UC Berkeley
UC Berkeley Electronic Theses and Dissertations

Title
Inorganic-Biological Hybrids for Solar-to-Chemical Production

Permalink
https://escholarship.org/uc/item/0jz8z74s

Author
Sakimoto, Kelsey Kenzo

Publication Date
2016

Peer reviewed|Thesis/dissertation

eScholarship.org Powered by the California Digital Library
University of California

Inorganic-Biological Hybrids for Solar-to-Chemical Production

by

Kelsey Kenzo Sakimoto

A dissertation submitted in partial satisfaction of the

requirements for the degree of

Doctor of Philosophy

in

Chemistry

in the

Graduate Division

of the

University of California, Berkeley

Committee in charge:

Professor Peidong Yang, Chair
Professor Michelle C.Y. Chang
Professor Ke Xu
Professor Luke P. Lee

Spring 2016

© Copyright by Kelsey Kenzo Sakimoto 2016
All Rights Reserved

Abstract

Inorganic-Biological Hybrids for Solar-to-Chemical Production

by

Kelsey Kenzo Sakimoto

Doctor of Philosophy in Chemistry

University of California, Berkeley

Professor Peidong Yang, Chair

The interplay of chemistry and biology holds many opportunities to address the woes of the modern world. As synthetic chemistry and cell biology have married together to make great strides in health and medicine, an amalgamation of inorganic materials chemistry and microbiology holds similar promise to revolutionize our approach to transducing solar energy into chemical bonds. By combining the superior light harvesting of inorganic semiconductors with enzymatic biocatalysts, high efficiency solar-to-chemical production of complex molecules and materials may outcompete natural photosynthesis. In this work, I describe a series of investigations into the physical and chemical interactions of inorganic-biological hybrid organisms. In the *Sporomusa ovata*-silicon nanowire system, changes in salt concentrations predictably controlled cell-nanowire alignment, producing a predictive model of inorganic-biological colloidal interaction. The hybrid organism *Moorella thermoacetica*-cadmium sulfide self-photosensitized the synthesis of acetic acid from CO_2 via bioprecipitated CdS nanoparticles. A titanium dioxide-manganese(II) phthalocyanine photocatalyst system extended oxygenic photosynthesis in *M. thermoacetica*-CdS through a photoregenerative cysteine-cystine redox couple. Finally, transient absorption spectroscopy, time-resolved infrared spectroscopy and biochemical assays suggested a two-pathway mechanism of charge and energy transport between *M. thermoacetica* and CdS. These initial works at the nexus of materials chemistry and biology lay the foundation for deeper understanding of this complex interface as well as for the development of advanced solar-to-chemical production systems.

Dedication

To Mom, Dad, Kayla, Kerry, Grandmas and Grandpas,
and Angela for their immoveable love and support.

Table of Contents

	Page
Acknowledgements	iii
Preface	v
List of Figures, Tables	viii
Chapter 1 - Salt-Induced Self-Assembly of Bacteria on Nanowire Arrays	
1.1 Introduction	1
1.2 Scanning Electron Microscopy Imaging of *S. ovata* on Nanowire Arrays	3
1.3 *S. ovata* Growth and Alignment Under High Salt and High Pressure Conditions	5
1.4 DLVO Theory of *S. ovata*-Nanowire Alignment	8
1.5 Conclusions	10
1.6 Materials and Methods	11
Chapter 2 - Self-Photosensitization of Non-Photosynthetic Bacteria for Solar-to-Chemical Production	
2.1 Introduction	13
2.2 Growth and Characterization of *M. thermoacetica*-CdS	15
2.3 Photosynthetic Performance of *M. thermoacetica*-CdS	19
2.4 Growth, Characterization and Photosynthetic Performance of *M. thermoacetica*-PbS	24
2.5 Conclusions	25
2.6 Materials and Methods	27
2.7 Supplementary Discussion	32
Chapter 3 - Cysteine-Cystine Photoregeneration for Oxygenic Photosynthesis of Acetic Acid from CO_2 by a Tandem Inorganic-Biological Hybrid System	
3.1 Introduction	34
3.2 Characterization of Phthalocyanine-based Cystine Reduction Photocatalysts	35
3.3 Photosynthetic Performance of *M. thermoacetica*-CdS+TiO_2-MnPc Tandem System	39
3.4 Conclusions	40
3.5 Materials and Methods	41
Chapter 4 - Spectroscopic Elucidation of Picosecond Energy Transfer Pathways in Hybrid Inorganic-Biological Organisms for Solar-to-Chemical Production	
4.1 Introduction	43
4.2 Photo-biochemical Characterization of *M. thermoacetica*-CdS	45
4.3 Transient Absorption Spectroscopy of *M. thermoacetica*-CdS	46
4.4 Time Resolved Infrared Spectroscopy of *M. thermoacetica*-CdS	48
4.5 Proposed Mechanism of *M. thermoacetica*-CdS Charge and Energy Transfer	50
4.6 Conclusions	52
4.7 Materials and Methods	53
References	54

Acknowledgements

As Max Bialystock and Leo Bloom parsed out 25,000% of the ownership of their show in *The Producers*, I must certainly attribute more than 100% of the credit for this dissertation to a number of people.

For the actual doing science and being a scientist bit, many thanks to Peidong as well as the entirety of the Yang lab throughout my 4 years here. The lessons are both in how to do good science, and how not to do good science, and for both sets experiences I'm extremely grateful. I think Peidong himself would admit he hasn't taught me a lot about science specifically, but more importantly, I've learned all the tangential business surrounding academia from one of the best. It's about more than just doing good work, and I'm proud to add another branch to the Yang academic family tree.

In particular, I must extend a special thank you to Andrew for many talks over the years about an innumerable number of things, and I will indeed miss being able to just turn my chair to the right to bother you late into the night.

Unexpectedly, I owe a great deal of thanks to Palmore, and all my various speech, debate and drama teachers throughout the years. Being able to speak and present my work with clarity and confidence has been a great boon to my career, I think, and so far has been able to convince most people I have a tiny inkling of what I'm talking about. At the very least, it's prevented me from doing weird things with my hands as I talk.

Oh, Angela, where would I be without you? Aside from being one of the few biologists to whom I can ask stupid basic questions, I think my perspective on life and of myself would be significantly different. You have been my singular and constant driving force throughout grad school, and I'm glad I can keep my promise of 4 years. While perhaps I spend too much time in lab (from lack of efficiency rather than diligence), I think it would be worse if you weren't there to look out for my mental welfare and social life (what little there is of it). I've thanked you many times in the past and will continue to do so as we move through life together, but give me a moment to reiterate. While the years at Yale and now at Berkeley would have changed me no matter what, I'm glad you've been there to help mold me along the way into someone I can look inwardly upon and say "eh, that'll do".

To my family, I am forever indebted not only for their help over the past 4 years, but the 22 before that as well. It is very fortunate that my parents placed such importance on education, and have given me the opportunities to explore and develop into the person that I am today. The weird oddities of my childhood, the hours I was given to tinker around and play by myself, and the indulgent way they would entertain my most eccentric hobbies directly reflects upon the way I do research. While this lab and graduate school have taught me the specifics of my field, how I do research and approach scientific inquiry was developed long before that. I'm unsure if they'll ever actually read the technical bits of this dissertation, but if they read nothing but this, I would like them to know how thankful I am for the time, money, and energy they've invested in me, and the things they've had to sacrifice to help me along the way. I hope they can look upon who I've become with pride. To think, I almost became a historian.

Now for the formal bits:

I acknowledge support from the NSF Graduate Research Fellowship Program under grant DGE-1106400. Solar-to-chemical production experiments were supported by the NSF under grant DMR-1507914. TEM was performed at the National Center for Electron Microscopy. TAS measurements were performed in the Molecular Foundry. Work at the Molecular Foundry was supported by the Office of Science, Office of Basic Energy Sciences, Materials Sciences and Engineering Division of the U.S. Department of Energy under Contract No. DE-AC02-05CH11231. I would also like to thank J.J. Gallagher and M.C.Y. Chang for the original inoculum of *M. thermoacetica* ATCC 39073 around which a great deal of this dissertation is based.

Preface

The availability of two fundamental building blocks, matter and energy, has governed the evolution of life on Earth. The natural abundance of particular chemical elements in Earth's chemosphere has, in part, dictated the evolution of biological life. While the smaller p-block elements (carbon, nitrogen, oxygen, phosphorus, sulfur) widely availed themselves throughout Earth's evolutionary history, we have only recently mined the heavier p-block elements and transition metals and mobilized them throughout the world. As such, it should come as no surprise that most of the biological world (of which we are a deeply rooted part) roots itself in covalent bonds of C, H, O, N, P, and S. Examination of most proteins, membranes, nucleic acids, etc. quickly reveals that biology has evolved to make use of only the most widely available chemical elements, achieving quite remarkable feats of catalysis, light harvesting, self-replication, self-repair, sensing, and mechanics, amongst others. Of these, none have been quite as revolutionary as the development of light harvesting, carried out predominantly today by chlorophyll found in plants and algae, which possess an innocuous porphyrin ring active center composed of C, N, H, and Mg. Yet, from these simple components, the advent of chlorophyll allowed the transduction of solar energy into chemical energy, driving thermodynamically uphill reactions such as the reduction of CO_2 into carbohydrates, and the oxidation of H_2O to O_2. Throughout this First Age of Photosynthesis, this thermodynamic energy input enabled the self-replication of enzymes and whole organisms over time, driving an evolutionary process that could slowly but surely sample a wide swath of parameter space in search of local optima.

As modern society traverses the 21st century, the availability of matter and energy has shifted, prompting new evolutionary forces governing the growth of life on Earth and beyond. For its energy needs, within the last 100 years humankind has largely relied upon the extraction of exhaustible reserves of carbonaceous petrochemicals. While this massive influx of thermodynamic energy has driven advances in industrialization and population expansion within our current Second Age of Petroleum, the limitations of this energy source has become painfully apparent, calling for an alternative source of energy to maintain our current standard of living.

However, simultaneously, this extensive mining and the abundance of energy it produced has unearthed a cornucopia of new materials, significantly expanding the toolbox of the modern chemist. Today, the modern scientist can access nearly every corner of the periodic table, from the transition metals to the lower p-block semi-metals and metalloids, all the way to the radioactive lanthanides and actinides. While their relative abundances still remain relatively low, this influx of new chemical building blocks has already forever changed the transduction of energy on Earth. Notably, the wide availability of Si(0) has driven the photovoltaic industry, facilitating the production of electrical energy directly from the sun. Additionally, many of these new light harvesting systems take advantage of the new optical and chemical properties available to materials on the nanoscale. With this basis, we have begun to enter a Third Age, what may be called the Third Age of Artificial Photosynthesis.

Of these three Ages of Energy, this Third Age remains in its infancy, unable to fully support the energetic and material needs of modern society. Though inorganic semiconductor based light harvesters certainly surpass the efficiency of natural photosynthesis, the formation of complex chemicals remains challenging. To accelerate the maturation of Artificial Photosynthesis, the approach described in this dissertation has taken a hybrid approach, combining semiconductor light capture with biological catalysis. Thus, while fully synthetic approaches to catalysis undergo development, we may take advantage of the evolutionary

process that has optimized enzymatic reaction as an initial entry point to complex chemical synthesis. This dissertation examines these hybrids of inorganic materials with biological organisms, exploring their properties and emergent features found at the newly formed interface of chemistry and biology, of the living with non-living. The following details the chemical and physical interactions of inorganic light harvesters, photocatalysts with biological enzymatic catalysts in these inorganic-biological hybrids.

Chapter 1 investigates the physical interaction of the hybrid inorganic-biological system *Sporomusa ovata* with Si nanowires. Favorable and controllable physical integration of the two disparate components must precede any chemical reactions and interactions. Through careful control of growth conditions, *Sporomusa ovata* cells can be tunably aligned parallel or perpendicular to the Si nanowires. This flexible interaction, modeled by Derjaguin-Landau-Verwey-Overbeek Theory of colloidal interactions, offers a rational entry point in describing and gaining control over the combination of biological- and nano-materials.

Chapter 2 demonstrates the chemical interaction of the hybrid inorganic-biological organism, *Moorella thermoacetica*-CdS, capable of self-replicating photosynthesis of acetic acid from CO_2. With the increased availability of heavy metals such as Cd and Pb mined for their electrochemical importance in batteries, this work hypothesizes an evolutionary step in which non-photosynthetic bacteria may now employ inorganic semiconductors rather than molecular light absorbers to self-photosensitize. The growth/synthesis and performance of this newly photosynthetic organism represents a first step in this Third Age of Artificial Photosynthesis and a paradigm shift in how solar-energy is converted to chemical energy.

Chapter 3 integrates a purely chemical photocatalyst, TiO_2-Manganese(II) Phthalocyanine with *M. thermoacetica*-CdS to enable oxygenic photosynthesis, relying upon a photoregenerated redox cycle. The integration of both chemical and biological catalysis demonstrates the flexibility of such hybrid systems.

Chapter 4 employs spectroscopic and biochemical characterization to uncover and postulate the mechanism of charge and energy transfer within *M. thermoacetica*-CdS. Data from enzyme activity assays, transient absorption spectroscopy, and time-resolved infrared spectroscopy suggest two energy transfer pathways may link inorganic and biological components to drive solar-to-chemical production.

The work in Chapter 1 was based on:
Sakimoto, K. K., Liu, C., Lim, J. & Yang, P. Salt-Induced Self-Assembly of Bacteria on Nanowire Arrays. *Nano Lett*. **14,** 5471–5476 (2014)

The work in Chapter 2 was based on:
Sakimoto, K. K., Wong, A. B. & Yang, P. Self-photosensitization of nonphotosynthetic bacteria for solar-to-chemical production. *Science*. **351,** 74–77 (2016)

The work in Chapter 3 was based on:
Sakimoto, K. K., Zhang, S. J. & Yang, P. Cysteine-Cystine Photoregeneration for Oxygenic Photosynthesis of Acetic Acid from CO_2 by a Tandem Inorganic-Biological Hybrid System. *Submitted* (2016)

The work in Chapter 4 was based on:
Kornienko, N.*, Sakimoto, K. K.*, Herlihy, D. M., Nguyen, S. C., Alivisatos, A. P., Harris, C. B., Schwartzberg, A. M., & Yang, P. Spectroscopic elucidation of picosecond energy transfer pathways in hybrid inorganic-biological organisms for solar-to-chemical production. *Submitted* (2016)

*denotes equal contribution

List of Figures, Tables

Figure 1-1. Scanning Electron Microscopy (SEM) and Fluorescence Micrographs of *S. ovata* on Nanowire Arrays 3
Figure 1-2. Scanning Electron Micrograph of Aligned Filamentous *S. ovata* on Silicon Nanowire Arrays 4
Figure 1-3. Filamentous Growth of *S. ovata* 6
Figure 1-4. Radar Plots of Bacteria-Nanowire Angle Distribution 7
Figure 1-5. Cumulative Distribution Functions of Bacteria-Nanowire Angle 8
Figure 1-6. Model and Mechanism of Bacteria-Nanowire Interaction 9

Figure 2-1. *M. thermoacetica*-CdS Reaction Schematics 14
Figure 2-2. Hypothesized Electron Transfer Pathways for *M. thermoacetica*-CdS 15
Figure 2-3. Culture Tubes of *M.thermoacetica*-CdS and Growth Kinetics 16
Figure 2-4. Electron Microscopy of *M. thermoacetica*-CdS Hybrids 17
Figure 2-5. Additional Electron Microscopy of *M. thermoacetica*-CdS Hybrids 18
Figure 2-6. Characterization of CdS Nanoparticles 19
Figure 2-7. *M. thermoacetica*-CdS Photosynthesis 20
Figure 2-8. ^{1}H-NMR Spectrum of Photosynthetic Products 21
Figure 2-9. CFU and Cell Counts for *M. thermoacetica*-CdS During Photosynthesis 22
Figure 2-10. SEM of Photooxidative Damage to *M. thermoacetica*-CdS 23
Figure 2-11. Optical Characterization of *M. thermoacetica*-PbS 25
Figure 2-12. Acetic Acid Production of *M. thermoacetica*-PbS 25
Figure 2-13. Spectrum of Blue Light Illumination Source 30

Figure 3-1. Schematic of the *M. thermoacetica*-CdS + TiO_2-MnPc Tandem System 35
Figure 3-2. Reflectance Spectra of TiO_2-MnPc 36
Table 3-1. CySS Reduction Rate of Phthalocyanine Loaded TiO_2 Photocatalysts 36
Figure 3-3. CySS Photoreduction Kinetics of TiO_2-MnPc 37
Figure 3-4. Reflectance Spectra of TMPc and TiO_2-TMPc 38
Figure 3-5. Direct Comparison of TMPc and H_2Pc Reflectance Spectra 38
Figure 3-6. Photosynthetic Performance of *M.thermoacetica*-CdS and TiO_2-MnPc Tandem System 39

Figure 4-1. Schematic of *M. thermoacetica*-CdS Photosynthetic Charge Transfer 44
Figure 4-2. Biochemical Assays of *M. thermoacetica*-CdS 45
Figure 4-3. H_2ase Activity of *M. thermoacetica*-CdS with Varying H_2 Concentration 45
Figure 4-4. TAS of *M. thermoacetica*-CdS 47
Figure 4-5. Supplementary TAS Spectra of *M. thermoacetica*-CdS 47
Figure 4-6. TRIR Spectra of *M. thermoacetica*-CdS 49
Figure 4-7. Standard Error of TRIR Spectra 50
Figure 4-8. Proposed Dual Pathway of Charge and Energy Transfer in *M. thermoacetica*-CdS 51

Chapter 1

Salt-Induced Self-Assembly of Bacteria on Nanowire Arrays

Abstract:

Studying bacteria-nanostructure interactions is crucial to gaining controllable interfacing of biotic and abiotic components in advanced biotechnologies. For bioelectrochemical systems, tunable cell-electrode architectures offer a path towards improving performance and discovering emergent properties. As such, *Sporomusa ovata* cells cultured on vertical silicon nanowire arrays formed filamentous cells and aligned parallel to the nanowires when grown in increasing ionic concentrations. Here, we propose a model describing the kinetic and the thermodynamic driving forces of bacteria-nanowire interactions.

1.1 Introduction:

A deeper understanding of the interactions of biological systems with nanostructures has gained pertinence with the development of 1) investigative tools designed to match the micro- to nanometer length scale of single cells,[1,2] as well as 2) hybrid systems which combine the catalytic and synthetic power of microorganisms, such as bacteria, with the optoelectronic capabilities of abiotic materials, such as inorganic nanowires.[3] The majority of the work has been biomedical in nature, devoted to understanding the interface between nanoparticles and mammalian cells as probes of neuronal and eukaryotic cell activity,[4] or to developing nanostructured surfaces designed to prevent the growth of pathogenic bacteria.[5]

In contrast to the chemical and geometric anti-microbial properties desired for applications such as biomedical devices, the growing field of bioelectrochemistry calls for the development of pro-microbial materials to create a controllable and favorable interaction between microorganisms and the surfaces of electrodes.[6,7] The field of bioelectrochemistry has stemmed from the realization that traditional oxidation-reduction reactions, catalysts, and electrodes, can be interchanged with the biochemical reactions and enzymes that drive cellular metabolism. This approach offers the ability to use electrochemistry to both intercept and study the complex chains of biological redox reactions, as well as augment electrochemical systems with the vast synthetic diversity and specificity of enzyme and whole-cell catalysis.[8] In microbial fuel cells (MFCs), bacteria attach to conductive electrodes to catalyze the oxidation of organic matter to generate electricity.[9] In microbial electrosynthesis cells (MECs), external voltage biases are applied to drive the biological reduction of small molecules to synthesize commodity chemicals and fuels.[10] As a first demonstration of a new type of hybrid artificial photosynthesis, we have recently shown that the direct integration of the acetogen *Sporomusa ovata* with high surface area, photoactive silicon (Si) semiconductor nanowires is able to photoelectrochemically drive the biological reduction of CO_2 to acetate.[3] For such applications, high surface area electrodes, such as carbon cloth or nanostructured electrodes, are desired to increase the performance of typically low density microbial catalysts. Nanowire array photoelectrodes are well suited to such a purpose, providing high photoelectrochemical performance in addition to increased surface area. Advances in these bioelectrochemical systems will be aided first by understanding and controlling the interfacing of bacterium and nanowire.

As an analytical tool, the nanowire array platform offers several distinct advantages to the study of bacteria-surface interactions. With a well-defined geometry, the physical relation between bacteria and nanowire can be precisely measured and analyzed to probe the underlying interaction. By providing a surface perpendicular to the imaging plane, vertically oriented nanowires allow for *in situ* optical monitoring of cell-surface interactions without the need for complex confocal microscopy techniques or other forms of 3D microscopy.[11] For *ex situ* techniques, such as scanning electron microscopy (SEM), the low convective flux through the nanowire array reduces the disruption of cell attachment, guarding against the formation of structural artifacts due to the serial washing and drying steps required for *ex situ* high vacuum techniques. The high surface area allows for quick measurement of many cells at once, enabling quick statistical averaging in order to obtain significant results. These advantages poise nanowire arrays as a potent tool to investigate cell-surface interactions.

Studies of the interactions between cells and nanowires have largely focused on the influence of geometric and steric features of nanowire arrays in cell growth, patterning, and motility.[11–15] By decreasing the spacing between vertical nanowires, bacteria cells can become squeezed and confined into a vertical attachment, parallel to the nanowires.[16] However, cell-nanowire interactions are also greatly influenced by the myriad of environments in which cells are naturally found. The wide range of temperatures, pH, pressure, and salinity in which microorganisms thrive[17] are liable to alter the surface and colloidal interactions of bacteria and nanostructures,[18] and bears further scrutiny into the role of growth conditions in cell-nanowire interactions.

The approach we have adopted to understand the effect of different growth conditions is to model the interaction between colloids such as bacteria and nanowires by the widely used Derjaguin-Landau-Verwey-Overbeek (DLVO) theory, which describes the pairwise interaction as the sum of a van der Waals attractive force, and an electrostatic repulsive force originating from the pH sensitive, typically negatively charged bacteria membrane and inorganic oxide surface.[19–21] While the attractive force is fairly unalterable, the repulsive force can be readily decreased with increased ionic strength (through increased concentrations of dissolved salts, such as NaCl).[22] While this approach explicitly describes the potential energy landscape of this bacteria-nanowire interaction, dynamic information can be similarly derived,[23] yielding predictive power over the subtle interplay of thermodynamic and kinetic driving forces to attachment. The reduced dimensionality of nanowires and similar length scales to single bacteria cells allow for facile application of one dimensional solutions to DLVO theory, offering a quick and intuitive understanding of this interaction. Such models have been widely used to explain nanoparticle-nanoparticle, protein-protein, and cell-bulk surface interactions,[18,22] and offers a potential route to understanding and tuning bacteria-nanowire interactions.

In this work, we offer the first investigation into the application of nanowire arrays to study the physical interaction between bacteria and nanostructures at varying ionic concentration and pressure. We demonstrate the ability to tune the orientation of attached *S. ovata* cells cultured on Si nanowire arrays of various geometries, employing facile changes in growth conditions. This offers a generalized approach to study bacteria-nanowire, or more broadly, cell-nanostructure interaction and self-assembly, with applications ranging from bioelectrochemical systems to biomedical control of cell-surface interaction.

1.2 Scanning Electron Microscopy Imaging of *S. ovata* on Nanowire Arrays:

To test the validity of our DLVO-based model, Si nanowire arrays were submerged in growth media of varying compositions, inoculated with *S. ovata* cells, and then incubated to simulate the initial electrode colonization by bacteria typical of many bioelectrochemical systems.[3,24] The Si nanowire dimensions (approximately 800 nm in diameter and 25-30 μm in length) were selected in accordance with the optimized geometry for Si photocathode performance, with the periodicity of the array varied to study the effect of steric confinement. After 6 days of growth, nanowire arrays were removed from the growth media. The resulting bacteria-nanowire structure was analyzed by fluorescence microscopy and scanning electron microscopy (SEM) to quantify the rod-shaped cells' attachment orientations within the array.

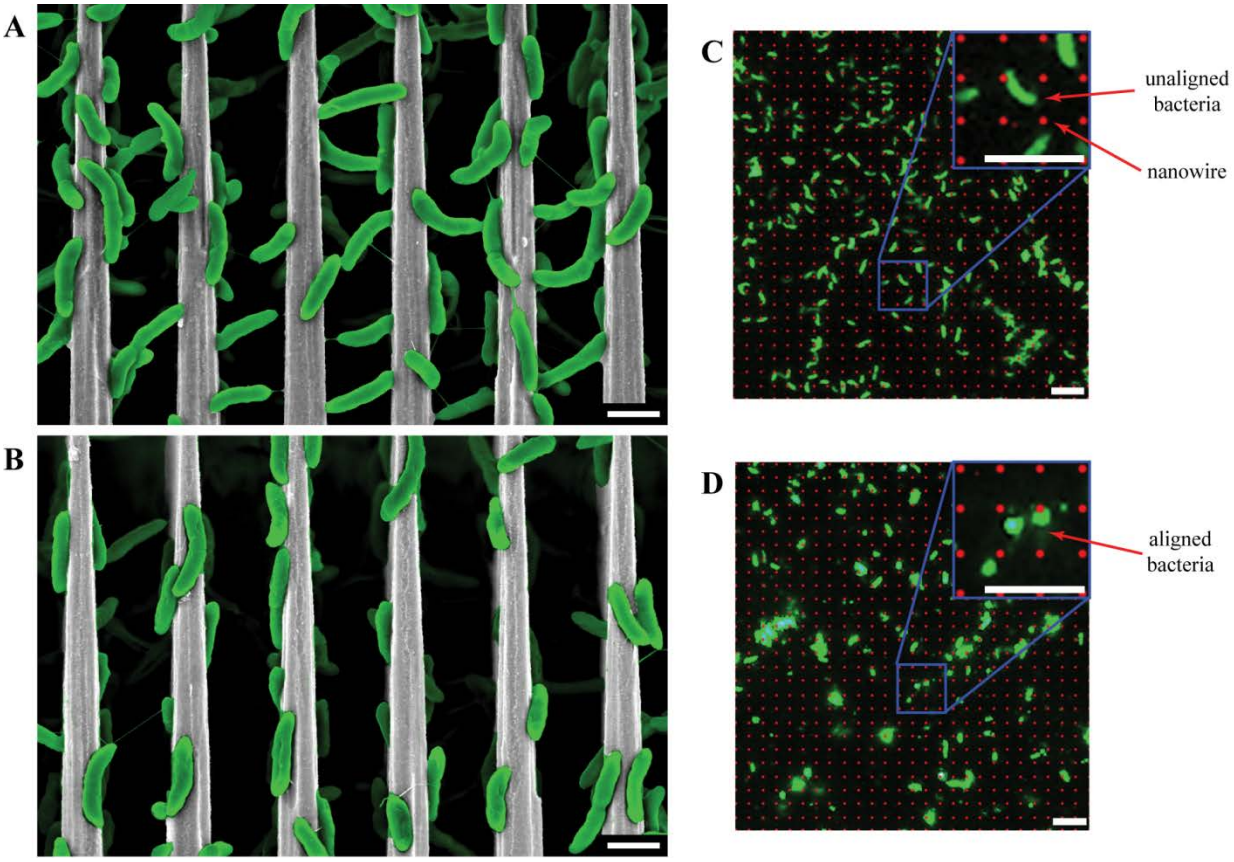


Figure 1-1. Scanning Electron Microscopy (SEM) and Fluorescence Micrographs of *S. ovata* on Nanowire Arrays. (A, B) SEM and (C, D) fluorescence images were taken of *S. ovata* cells grown on Si nanowire arrays of 4 μm periodicity under (A, C) normal ionic concentrations (~100 mM) and 100 kPa H_2:CO_2, showing random orientations with respect the nanowire axis, and (B, D) with +200 mM NaCl and 500 kPa H_2:CO_2, showing alignment with the nanowire. Both (A, B) side view SEM and (D, E) top down *in situ* fluorescence microscopy show alignment, with (C) unaligned bacteria appearing as rods in fluorescence micrographs, and (D) aligned bacteria appearing as circles. Scale bars (A, B) 2 μm (C, D) 5 μm.

When cultured in normal, literature recommended growth media and conditions (~100 mM ionic strength, 100 kPa H_2:CO_2 as growth substrate),[3,10] cross sectional SEM (Fig. 1-1A)

reveals that bacteria populate the array with random orientations with respect to the vertical nanowires. However, when the bacteria are grown on the array in media of increased ionic strength (the normal growth media supplemented with an additional 200 mM NaCl), the cells self-assemble onto the array in a vertically aligned orientation, mostly parallel to the nanowires (Fig. 1-1B, 1-2). These results are corroborated by *in situ* fluorescence microscopy, in which (Fig. 1-1C) unaligned bacteria appear as rods (cells lying flat with respect to the imaging plane, perpendicular to the nanowires), and (Fig. 1-1D) parallel aligned bacteria appear as circles (a 2 dimensional projection down the length of the bacteria cell). The agreement between *in situ* fluorescence microscope images and *ex situ* SEM images demonstrates the ability of nanowire arrays to reduce disruptions in cell attachment during preparation for high vacuum techniques. Qualitatively, these results show that increasing the ionic strength by simple addition of NaCl shifts the bacteria-nanowire orientation from a random state (low salt) to a parallel aligned state (high salt).

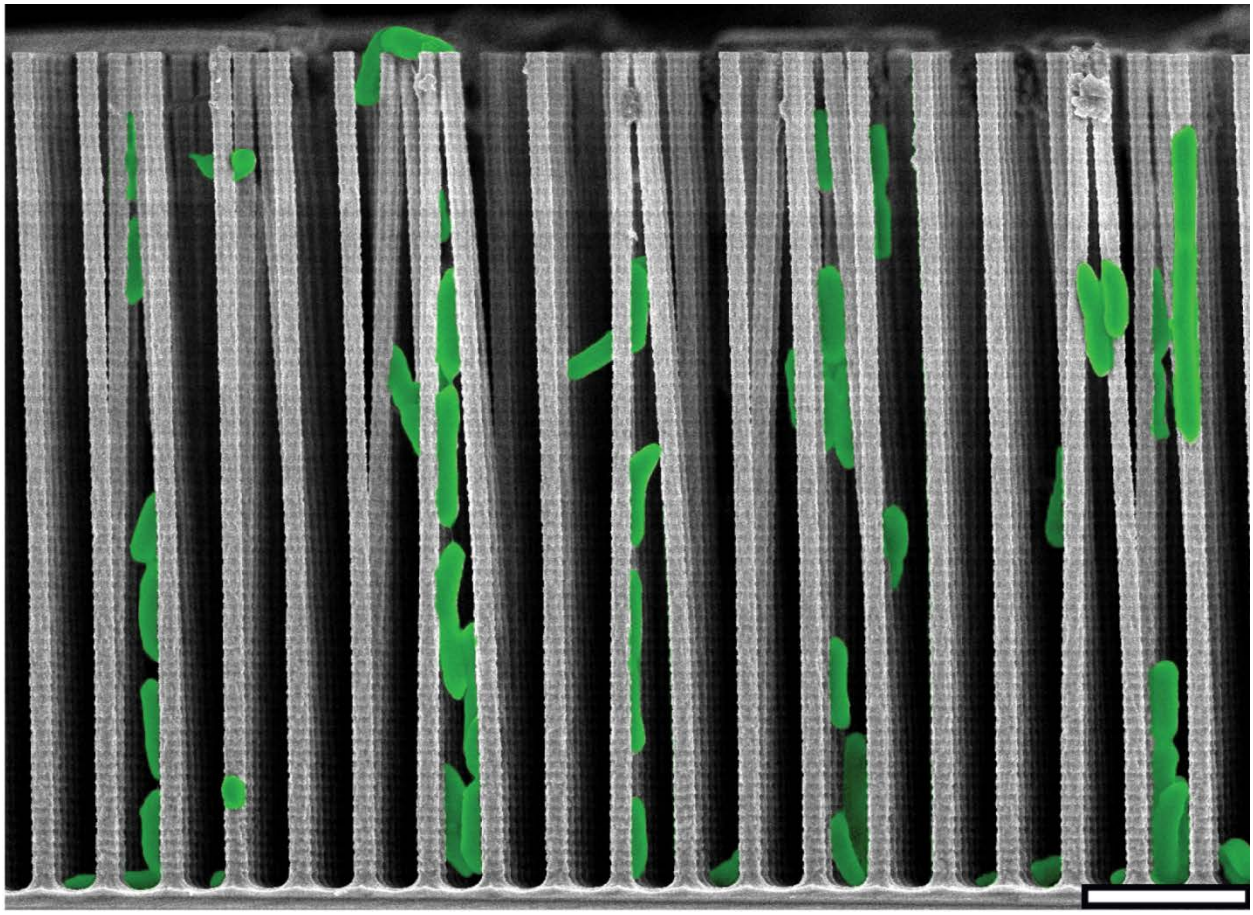


Figure 1-2. Scanning Electron Micrograph of Aligned Filamentous *S. ovata* on Silicon Nanowire Arrays. When grown under conditions of increased NaCl concentration and H_2:CO_2 pressure, *S. ovata* cells form multicellular filamentous cells. Such cells preferentially attach parallel to the nanowire in their filamentous form, followed by eventual division into single cells. Scale bar 5 μm.

1.3 *S. ovata* Growth and Alignment Under High Salt and High Pressure Conditions:

To further investigate the mechanism of this self-assembled alignment, cell morphology and growth kinetics were measured for planktonic cells under increasing NaCl concentrations to determine whether salt-induced alignment was attributable to physiological changes in the bacteria themselves. Conditions of higher salinity were found to promote cell filamentation, as evidenced by SEM images and broadening of cell length histograms (Fig. 1-3B, D), regularly producing cells upwards of 2~5 times their normal length. We hypothesized that the observed cell filamentation was attributable to the concomitant increased osmotic pressure produced by addition of NaCl, as has been observed for other bacteria species.[25] Cell filamentation has been shown to be related to pressure induced inhibition of cell division proteins from either osmotic or hydrostatic pressure changes during growth.[26,27] To test this possibility, *S. ovata* cells were also cultured under conditions of increased hydrostatic pressure up to 500 kPa H_2:CO_2, achieved by pressurizing the headspace above the culture medium. Increased hydrostatic pressure produced similar cell filamentation (Fig. 1-3C, D). Growth under increased osmotic and hydrostatic pressures were characterized by increased cell doubling times (decreased growth rate) as monitored by cell suspension optical density (Fig. 1-3E). Filamentous cells were also found to eventually divide into single cells after extended culturing time (>6 days), as well as resist filamentation with the addition of osmolytes such as betaine, which is consistent with previous observations of osmotic and hydrostatic pressure induced arrested cell division and filamentation.[28] Such changes in cell morphology and growth kinetics have the potential to influence cell-nanowire interactions and must be accounted for in subsequent analyses.

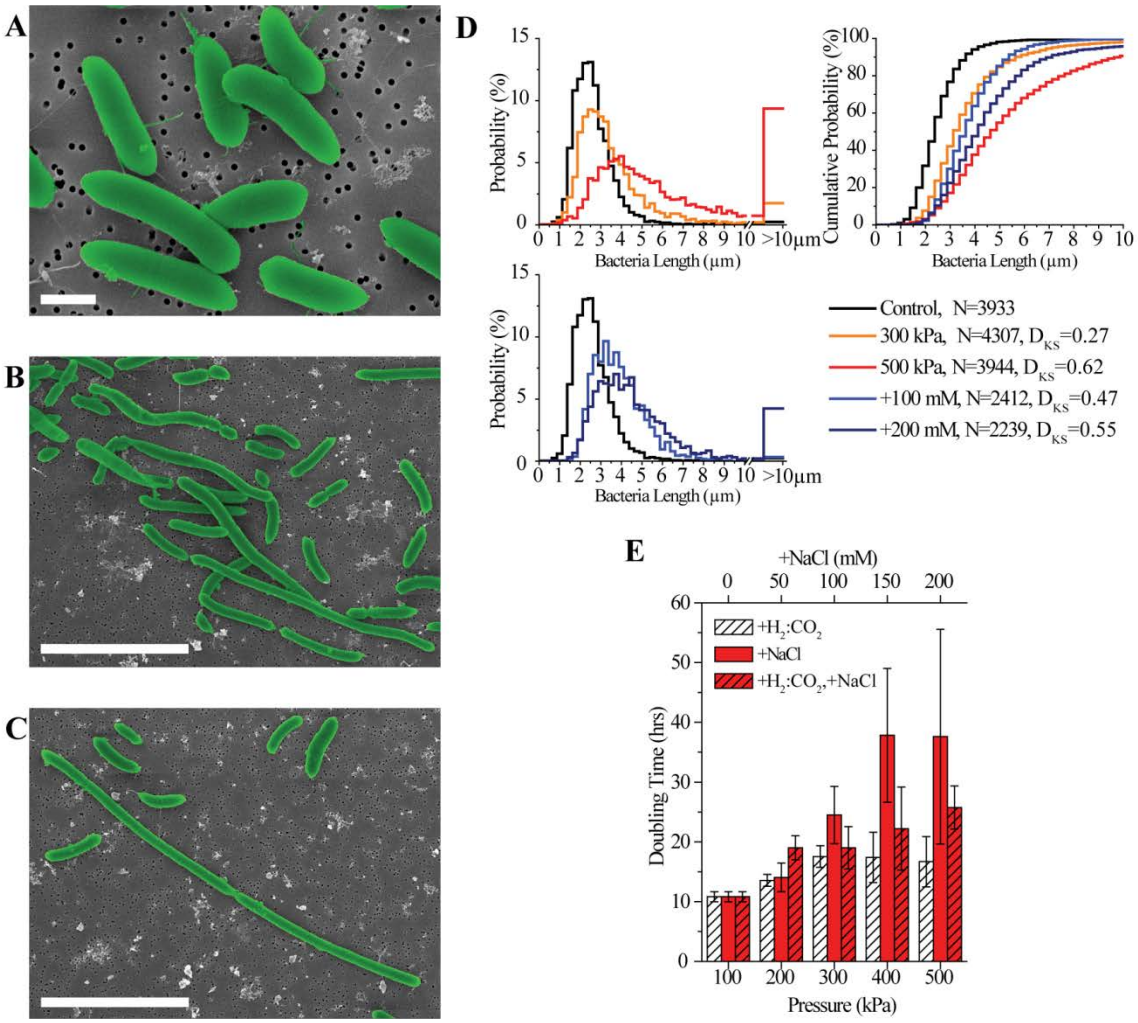


Figure 1-3. Filamentous Growth of *S. ovata*. (A, D) Under normal growth conditions, *S. ovata* form single cells approximately 2~3 μm x 0.5 μm. With (B, D) increasing NaCl concentrations or (C, D) H_2:CO_2 pressure, *S. ovata* forms long filamentous cells. (D) Cell length histograms and two-sample modified Kolmogorov-Smirnov test statistics were calculated, rejecting the null hypothesis at significance $\alpha < 0.001$.[29] (E) The formation of these filamentous cells is accompanied by increases in the cell doubling time. Scale bars (A) 1 μm, (B, C) 5 μm.

In order to deconvolute the effects of reduced electrostatic repulsion from the effects of cell filamentation brought on by increased ionic strength, cells were cultured on nanowire arrays under conditions of increasing NaCl concentrations, increasing H_2:CO_2 pressure, or both. As shown by the radar plots of bacteria-nanowire angles measured from SEM images (Fig. 1-4), as the ionic strength is incrementally increased, the distribution of bacteria-nanowire angles gradually shifts from a random (even distribution from 0° to 90°) to a preferentially aligned distribution (large peak centered at 0°). This effect appears to be independent of the previously observed steric control, as square periodic nanowire arrays of both 2 μm and 4 μm periodicity (*S. ovata* diameter ~0.5 μm) display similar trends (Fig. 1-4, 1-5). The effect of increasing hydrostatic pressure on bacteria-nanowire orientation was also investigated, and showed minimal variation at the same ionic strength with pressures up to 500 kPa H_2:CO_2. The angle distributions were statistically analyzed by means of a two-sample modified Kolmogorov-Smirnov (KS)

test.[29] For increasing NaCl concentrations, +100 mM NaCl and +200 mM NaCl, the calculated KS statistic with respect to normal growth conditions similarly increased, rejecting the null hypothesis at a significance of $\alpha < 0.1$ and $\alpha < 0.05$, respectively. Distributions between different nanowire array periodicities and between different pressures showed no statistically significant difference ($\alpha > 0.2$) (Fig. 1-5). While the effect of cell elongation and retarded growth rate brought on by increased osmotic or hydrostatic pressure cannot be fully discounted, these results suggest that high ionic concentrations alone are required to produce cell alignment.

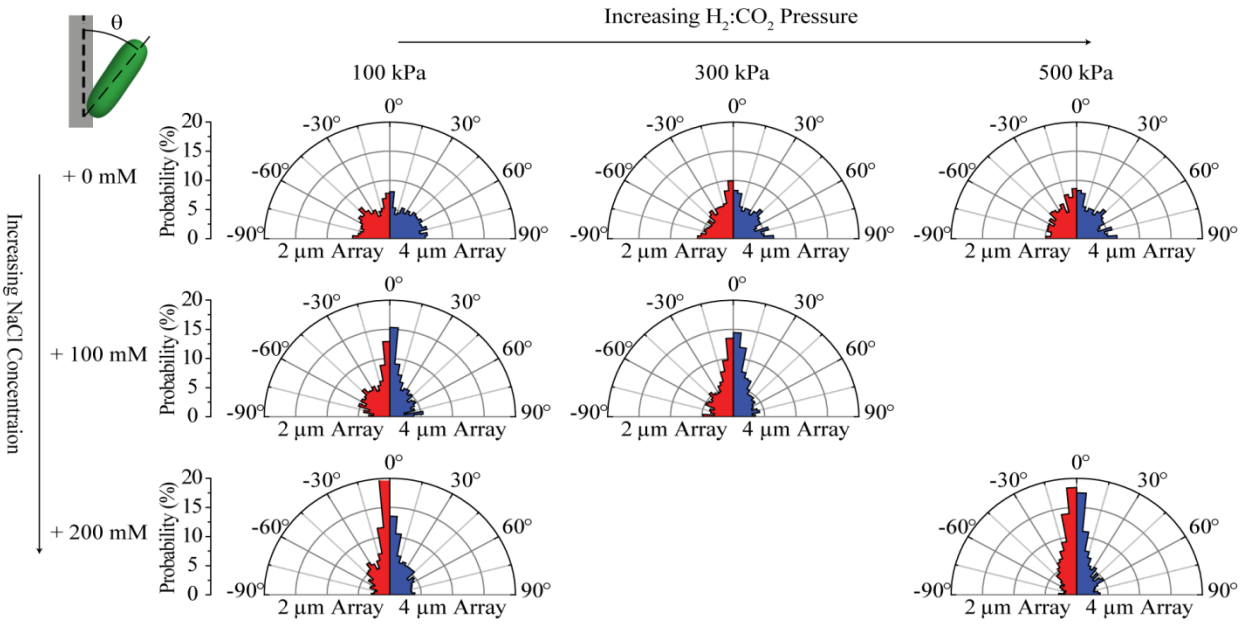


Figure 1-4. Radar Plots of Bacteria-Nanowire Angle Distribution. Measured angles between bacteria and nanowire axes were measured via SEM for growth conditions of increasing NaCl concentrations, H_2:CO_2 pressure, or both. While increasing pressure shows little variation in the angular distribution, increasing NaCl concentrations shows a distinct shift towards the aligned (0°) state.

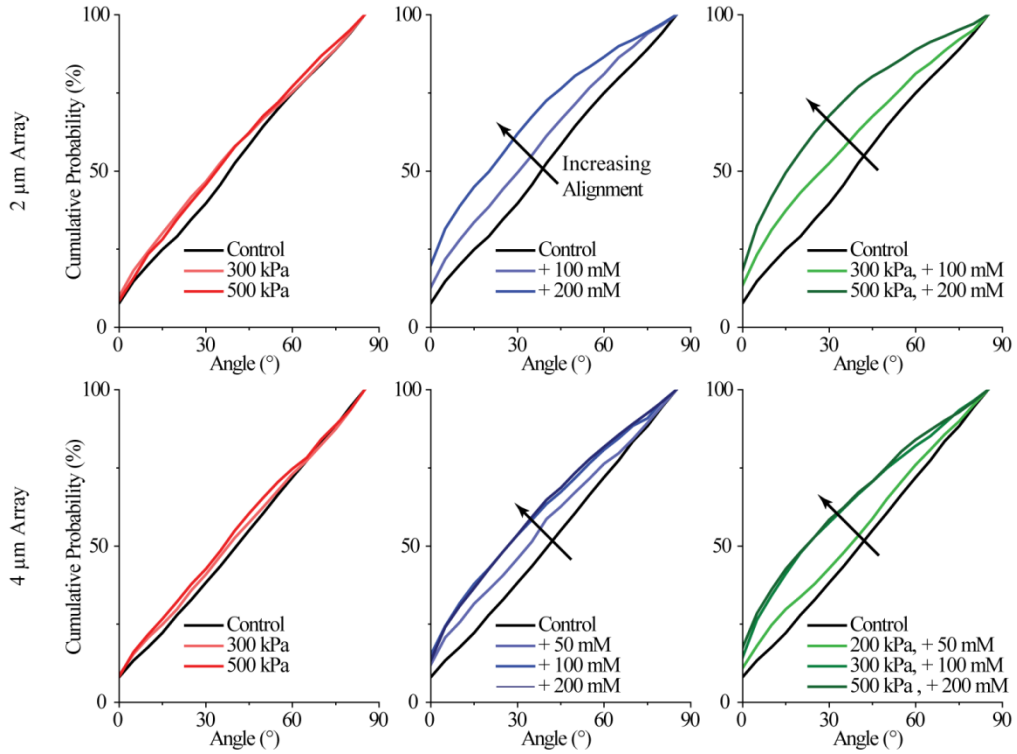


Figure 1-5. Cumulative Distribution Functions of Bacteria-Nanowire Angle. Bacteria-nanowire angles for various growth conditions (increasing NaCl concentration or H_2:CO_2 pressure) were measured by SEM for 2 µm and 4 µm periodicity arrays. For both periodicities, little change is observed for increasing pressure, while conditions of increasing NaCl concentration show gradually greater alignment.

1.4 DLVO Theory of *S. ovata*-Nanowire Alignment:

To provide a mechanistic insight into bacteria-nanowire interactions, DLVO theory interaction energy curves were generated to describe the thermodynamic energy landscape of attachment (Materials and Methods). Curves were generated for normal ionic concentrations (100 mM total ionic concentration) (Fig. 1-6A) and +200 mM NaCl conditions (300 mM total ionic concentration) (Fig. 1-6B), for an unaligned configuration (the bacterium perpendicular to the nanowire, $\perp$) and an aligned configuration (the bacterium parallel to the nanowire, $\parallel$). While the energies of the primary minima offer insight into the thermodynamic stability of various configurations, these interactions are influenced not only by thermodynamic factors, but kinetic factors as well.

The bacteria-nanowire angle distribution was rationalized in terms of the kinetic rates of attachment and detachment for each configuration. From this, the angle distribution will shift towards the configuration pathway with a faster effective rate (i.e. the sum of attachment and detachment rates). Analogous to transition state theory for chemical reactions, the rate of attachment/detachment is exponentially proportional to the height of the activation energy barrier, $\Delta G_{attach/detach}$ (Fig. 1-6A).[23] At normal ionic concentrations, the aligned configuration pathway is relatively slow due to the large energy barrier ($\Delta G_{attach,\parallel} >> \Delta G_{attach,\perp}$). As such, the kinetically favored pathway with the smaller energy barrier is achieved, disfavoring bacteria-nanowire alignment.

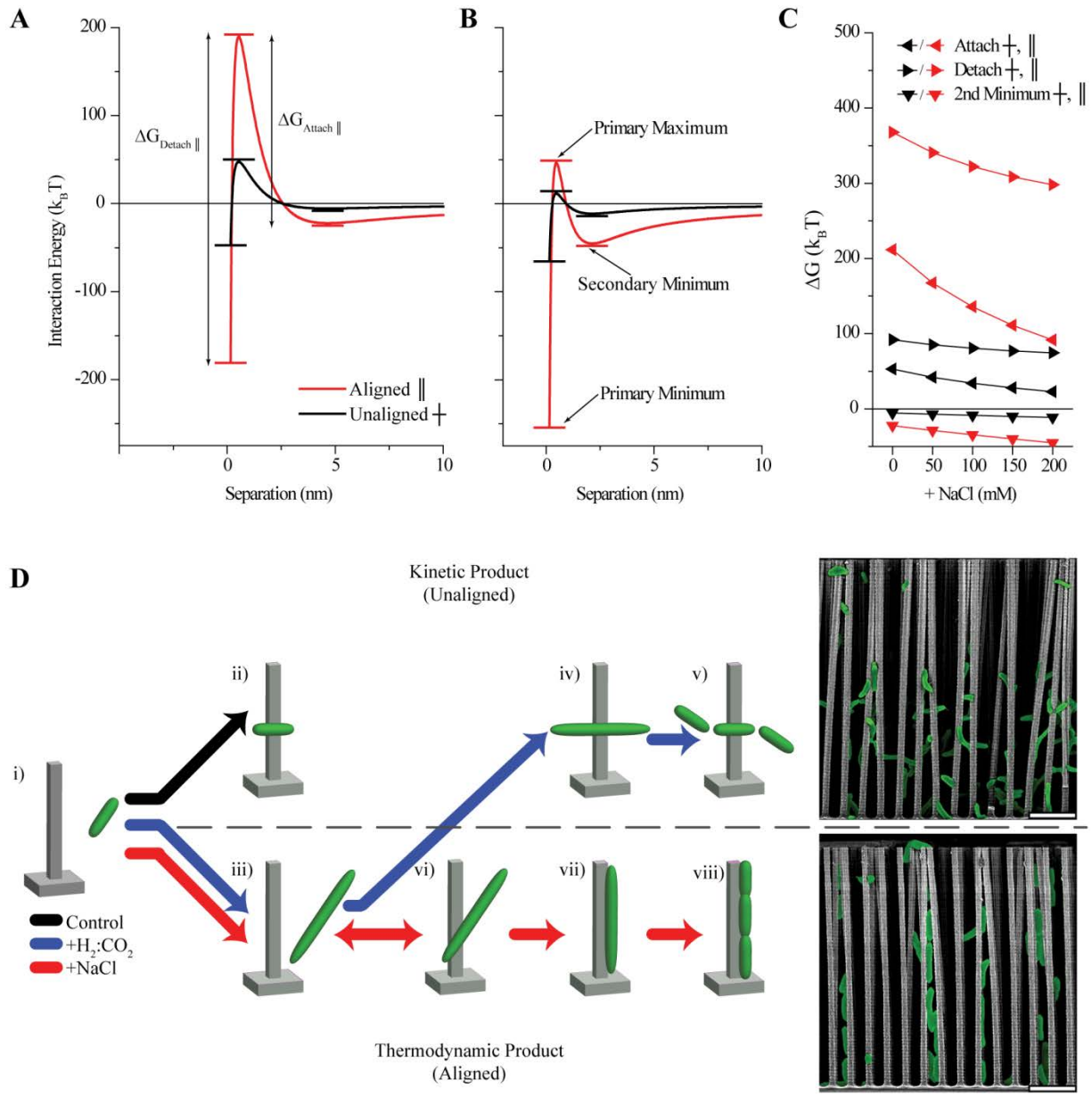


Figure 1-6. Model and Mechanism of Bacteria-Nanowire Interaction. Derjaguin-Landau-Verwey-Overbeek (DLVO) model curves were generated for bacteria attachment in a perpendicular (unaligned, ┼) and parallel (aligned, ‖) orientation for (A) normal growth conditions and (B) +200 mM NaCl growth media. (C) The activation energy barriers for attachment, detachment, and the secondary minima were calculated for +0 mM to +200 mM NaCl, showing decreasing values at higher ionic concentrations. (D) In the proposed mechanism, i) planktonic cells ii) attach in the unaligned state (kinetic product) under normal conditions. Under increased hydrostatic or osmotic pressure iii) filamentous cells form. At normal ionic strengths, iv-v) the kinetically favored unaligned state is achieved. However, at increasing NaCl concentrations, vi) the bacteria cell enters a reversible adhesion state, from which vii-viii) the thermodynamically favored product is achieved. Representative SEM images for *S. ovata* grown at (top) control conditions and +200 mM NaCl (bottom) on 2 μm periodicity arrays are included. Scale bars 5 μm.

Due to the decreasing electrostatic repulsion with increasing ionic strength, all free energies decrease under high salt conditions (Fig. 1-6C).[18,22] As the ionic strength increases from 100 mM to 300 mM (+0 mM to +200 mM NaCl), the heights of both the aligned and unaligned pathway energy barriers decrease. In the unaligned pathway, $\Delta G_{attach,\perp}$ is comparable in magnitude to $\Delta G_{detach,\perp}$, meaning this pathway is fairly reversible. In contrast, $\Delta G_{attach,\parallel} << \Delta G_{detach,\parallel}$, indicating parallel attachment is still fairly irreversible. Thus, at this high ionic strength, the bacteria become trapped in the orientation with the lowest primary minimum, selecting the thermodynamically favored attachment scheme (alignment). Also notable is the formation of a pronounced secondary minimum, allowing the cell to loosely associate with the nanowire in a reversible attached state, from which the bacteria can sample several possible attachment configurations, and come to rest in the most energetically favorable one.[30] Though elongation produced by increases in hydrostatic pressure alone is unable to effect bacteria-nanowire alignment, the effect of cell elongation under increased ionic strength (increased osmotic pressure) cannot be wholly discounted. As cells elongate under increased osmotic pressure, the thermodynamic driving force and concomitant torque force towards alignment become magnified, scaling with cell surface area. Additionally, previous work has suggested attachment efficiency is also mediated by cell growth phase.[31] Due to cell membrane surface charge heterogeneities during the early stages of growth, electrostatic repulsion is reduced, allowing faster adhesion rates. The observed preferential alignment perhaps stems in part from the longer growth time scale under increased osmotic pressures (Fig. 1-3E). From these observations, a mechanism for bacteria-nanowire interactions is proposed (Fig. 1-6D).

1.5 Conclusions:

Our results have demonstrated the ability to control the orientation of bacteria attachment to nanowires by simple changes in ionic strength, utilizing nanowire arrays as a platform for precise measurement of cell-surface attachment. More generally, the applicability of DLVO theory towards cell-nanostructure interactions demonstrated by this work provides a well-studied predictive framework for not only investigations of bioelectrochemical systems, but for the further development of nanomaterials for the biomedical and biotechnological fields, where widely varying temperatures, pressures, pH, salinities and surface properties are regularly encountered. As we have shown, this predictive power enables both the analysis of and the ability to modulate the subtle interplay of thermodynamic and kinetic driving forces to control this colloidal interaction. These insights into the fundamental nature of bacteria-nanowire interactions offer a path towards designing the next generation of nano-bio hybrid systems.

1.6 Materials and Methods:

Si Nanowire Array Fabrication[3]

Si p-type <100> oriented 4-6" wafers were patterned with a photoresist square dot array with a periodicity of 2 or 4 μm using a standard photolithography stepper. Nanowires were formed by inductive-coupled plasma deep reactive-ion etching (Surface Technology Systems, Inc.), followed by O_2 plasma to remove residual photoresist. Nanowire diameters were controlled by iterative cycles of dry thermal oxide growth (1050 °C, 40 min) and 10:1 buffered HF. Periodicity 2 μm arrays required critical point drying (Tousimis, Inc.) to prevent nanowire bundling. A final oxide outer coating was formed by atomic layer deposition of 30 nm conformal TiO_2 (300 °C, $TiCl_4/H_2O$ precursors), or dry thermal oxidation (850 °C, 12 hours, ~50 nm SiO_2). Final dimensions of Si nanowire arrays were approximately 800 nm in diameter and 25-30 μm in length.

Bacterial Growth on Nanowire Arrays

Cryopreserved (10% DMSO) *Sporomusa ovata* (ATCC 35899) was inoculated 0.4% into aluminum crimped Balch tubes containing pre-reduced media (DSMZ 311) omitting betaine, casitone, and resazurin prepared under standard anaerobic technique (defined as the normal, control growth conditions). Up to 200 mM additional NaCl was added prior to autoclaving.

Nanowire arrays were cut into 0.5 cm x 0.5 cm chips and cleaned with O_2 plasma prior to sealing within sterile Balch tubes flushed with anoxic H_2:CO_2 (80:20). To each 20 mL Balch tube (23 mm × 75 mm, Chemglass Life Sciences) was added 2.5 mL of inoculated media, giving approximately 1mm of media above the surface of the nanowire array. The headspace of each tube was pressurized with anoxic H_2:CO_2 (80:20) up to 500 kPa (100 kPa defined as the normal growth conditions). As H_2:CO_2 was consumed, the culture tubes were repressurized every 24 hours, or connected via gas pressure regulator to a gas cylinder to maintain constant pressure. Inoculated tubes were incubated at 30 °C for 6 days with minimal agitation.

Bacteria Growth Kinetics and Cell Length

Planktonic bacteria were grown in suspension as per the protocol above. To test for substrate dependence, culture tubes were optionally supplemented with 50 mM betaine or sodium lactate, flushed with anoxic N_2 and pressurized up to 400 kPa. For the first 3 days of growth, cultures were sampled every 6 hours. OD_{600} measurements (SpectroVis, Vernier) were used to determine growth rate under varying concentrations of NaCl and H_2:CO_2 pressures based on standard Monod kinetics. Optical measurements were confirmed with cell counting in a Petroff-Hausser counting chamber. Cultures were then processed for scanning electron microscopy (SEM) as detailed below.

Fluorescence Microscopy

After bacterial growth on nanowire arrays, the chips were removed from media and gently washed with isotonic phosphate buffered saline (PBS) to remove planktonic cells. Bacteria were stained with a fluorescent dye (BacLight Green, Invitrogen) in PBS as per the manufacturer suggested protocol. Stained bacteria-nanowire chips were imaged with an upright microscope (Eclipse LV100D-U, Nikon) outfitted with filter sets appropriate for FITC imaging (B-2E/C FITC, Nikon). Images were captured by a microscope mounted camera (Moticam Pro, Motic) at 20×, 50× magnification. All steps were conducted in an anaerobic chamber (Coy Labs).

Scanning Electron Microscopy

Bacteria on nanowire arrays were prepared for SEM by overnight fixation with 2.5% glutaraldehyde added directly to the growth media. Chips were washed with isotonic deionized water followed by dehydration in increasing concentrations of ethanol (25%, 50%, 75%, 90%, 100%, 10 min each), and then transferred into hexamethyldisilazane (HMDS) (Aldrich) for 1 hour.[32] Chips were air dried overnight. Prior to imaging, chips were cleaved along the middle and sputtered with ~3 nm of Au (Denton Vacuum, LLC). Bacteria on nanowire arrays were imaged at 5 keV/12 μA by field emission SEM (JEOL FSM6430).

Planktonic bacteria collected from the bulk solution for cell length measurement were fixed as above. Prior to dehydration, fixed cell suspensions were vacuum filtered onto 0.1 μm polycarbonate membranes (Isopore Membrane Filter, EMD Millipore) sputtered with ~10 nm of Au, followed by dehydration and HMDS treatment, and another 3 nm of sputtered Au. SEM images were adjusted for brightness, contrast, and false colored in Adobe Photoshop.

Cell Length and Bacteria-Nanowire Angle Measurement

All images were manually processed in ImageJ for cell length and angle measurements. Cell length histograms were generated for varying conditions. To determine the statistical significance of changes in each cell length distribution histogram, a cumulative distribution curve was constructed and the two-sample modified Kolmogorov-Smirnov test statistic and accompanying significance level, α, for each growth condition relative to normal conditions was calculated.[29] Histograms of same growth conditions with different nanowire array periodicities, same NaCl concentration with different pressures, and similar pressures with different NaCl concentrations were also evaluated for statistically significant differences.

Derjaguin-Landau-Verwey-Overbeek Modelling

To model the colloidal interaction between bacteria and nanowire, free energy curves were generated based on Derjaguin-Landau-Verwey-Overbeek (DLVO) theory, considering the total interaction energy as the sum of a van der Waals attractive potential and an electrostatic double layer repulsive potential. For this model, though the surface properties of *S. ovata* are unknown, parameters typical of bacteria cells were selected to illustrate general trends in bacteria-nanowire interactions. The zeta potential for bacteria and metal oxide surfaces were chosen as -20 mV and -40 mV, respectively. The Hamaker constant was selected as 6.5×10^{-21} J. The minimum separation distance (where the primary minimum was defined) was selected at 0.158 nm, corresponding to the typical van der Waals radius of bacteria outer membrane surface.[18,19,23]

For the unaligned attachment scheme (bacteria perpendicular to nanowire), bacteria and nanowires were treated as spheres of radius 250 nm. To provide a first order approximation of the aligned attachment scheme (bacteria parallel to nanowire), an aspect ratio of 4:1 was assumed, resulting in interaction energy curves 4 times that of the perpendicular attachment scheme, scaling the interaction energy with surface area. Curves were generated for an ionic concentration of 100 mM and 300 mM. Kinetic activation energy barrier for attachment and detachment were calculated by the difference between the primary maximum and the secondary minimum, and the primary maximum and primary minimum, respectively.

Chapter 2

Self-photosensitization of Non-photosynthetic Bacteria for Solar-to-chemical Production

Abstract:

Improving natural photosynthesis can lead to the sustainable production of chemicals. Neither purely artificial nor purely biological approaches seem poised to realize the potential of solar-to-chemical synthesis. We developed a dual/hybrid approach whereby we combined the highly-efficient light harvesting of inorganic semiconductors with the high specificity, low-cost, and self-replication/self-repair of biocatalysts. We induced the self-photosensitization of a non-photosynthetic bacterium, *Moorella thermoacetica* with cadmium sulfide (CdS) nanoparticles, enabling the photosynthesis of acetic acid from CO_2. Biologically precipitated CdS nanoparticles serve as the light harvester to sustain cellular metabolism. This self-augmented biological system selectively produced acetic acid continuously over several days of light/dark cycles at relatively high quantum yields, demonstrating a self-replicating route towards solar-to-chemical CO_2 reduction.

2.1 Introduction:

The necessity of improving the natural mechanisms of solar energy capture for sustainable chemical production[33] has motivated the development of photoelectrochemical devices based on inorganic, solid-state materials.[34] Although solid-state semiconductor light absorbers often exceed biological light harvesting in efficiency,[35] transduction of photoexcited electrons into chemical bonds (particularly towards multi-carbon compounds from CO_2) remains challenging for abiotic catalysts.[36,37] Such catalysts struggle to compete with the high specificity, low-cost material requirements, and self-replicating/self-repairing properties of biological CO_2 fixation.[38] Thus, a likely solution must combine the best of both worlds: the light harvesting capabilities of semiconductors with the catalytic power of biology.

Several inorganic-biological hybrid systems have been devised: semiconductor nanoparticles with hydrogenases to produce biohydrogen,[39] long wavelength absorbing nanomaterials to improve the photosynthetic efficiency of plants,[40] or whole-cells with photoelectrodes for CO_2 fixation.[3,41] Whole-cell microorganisms are favored to facilitate the multi-step process of CO_2 fixation and can self-replicate/self-repair.[42] Furthermore, bacteria termed "electrotrophs" undergo direct electron transfer from an electrode.[43] However, traditional chemical synthesis of the semiconductor component often requires high-purity reagents, high temperatures, and complex microfabrication techniques. Additionally, the integration of such foreign materials with biotic systems is non-trivial.[44] Many reports have shown that some microorganisms induce the precipitation of nanoparticles,[45] producing an inherently biocompatible nanomaterial under mild conditions.

Although photosynthetic organisms can precipitate semiconductor nanoparticles, their metabolic pathways are arguably less desirable than their non-photosynthetic counterparts. Though gene modification of phototrophs has progressed,[46] non-photosynthetic bacteria remain the workhorse of synthetic biology, offering a facile route to tailoring the product diversity from CO_2 reduction.[47] Additionally, thermodynamic comparisons reveal large energetic advantages to

photosensitizing non-photosynthetic CO_2 reduction.[48] Of particular interest is the Wood-Ljungdahl pathway through which CO_2 is reduced to acetyl coenzyme A (acetyl-CoA), a common biosynthetic intermediate, and eventually acetic acid, both of which can be further upgraded to high-value products by wild-type and genetically engineered organisms.[3,49] This pathway is also used by CO_2 fixing electrotrophs, enabling the use of semiconductor photoelectrons in this energetically efficient biosynthetic route.

Here, we developed a hybrid system containing the non-photosynthetic, CO_2-reducing bacterium, *Moorella thermoacetica* (ATCC 39073) and its biologically precipitated CdS nanoparticles.[50] With an appropriate band structure, CdS is a well-studied semiconductor suitable for photosynthesis.[51] As an acetogen and an electrotroph, *M. thermoacetica* serves as an ideal model organism to explore the capabilities of this hybrid system.[52]

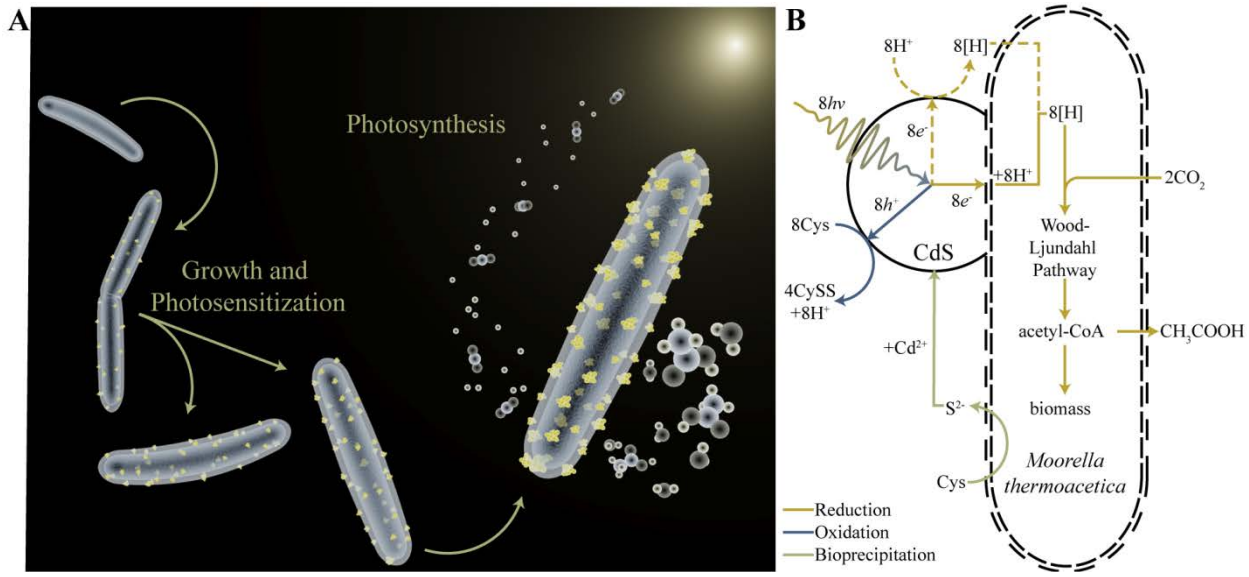


Figure 2-1. *M. thermoacetica*-CdS Reaction Schematics. (A) Depiction of the growth of *M thermoacetic*-CdS proceeding through growth of the cells and bioprecipitation/loading of CdS nanoparticles followed by photosynthesis of CO_2 to acetic acid. (B) Pathway diagram for *M. thermoacetica*-CdS. Two possible routes to generate reducing equivalents, [H], exist: generation outside the cell (dashed line), or generation by direct electron transport to the cell (solid line). Hypothesized electron transfer pathways are presented in Fig. 2-2.

The photosynthesis of acetic acid by *M. thermoacetica*-CdS is a two-step, one-pot synthesis (Fig. 2-1). First, the precipitation of CdS by *M. thermoacetica* is triggered by the addition of Cd^{2+} and cysteine (Cys) as the sulfur source.[50,53] *M. thermoacetica* utilizes photogenerated electrons from illuminated CdS nanoparticles to carry out photosynthesis (Fig. 2-1B). Absorption of a photon, $h\nu$, by CdS produces an electron-hole pair, e^- and h^+. The electron generates a reducing equivalent, [H], (see Fig. 2-2 for elaboration of this process), that is then passed on to the Wood-Ljungdahl pathway to synthesize acetic acid from CO_2. Cysteine quenches the h^+ leading to the oxidized disulfide form, cystine (CySS) (see Supplementary Discussion below for full set of reaction equations). The overall photosynthetic reaction is:

$$2\ CO_2 + 8\ Cys + 8\ h\nu \xrightarrow{M.thermoacetica-CdS} CH_3COOH + 2\ H_2O + 4\ CySS \quad (1)$$

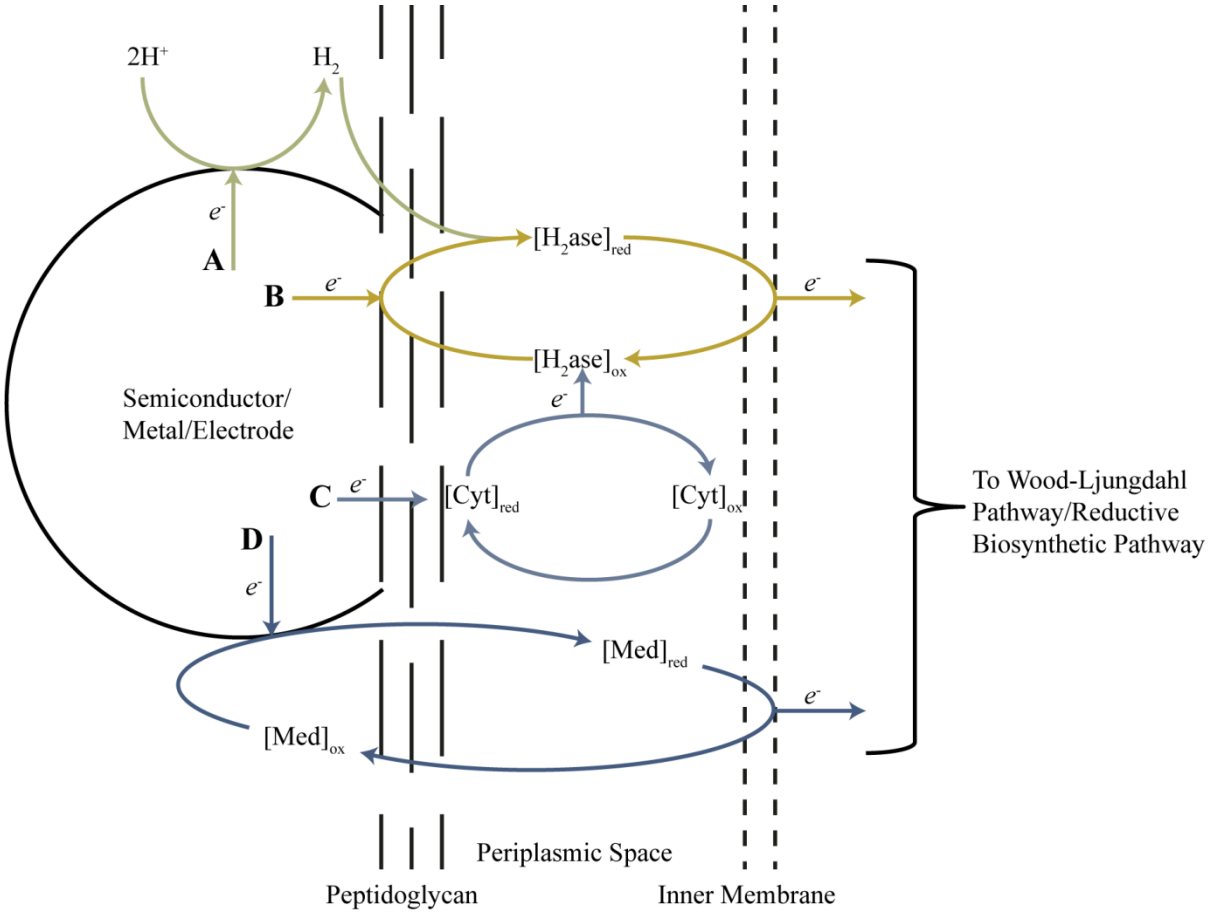


Figure 2-2. Hypothesized Electron Transfer Pathways for *M. thermoacetica*-CdS. (A) Hydrogen generation at the semiconductor surface, followed by diffusion into the cell. (B) Electron transfer directly from semiconductor to surface/membrane bound hydrogenase. (C) Electron transfer to membrane bound cytochromes. (D) Secretion of a soluble redox mediator. The proposed full and balanced reaction pathway is depicted in Fig. 2-1B.

2.2 Growth and Characterization of *M. thermoacetica*-CdS:

Precipitation of CdS by *M. thermoacetica* was initiated by addition of $Cd(NO_3)_2$ to an early exponential growth culture of glucose-grown cells supplemented with Cys (Fig. 2-3).[50] Scanning electron microscopy (SEM), scanning transmission electron microscopy (STEM) and energy dispersive x-ray spectroscopy (EDS) mapping revealed clusters of smaller nanoparticles (<10 nm, Fig. 2-2A, B) composed of cadmium and sulfur (Fig. 2-4C, E) decorated the cell (see Fig. 2-5 for addition SEM, STEM images and EDS mapping). Absorption spectra and Tauc plots yielded a measured direct band gap of 2.51±0.05 eV (Fig. 2-6A). The slightly larger measured band gap compared to bulk CdS (2.42 eV) suggests quantum confinement expected of sub-10 nm particles.[51] Powder x-ray diffraction (XRD) displayed broad peaks consistent with small particles of the wurtzite phase (Fig. 2-6B).

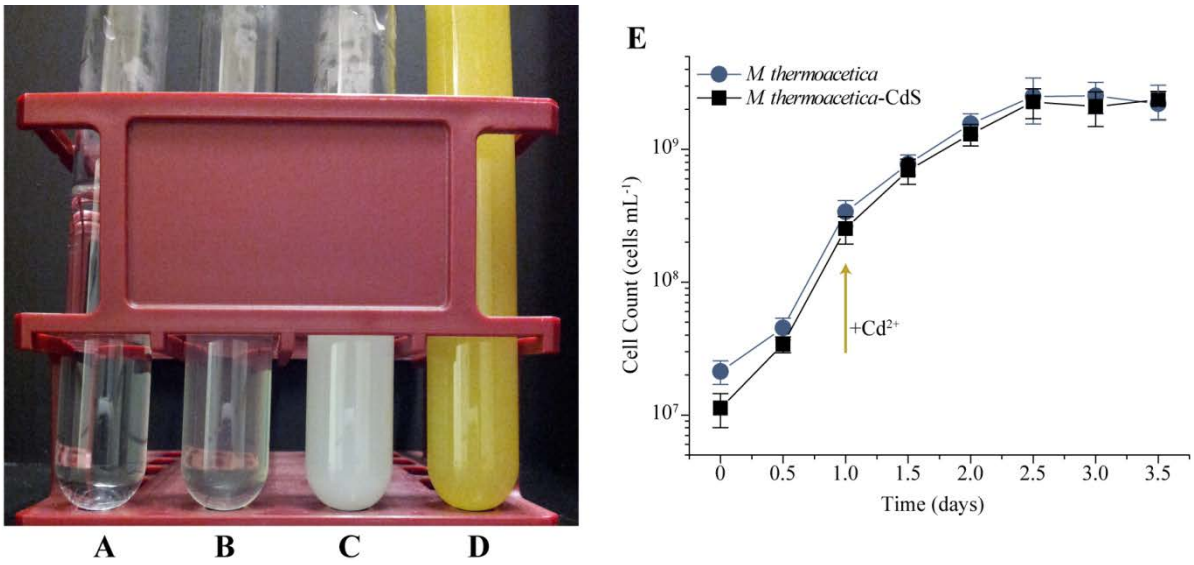


Figure 2-3. Culture Tubes of *M.thermoacetica*-CdS and Growth Kinetics. (A) Undefined medium (UDM) with 1 mM $Cd(NO_3)_2$ (no bacteria). (B) UMD with *M. thermoacetica* 24 hours after inoculation (at point of Cd^{2+} addition). (C) *M. thermoacetica*-CdS 24 hours after Cd^{2+} addition (48 hours total culture time). (D) *M. thermoacetica*-CdS 48 hours after Cd^{2+} addition (72 hours total culture time). (E) Growth Kinetics for *M. thermoacetica*-CdS. Growth kinetics obtained by manual cell count for *M. thermoacetica* grown on 50mM glucose with and without Cd^{2+} addition at 24 hours.

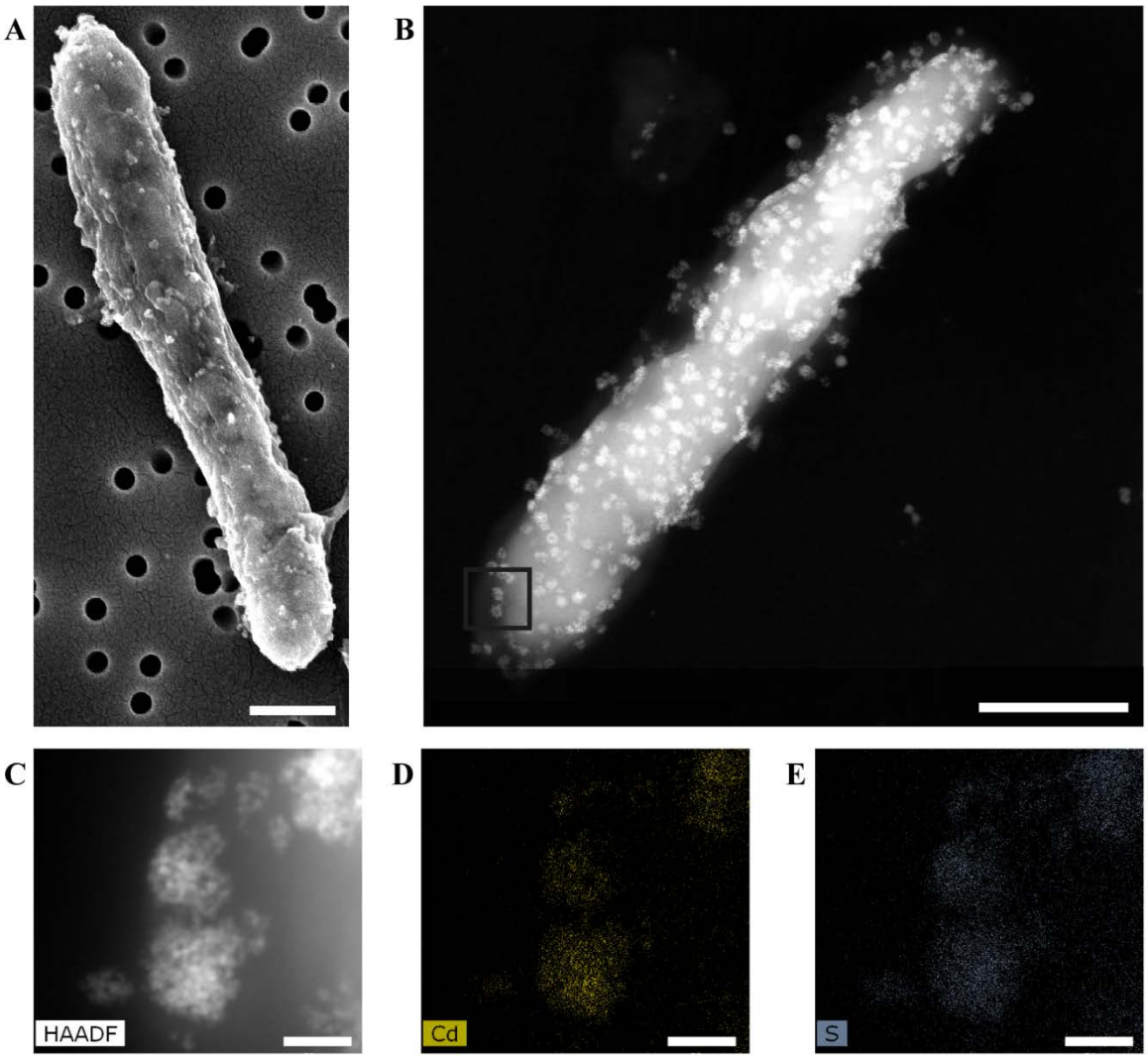


Figure 2-4. Electron Microscopy of *M. thermoacetica*-CdS Hybrids. (A) SEM image of CdS nanoparticles on *M. thermoacetica*. (B) High Angle Annular Dark Field (HAADF) STEM image of a single cell showing clusters decorated across the entire cell. (C) HAADF image and EDS mapping showing clusters mainly composed of (D) cadmium and (E) sulfur. Further elemental mapping is provided in Fig. 2-5. Scale bars are (A and B) 500 nm, (C to D) 50 nm.

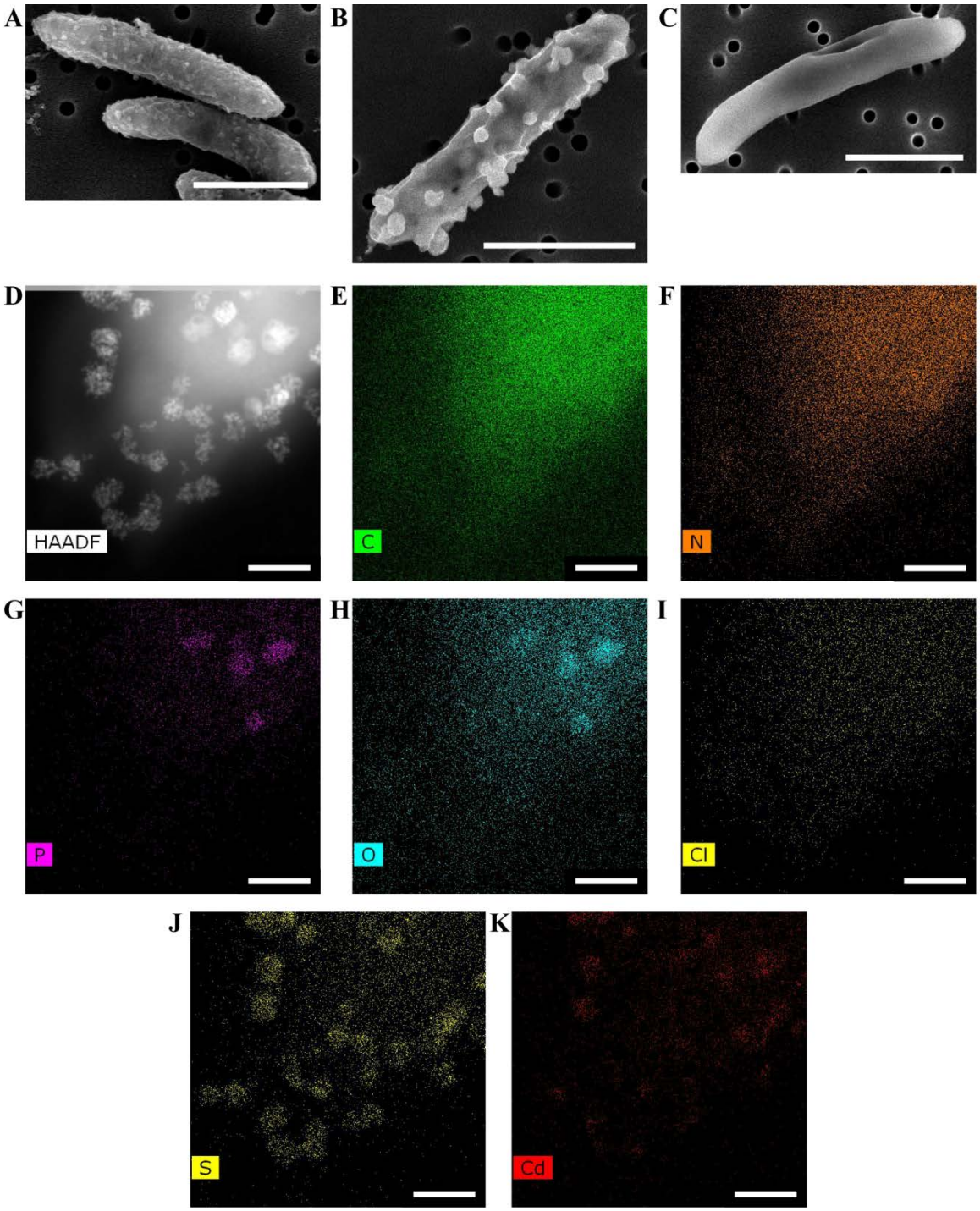


Figure 2-5. Additional Electron Microscopy of *M. thermoacetica*-CdS Hybrids. (A) Additional SEM images of *M. thermoacetica*-CdS. (B) larger particles obtained after additional ripening. (C) A CdS free cell for reference. The cell body can be distinguished by the presence of biologically common elements such as (B) carbon (C) nitrogen (D) phosphorous (E) oxygen (F) chlorine and (G) sulfur. Of note is the formation of nanoparticle clusters with bright Z-contrast on the bacteria composed largely of (H) cadmium and (G) sulfur. Scale bars (A to C) 1μM, (D to K) 100 nm.

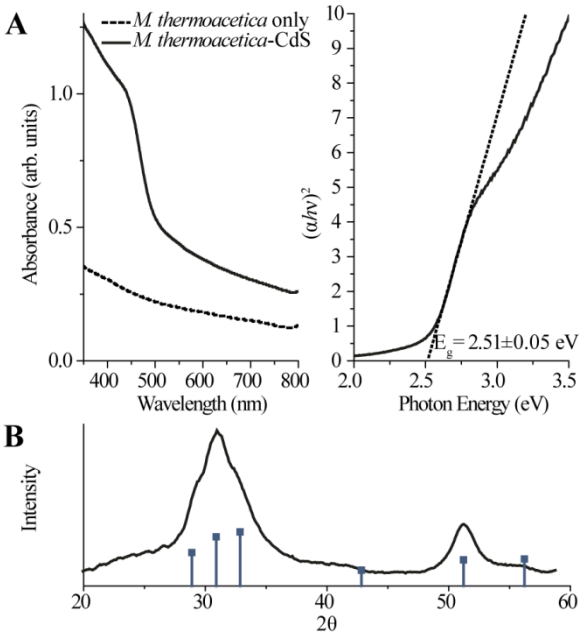


Figure 2-6. Characterization of CdS Nanoparticles. (A) UV-Vis Spectrum of *M. thermoacetica*-CdS hybrids demonstrating a band gap, E_g, of 2.51±0.05 eV. (B) XRD reveals peaks assignable to the pattern of wurtzite CdS (reference peaks from JCPDS data card No. 00-041-1049 given as drop lines). These peaks appear broad due to the small size of the nanoparticles.

2.3 Photosynthetic Performance of *M. thermoacetica*-CdS:

To confirm photosynthesis, a series of deletional controls were carried out in which *M. thermoacetica*, CdS, and light were systematically removed (Fig. 2-7A, B). In the absence of light (405±5 nm), acetic acid concentrations measured by quantitative proton nuclear magnetic resonance (^{1}H-qNMR) spectroscopy decreased (from ~2 mM accumulated under initial H_2:CO_2 acclimation) potentially due to a dark catabolic process. The viability determined by colony forming units (CFU) assays slowly declined to ~25% after 4 days (initially $5.9\pm0.4\times10^4$ CFU mL^{-1} and $1.7\pm0.4\times10^9$ cells mL^{-1}) indicating that *M. thermoacetica*-CdS requires light to maintain viability. The viability of bare *M. thermoacetica* without CdS dropped to 0% within the first day under light, consistent with previous observations of semiconducting/insulating precipitates having a photoprotective role towards bacteria.[54] Only *M. thermoacetica*-CdS hybrids with light produced acetic acid. The ^{1}H-qNMR spectrum revealed acetic acid to be the only CO_2 reduction product, confirming the high selectivity expected of biological catalysts (Fig. 2-8). After the first 1.5 days, the rate of production began to plateau because of the limiting amounts of the sacrificial reductant, Cys.

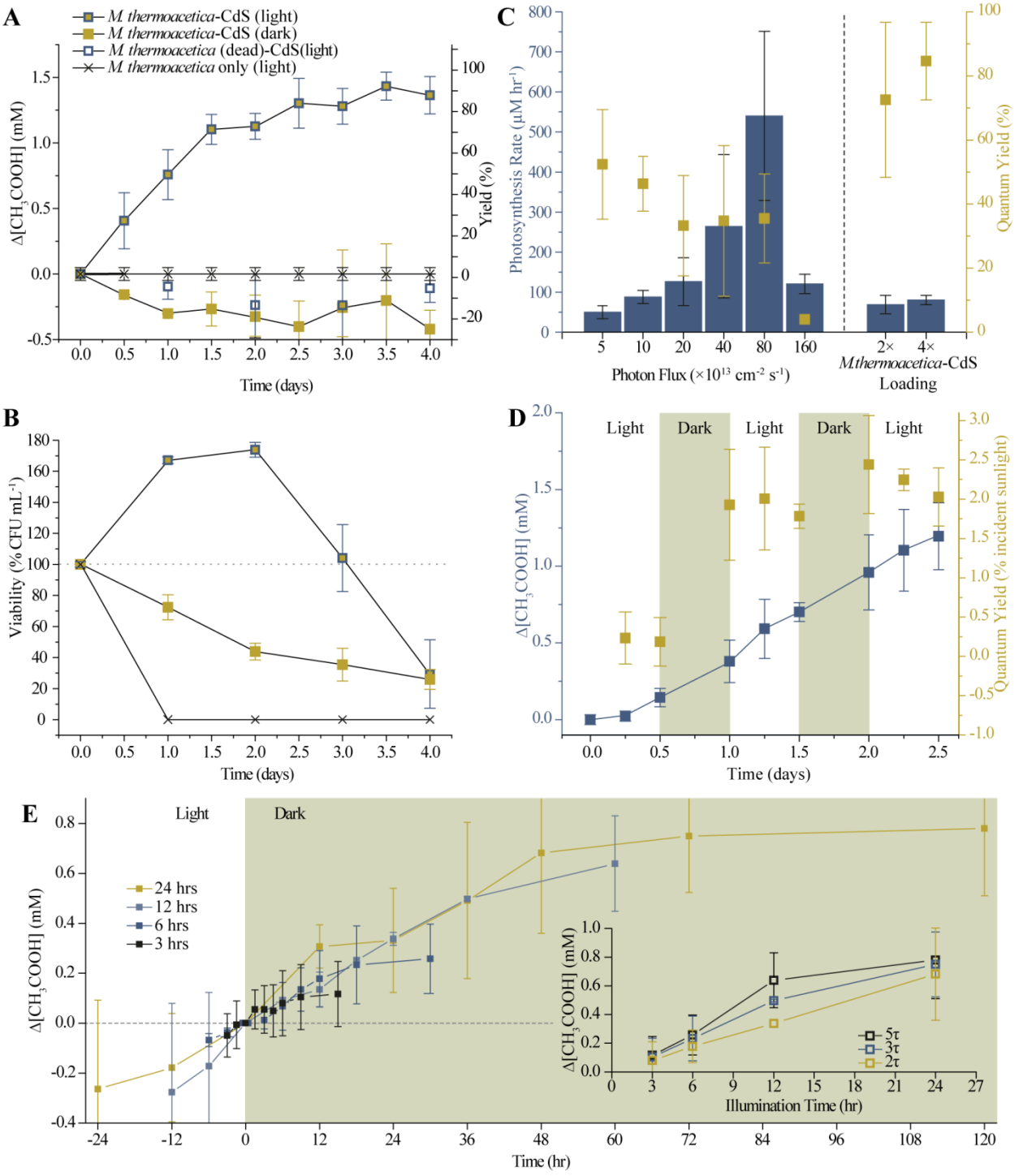


Figure 2-7. *M. thermoacetica*-CdS Photosynthesis. (A) Photosynthetic production of acetic acid for *M. thermoacetica*-CdS. Key applies to (A, B) (B) CFU viability assays. (C) Performance under increasing illumination intensities and *M. thermoacetica*-CdS concentrations. (D) Photosynthesis under low intensity simulated sunlight with light/dark cycles. (E) Acetic acid production in dark for varying illumination times. Inset shows the relation between illumination time, τ, and acetic acid yield at increasing multiples of τ in dark. All values and error bars represent the mean and error propagated standard deviation of triplicate experiments.

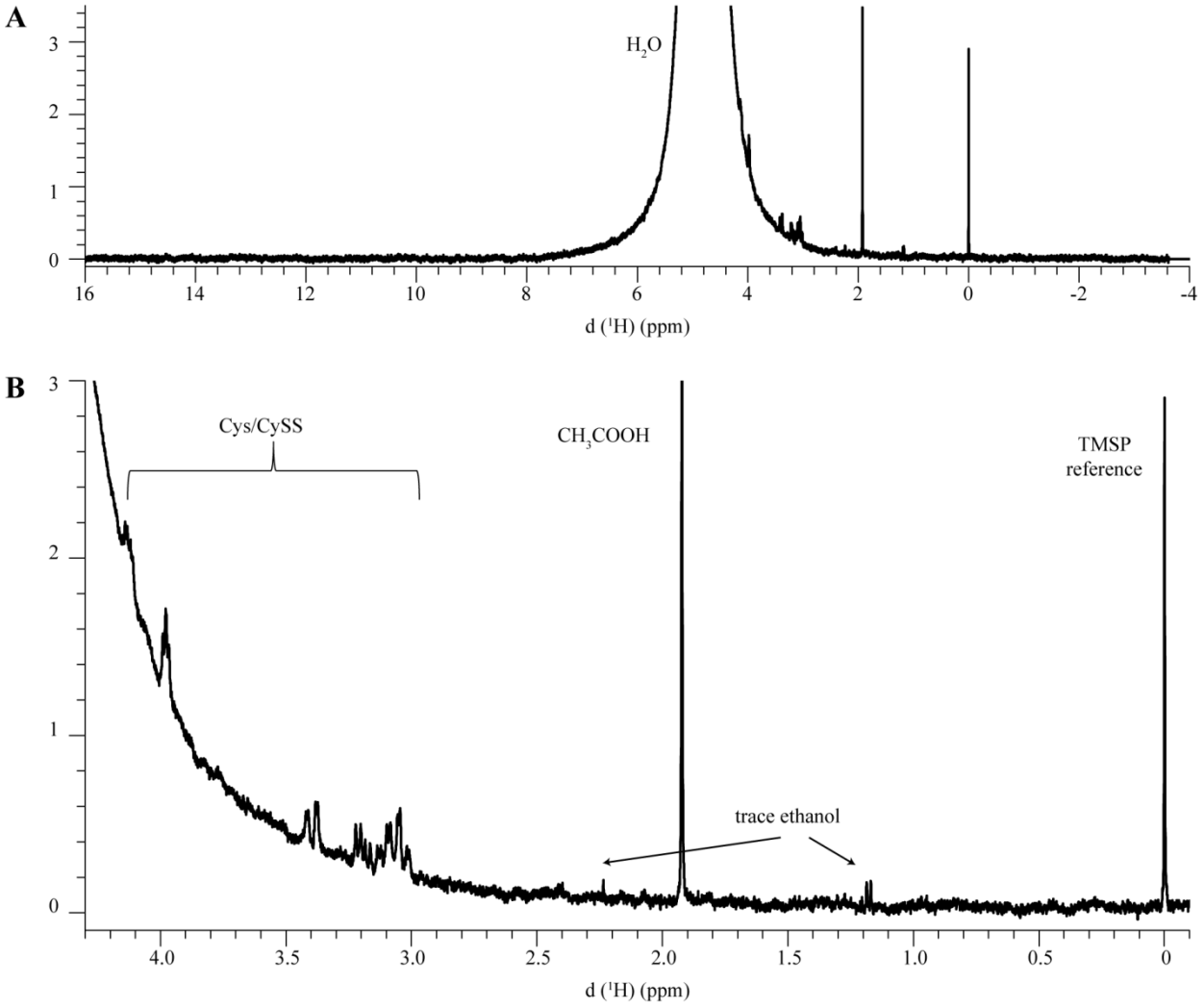


Figure 2-8. ^{1}H-NMR Spectrum of Photosynthetic Products. (A) Full spectrum shows a prominent solvent peak (H_2O). No significant products detected at chemical shifts larger than the solvent peak. (B) Inset of (A) shows the primary product detected is acetic acid (CH_3COOH), with a collection of peaks assignable to Cys/CySS. Trace peaks assignable to ethanol are occasionally observed, but these arise from residual amounts remaining from sterilization techniques.

We calculated a maximum yield of ~90% acetic acid (based on the initial Cys concentration), which is consistent with previous observations that ~10% of reduced CO_2 under the Wood-Ljungdahl pathway is directed towards cell biomass [55]. Under photosynthesis, both the viability and cell counts of *M. thermoacetica*-CdS nearly double after the first day (Fig. 2-9), on par with the doubling time of autotrophic growth (~25 hrs). Although the growth is not vigorous and perhaps limited by the total amount of CdS and other nutrients, these results suggest the possibility of a completely self-reproducing hybrid organism sustained purely through solar energy. After the third and fourth day, viability decreases, coincidental with the depletion of Cys, leading to oxidative photodamage (Fig. 2-10).

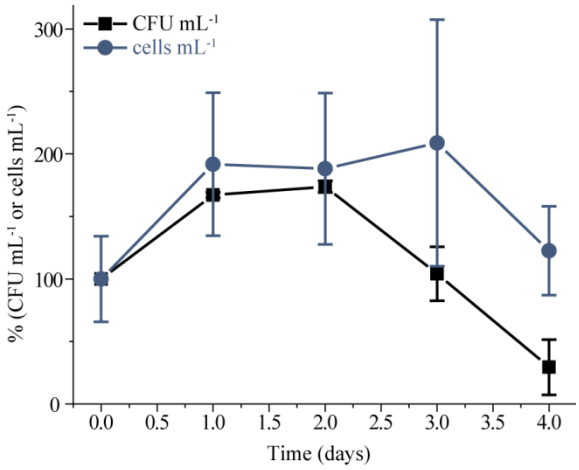


Figure 2-9. CFU and Cell Counts for *M. thermoacetica*-CdS During Photosynthesis. Data was obtained by the CFU assay and manual counting with a Petroff-Hauser counting chamber as detailed in Materials and Methods. Measurements were performed in parallel with the data presented in Fig. 2-7A, B. Both an increase in CFU mL^{-1} and cells were observed under illumination. All values are the mean and error propagated standard deviation of triplicate experiments.

Under increasing blue light (435-485 nm) flux, the rate of acetic acid production increased (Fig. 2-7C). At 5×10^{13} photons cm^{-2} s^{-1}, a quantum yield of 52±17% was observed. The rate of photosynthesis increased up until 160×10^{13} photons cm^{-2} s^{-1} when the rate dramatically decreased and the quantum yield dropped to 4±1%, possibly due to photooxidative degradation under high light intensities.[56] Under high light flux, large holes formed in the cell surface, and in some cases, resulted in the complete destruction of the cell membrane (Fig. 2-10). The high quantum yield of *M. thermoacetica*-CdS is notable given that previous analogous systems often report quantum efficiencies of ~20%.[39] This result is rationalized by the low light flux of these measurements, which reduces losses from recombination.[57] With four times the normal *M. thermoacetica*-CdS loading, we measured a quantum yield of 85±12% (Fig. 2-7C). Under higher concentrations, the average flux per bacteria decreased, correlating with increased quantum yield.

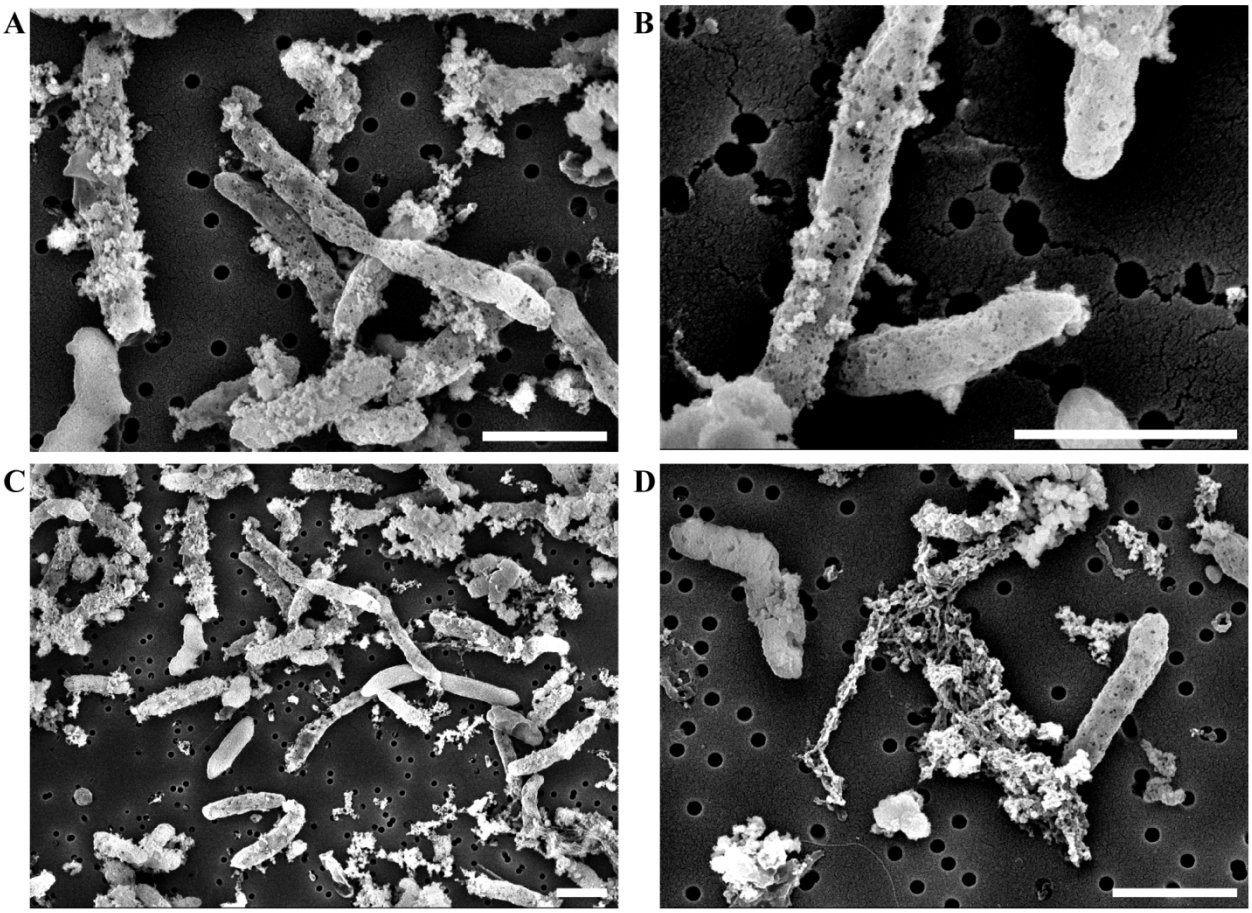


Figure 2-10. SEM of Photooxidative Damage to *M. thermoacetica*-CdS. Samples were taken from the experiments presented in Fig 2-7. All scale bars 1 μm.

To further characterize their photosynthetic behavior, *M. thermoacetica*-CdS was illuminated under low-intensity simulated sunlight (AM 1.5G spectrum, 2 W m^{-2}) with a 12 hr light/dark cycle to mimic day/night cycles (Fig. 2-7D). Unexpectedly, acetic acid concentrations not only increased under illumination, but continued to increase through the dark at the same rate through several light/dark cycles. A potential explanation lies in the accumulation of biosynthetic intermediates during the light cycle, which are then utilized during the dark cycle. These may include a number of reductive species (e.g., NADH, NADPH, ferredoxin), or intermediates in the Wood-Ljungdahl pathway such as acetyl-CoA.[58] A proton gradient may also be storing energy for ATP synthesis in the dark. Further experiments varying the duration of the light cycle (Fig. 2-7E) revealed a proportionality between the length of illumination, τ, and the dark acetic acid yield. Although the initial rate during and just after illumination appears to be relatively constant—consistent with a zeroth order catalytic reaction—the yield begins to plateau after 2τ, exhibiting a linearity between illumination time and acetic acid yield (Fig. 2-7E, inset). However, at 5τ, the 24 hr illuminated sample breaks this trend. These observations suggest that up through 12 hours of illumination, some intermediate accumulates, giving proportional dark acetic acid yield. Beyond this, the intermediate may saturate, giving no further acetic acid yield with longer illumination. We measured a peak quantum yield of 2.44±0.62% of total incident low-intensity simulated sunlight (Fig. 2-7D). These quantum yields are order-of-magnitude comparable with the year-long averages determined for plants and algae, which range from ~0.2-1.6%.[33]

2.4 Growth, Characterization and Photosynthetic Performance of *M. thermoacetica*-PbS:

The relatively large band gap of CdS limits the maximum theoretical photosynthetic efficiency of hybrid organisms, suggesting improvements may be realized by precipitation of lower band gap semiconductors. To explore this idea, 1 mM of $Pb(NO_3)_2$ was added to *M. thermoacetica* cultures as before at various time intervals after initial inoculation. These cultures ripened to dark red to brown suspensions after a total of 3 days of growth. Optical characterization of suspensions revealed significant light absorption throughout the visible portion, extending to the near IR (NIR) (Fig. 2-11A). Tauc plot analysis yielded direct band gaps of 1.20-1.97 eV, significantly larger than the 0.4 eV of bulk PbS, suggesting significant quantum confinement.

These *M. thermoacetica*-PbS suspensions were subjected to simulated sunlight photosynthetic conditions as was *M. thermoacetica*-CdS to analyze the effect of increased light absorption from the smaller band gap of PbS. Despite the increased light absorption, all *M. thermoacetica*-PbS hybrid organisms displayed lower photosynthetic acetic acid production rates (Fig. 3-12A). This poorer performance likely results from the increased toxicity of Pb compared to Cd. Comparison of dark acetic acid production rates under H_2:CO_2, all *M. thermoacetica*-PbS samples demonstrate lower performance (Fig. 2-12B). Notably, the performance decreases with increasing time of Pb addition (coincident with increasing band gap). These results suggest that smaller PbS may favor transport and diffusion of toxic Pb^{2+} into the cells, decreasing their viability and lowering acetic acid production, both in light and dark. From this, it is clear that increased solar-to-chemical efficiency must be realized only with less toxic small band gap semiconductors.

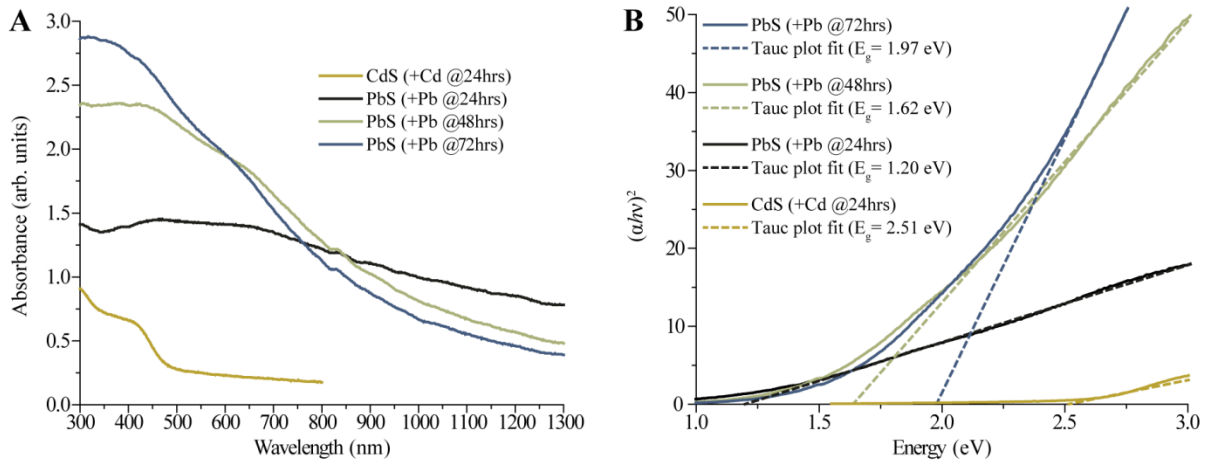


Figure 2-11. Optical Characterization of *M. thermoacetica*-PbS. (A) UV-Vis-NIR of *M. thermoacetica*-PbS with Pb addition at differing times during growth showing a tunable absorption. *M. thermoacetica*-CdS given as reference. (B) Tauc plot of *M. thermoacetica*-PbS showing decreasing band gap energies as Pb was added earlier during growth.

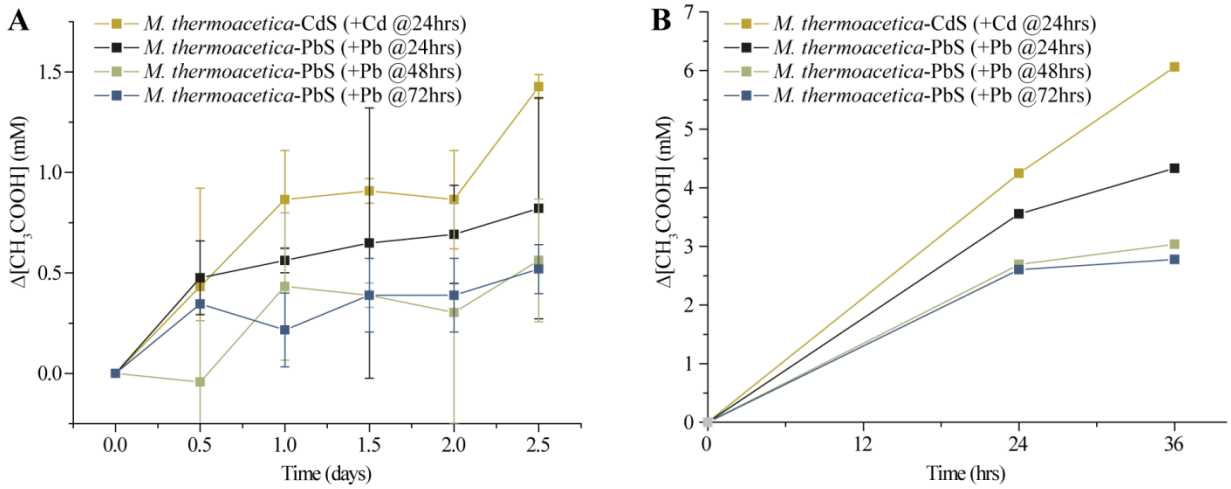


Figure 2-12. Acetic Acid Production of *M. thermoacetica*-PbS. (A) Photosynthetic production of acetic acid shows lower acetic acid production rates despite smaller band gap energy. (B) Dark synthesis of acetic acid from H_2:CO_2 show decreasing yields as Pb was added later during growth of *M. thermoacetica*.

2.5 Conclusions:

Biological routes to solid-state materials have often struggled to compete with high-quality, traditionally synthesized materials. This work demonstrates not only that biomaterials can be of sufficient quality to carry out useful photochemistry, but in some ways may be more advantageous in biological applications. Most traditional nanoparticle syntheses require organic capping ligands to control particle shape. These ligands present a barrier to charge transfer between semiconductor and catalyst, often relying upon electron tunneling.[44] The ligand-free approach taken here may help to establish a favorable interface between bacteria and semiconductor, resulting in improved efficiencies. Additionally, metal chalcogenides (such as CdS) have found limited application due to oxidative photodegradation. The ability of bacteria to

precipitate metal chalcogenides from the products of photodissolution, (Cd^{2+} and oxidized sulfur complex ions) suggests a potential regenerative pathway to circumvent the debilitating photoinstability through a precipitative self-regeneration.

Surprisingly, *M. thermoacetica*-CdS displays behavior that may help it to exceed the utility of natural photosynthesis. First, quantum yield increased with higher *M. thermoacetica*-CdS concentrations. The ability to tune the effective light flux per bacteria by simply changing the concentration of the suspension is a large advantage over similar light management practices in natural photosynthesis achieved through genetic engineering of chloroplast expression.[59] Secondly, the catabolic energy loss observed in natural photosynthesis during dark cycles was absent in *M. thermoacetica*-CdS, which may be an innate feature of the Wood-Ljungdahl pathway, in which acetic acid is a waste product of normal respiration. Additionally, many plants and algae tend to store a large portion of their photosynthetic products as biomass, which requires significant processing to produce useful chemicals. In contrast, *M. thermoacetica*-CdS, directs ~90% of photosynthetic products towards acetic acid, reducing the cost of diversifying to other chemical products.

To improve this system, greater utility could be gained by substituting Cys oxidation with a more beneficial oxidation reaction, such as oxygen evolution, wastewater oxidation for water purification, or oxidative biomass conversion.[60,61] Expanding the material library available through biologically induced precipitation will increase light absorption and raise the upper limit on bacteria/semiconductor photosynthetic efficiency. The availability of genetic engineering tools for *M. thermoacetica*,[62] as well as introduction of electrotrophic and nanoparticle precipitation behavior in model bacteria such as *Escherichia coli*,[63,64] suggests a potential role for synthetic biology in rationally designing such hybrid organisms.

Beyond the development of advanced solar-to-chemical synthesis platforms, this hybrid organism also holds potential as a tool to study biological systems. The native integration of semiconductor nanoparticles with bacterial metabolic processes provides a unique optical tag for the study of microbial behavior, such as semiconductor-bacteria electron transfer,[65,66] by providing a sensitive, non-invasive, non-chemical probe.

2.6 Materials and Methods:

Growth of *M. thermoacetica*-CdS:

Anaerobic media was prepared with three formulations in deionized (DI) water: undefined precipitation medium (UPM), defined photosynthesis medium (DPM) and undefined solid media (USM) as given below:

Component	UPM (g L^{-1})	DPM (g L^{-1})	USM (g L^{-1})
Salt Mix:			
NaCl	0.40	0.40	0.40
NH_4Cl	0.40	0.40	0.40
$MgSO_4 \cdot 7H_2O$	0.33	0.33	0.33
CaCl	0.05	0.05	0.05
KCl	0.25	0.25	0.25
Phosphorus Source:			
K_2HPO_4	--	0.64	0.64
β-glycerophosphate·2Na·xH_2O	0.80	--	--
Buffer:			
$NaHCO_3$	2.50	2.50	2.50
Supplemental Components:			
Wolfe's Vitamin Mix*	10 mL	10 mL	10 mL
Trace Mineral Mix**	10 mL	10 mL	10 mL
Yeast Extract	0.50	--	2.00
Tryptone	0.50	--	2.00
Agar	--	--	20.00

*From filter sterilized stock solution containing (mg L^{-1} DI):

Pyridoxine·HCl	10.0
Thiamine·HCl	5.0
Riboflavin	5.0
Nicotinic acid	5.0
Calcium D-(+)-pantothenate	5.0
Thioctic acid	5.0
Biotin	2.0
Folic acid	2.0
Vitamin B12	0.1

**From filter sterilized stock solution containing (mg L^{-1} DI):

Nitriloacetic acid	2000.0
$MnSO_4 \cdot H_2O$	1000.0
$Fe(SO_4)_2(NH_4)_2 \cdot 6H_2O$	800.0
$CoCl_2 \cdot 6H_2O$	200.0
$ZnSO_4 \cdot 7H_2O$	0.2
$CuCl_2 \cdot 2H_2O$	20.0
$NiCl_2 \cdot 6H_2O$	20.0
$Na_2MoO_4 \cdot 2H_2O$	20.0
Na_2SeO_4	20.0
Na_2WO_4	20.0

Yeast extract, tryptone, and agar were obtained from BD Biosciences, all other reagents were obtained through Sigma-Aldrich.

All gases were passed through two in-line oxygen traps (Agilent Technologies) to render anoxic prior to use.

Media (UPM, DPM, USM) were prepared by boiling an appropriate volume (100-500 mL) of DI water, salt mix, and trace mineral mix for 5 min under a continuously purged N_2 atmosphere. An additional 10 vol.% of DI was added to account for evaporation losses during boiling. The solution was then cooled to room temperature in an ice bath, and the atmosphere was switched to an 80:20 mixture of N_2:CO_2. The phosphorus source, buffer, and supplemental components were then added, and the media was allowed to purge and equilibrate at room temperature for 20 min. No adjustment of pH was necessary. Anaerobic media was then dispensed under the same atmosphere into 18 x 150 mm Balch-type anaerobic culture tubes (Chemglass Life Sciences) with butyl stoppers and aluminum crimp seals. Media was then autoclaved for 15 min at 121°C.

Stock solutions of 1 M glucose as a carbon source, 5.0 wt.% Cys·HCl as a reducing agent and sulfur source, and 100 mM $Cd(NO_3)_2$ as a cadmium source were prepared by boiling DI water for 5 min under N_2, cooling to room temperature, dissolving the respective solutes, and sealing under N_2 in 200 mL serum bottles with butyl stoppers and aluminum crimp seals. Stock solutions of glucose and Cys were autoclaved for 15 min at 121°C prior to use. All concentrations of glucose, Cys, and cadmium are given nominally, calculated from the initial volume of the media.

The Hungate technique or an anaerobic chamber (Coy Laboratory Products, Inc.) was employed in all operations to prevent exposure of the anaerobic bacteria to oxygen.

The initial inoculum of *Moorella thermoacetica* ATCC 39073 was graciously obtained from the laboratory of Prof. Michelle C.Y. Chang and recultured in UPM supplemented with 50 mM glucose and 0.1 wt.% cysteine. Late log cultures were cryopreserved in liquid nitrogen with 10% dimethylsulfoxide as a cryoprotectant.

To prepare *M. thermoacetica*-CdS hybrids, 20 mL UPM supplemented with 25 mM glucose and 0.1 wt.% cysteine was inoculated from the thawed cryopreserved stock at 5 vol.% and incubated with occasional agitation at 52°C. The headspace of each tube was pressurized to 150 kPag with 80:20 N_2:CO_2.

After 3 days of growth (OD_{600} = 0.16), the culture was reinoculated at 5 vol.% into fresh UPM (50 mM glucose, 0.1 wt.% cysteine), and incubated at 52°C. After 24 hours, 1 mM $Cd(NO_3)_2$ was added to the tubes. Each tube was returned to incubation and placed in an in-house fabricated rotator that slowly inverted each tube at a continuous rate of 4.5 min^{-1}. The suspension turned initially opaque white due to the formation of quantum confined CdS nanoparticles, and eventually ripened into an opaque yellow suspension (Fig. 3-3).

After an additional 2 days (3 days total growth), each tube was centrifuged at 2500 rpm for 30 min, washed and resuspended in an equivalent volume of DPM supplemented with 0.1 wt.% cysteine. A volume of 10mL of the suspension was distributed into clean anaerobic tubes equipped with a magnetic stir bar (sealed and autoclaved as previously described). Each tube was pressurized with 150 kPag of 80:20 H_2:CO_2 and incubated for 12-24 hours at 52 °C to promote autotrophic respiration.

M. thermoacetica-PbS was prepared similarly by substituting $Cd(NO_3)_2$ with $Pb(NO_3)$ at the same concentration. Addition of Pb^{2+} occurred 24 hrs, 48 hrs, or 72 hrs after reinoculation.

Material Characterization of *M. thermoacetica*-CdS:

The UV-Vis spectra of *M. thermoacetica*-CdS suspensions were obtained with a Shimadzu UV3101PC UV-Vis-NIR Spectrophotometer with an integrating sphere. Suspensions were diluted 8× in DI for measurements to ensure linearity under the Beer-Lambert law assumption. Band gap measurements were generated from Tauc plots assuming a 1 cm path length for each cuvette and a direct band gap transition for CdS.

Samples for XRD were prepared by drop casting *M. thermoacetica*-CdS suspensions onto quartz chips and air drying. XRD patterns were measured with a Bruker AXS D8 Advance Diffractometer with a Co Kα source.

Electron Microscopy:

Samples of *M. thermoacetica*-CdS were prepared for electron microscopy by fixing overnight in a solution of 5 vol.% glutaraldehyde in DPM at a 50:50 ratio of DPM/glutaraldehyde:*M.thermoacetica*-CdS suspension. Fixed samples were prepared for SEM by vacuum filtering onto 0.1 μm Isopore polycarbonate membrane filters (EMD Millipore) previously sputtered with ~6 nm of gold. Samples were washed by increasing concentrations of ethanol in DI water (0%, 25%, 50%, 75%, 90%, 100%, ~10 mL or 10 min each). Membrane filters were finally transferred into hexamethyldisilazane for 1 hour, then air dried overnight. An additional ~3 nm of gold was sputtered onto the samples prior to SEM mounting and imaging at 5 kV by field emission SEM (JEOL FSM6430).

Samples of fixed *M. thermoacetica*-CdS were prepared for STEM by dropping the fixed suspension onto Formvar coated Ultrathin Carbon Cu TEM grids, settling for 1 hour, and washing briefly in DI water. Grids were air dried overnight. STEM imaging and EDS mapping was performed at 80 kV with an FEI Titan microscope at the National Center for Electron Microscopy (NCEM). The EDS signal was acquired via a FEI Super-X Quad windowless detector based on silicon drift technology that was controlled by Bruker Esprit software.

Photosynthesis Measurements:

All photosynthesis measurements were conducted with the suspensions prepared as previously specified. Prior to photosynthesis, an additional 0.1 wt.% cysteine was added to each tube (total 0.2 wt.%, nominal) in part to act as a sacrificial reducing agent. Each tube was stirred magnetically at 150 rpm and heated to a measured temperature of 55 °C by means of a stirring hot plate and shallow sand bath (< 1 cm). Three illumination sources were employed: for high-throughput measurements: 1) an in-house fabricated circular LED array composed of 405±5 nm

violet LEDs with a measured photon flux of $5x10^{18}$ cm^{-2} s^{-1}, for blue light measurements, 2) a collimated Nikon C-HGFI Intensilight mercury lamp with a 435-485 nm filter (Fig. 2-13), and for simulated sunlight measurements, 3) a collimated 75 W Xenon lamp (Newport, Corp.) with an AM 1.5G filter. All light intensities were calibrated by a silicon photodiode (Hamamatsu S1787-04).

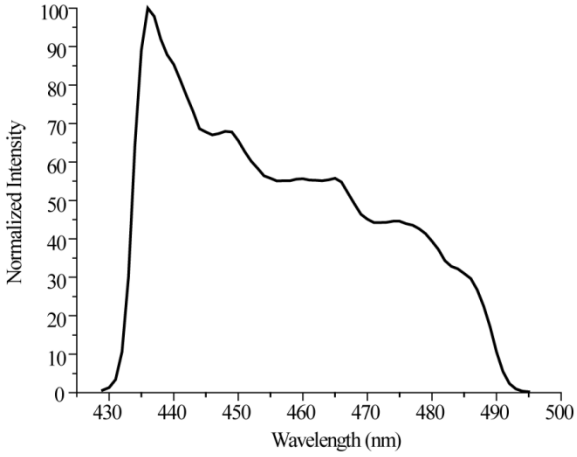


Figure 2-13. Spectrum of Blue Light Illumination Source. A Nikon C-HGFI Intensilight mercury lamp with a 435-485 nm filter was used for blue light photosynthesis quantum yield measurements.

Concentrations of photosynthesis products were measured by ^{1}H-qNMR with sodium 3-(trimethylsilyl)-2,2',3,3'-tetradeuteropropionate (TMSP-d4, Cambridge Isotope Laboratories, Inc.) as the internal standard in D_2O. Spectra were processed using Mnova NMR.

Headspace gas was periodically monitored by gas chromatography with an Agilent 3000A Micro GC (Ar carrier gas, molecular sieve column, thermal conductivity detector).

Colony Forming Unit Assay:

Colony Forming Unit Assays were performed by sampling and inoculating 0.1 mL of the *M. thermoacetica*-CdS photosynthesis suspension into 5 mL of molten (T > 50 °C) USM supplemented with 40 mM glucose and 0.1 wt.% cysteine. After thorough mixing, molten agar anaerobic tubes were quickly spun horizontally in ice water to set a thin layer of agar on the sidewalls of the anaerobic tubes. Assay tubes were pressurized to 150 kPag with 80:20 N_2:CO_2 and incubated vertically at 52 °C. After 3.5 days of growth, visible white, circular colonies were counted to determine the CFU mL^{-1} as a measure of cell number and viability. In parallel, cell mL^{-1} values were determined by manual counting with a Petroff-Hauser counting chamber.

Calculations:

Photosynthetic acetic acid yields and efficiencies were calculated based on Eq. 1.The 0.2 wt.% Cys·HCl (MW = 157.62g mol^{-1}) used in photosynthesis measurements, corresponds to 12.2 mM Cys. With the above stoichiometry, this leads to a maximum acetic acid yield of 1.53 mM CH_3COOH. Acetic acid yield is then defined as:

$$Yield_a(\%) = \frac{C_a(mM)}{1.53mM} \times 100\%$$

where C_a is the concentration of acetic acid.

The quantum yield was determined by comparison of the initial rate of acetic acid production with the measured photon flux. The reduction of two CO_2 molecules to one acetic acid molecule requires 8 electrons, giving the following quantum yield (QY) equation:

$$QY(\%) = \frac{8 \times {C_a}/{t} \times A \times V \times N_A}{\Phi_{ph}}$$

where t is the reaction time to produce C_a, A is the area of illumination, V is the volume of the *M. thermoacetica*-CdS suspension, Φ_{ph} is the measured photon flux (photons cm^{-2} s^{-1}), N_A is Avogadro's Number (6.022×10^{23}). For a lower limit of the efficiency, and to account for the possibility of scattering and reflections due to the curved sidewalls of the tubular reactor, A was assumed to be the entire surface of the reactor, or 25.4 cm^2 for a suspension volume of 10 mL.

All reported error bars represent one standard deviation from the mean average obtained from each experiment run in triplicate. All error bars on calculated values obtained after averaging were determined by the standard propagation of errors methodology.

2.7 Supplementary Discussion:

M. thermoacetica-CdS Reaction Equations:

CdS precipitation by *M. thermoacetica*:

$$Cd^{2+} + Cys \xrightarrow{M.thermoacetica} CdS + NH_3 + \text{pyruvic acid} + 2\ H^+$$

Electron-hole pair photogeneration:

$$h\nu \xrightarrow{CdS} e^- + h^+$$

Reducing equivalent generation:

$$2\ H^+ + 2\ e^- \xrightarrow{M.thermoacetica-CdS} 2\ [H]$$

CO_2 reduction to acetic acid:

$$2\ CO_2 + 8\ [H] \xrightarrow{M.thermoacetica-CdS} CH_3COOH + 2\ H_2O$$

Cys oxidation to CySS:

$$2\ Cys + 2\ h^+ \xrightarrow{M.thermoacetica-CdS} CySS + 2\ H^+$$

Overall photosynthetic reaction:

$$2\ CO2 + 8\ Cys + 8\ h\nu \xrightarrow{M.thermoacetica-CdS} CH3COOH + 2\ H2O + 4\ CySS$$

Discussion of *M. thermoacetica*-CdS growth and bioprecipitation:

Attempts to establish *M. thermoacetica*-CdS under different growth substrates yielded mixed results. In the same media, *M. thermoacetica* failed to produce CdS precipitates when grown purely on a mixture of H_2:CO_2 (80:20), the normal autotrophic growth substrate. When grown on a combination of H_2:CO_2 and glucose, formation of opaque yellow CdS occurred at a slower rate. These observations suggest that the precipitation of CdS depends heavily on the metabolic rate, pathway (fermentative glycolysis versus autotrophic respiration), protein expression under different growth substrates, or a combination of several factors. The influences of the growth substrate and the biological/chemical factors governing the formation of CdS bear further investigation to shed light on the nature of bioprecipitation processes.

Experiments in which dilute suspensions (~10-50% regular cell density) were supplemented with Cd^{2+} ions and subjected to illumination, a white precipitate was observed (which did not fully ripen to the opaque yellow suspension), suggesting photosynthetic precipitation of CdS. This contrasts sharply with the previous observation that Cd^{2+} precipitation did not occur during autotrophic growth (H_2:CO_2), the presumed pathway for photosynthetic acetic acid synthesis. The difference in biologically-induced precipitation behavior between autotrophic and photosynthetic metabolism bears further investigation.

Discussion of CFU Assays, Viability, and Self-replication:

As noted in the main text, CFU assays suggested that the photosynthetic production of acetic acid was sufficient to produce cell-replication, as evidenced by the increase in CFU mL^{-1}. It is important to note that CFU assays are not definitive, and the observed increase could be an artifact of culturing and growth conditions. To address these issues, we have cross correlated this observation with manual cell counting (Petroff-Hauser counting chamber). The rough doubling measured by CFU mL^{-1} (167±2% after the first day) correlates reasonably well with the parallel cell count (191±57% after the first day). While the CFU mL^{-1} begins to plateau after the second

day, so does the cells mL^{-1} (Fig. 2-9). While the CFU mL^{-1} begins to decline on the third day, the cells mL^{-1} does not decline until the fourth day. This is likely due to the initial cell death, followed gradually later by the photooxidative degradation (Fig. 2-10), which would result in an apparent decrease in the CFU mL^{-1} and then cells mL^{-1}, respectively.

This cross-correlation serves to rule out a few possibilities and artifacts. Firstly, no sporulation was observed at any time, suggesting that the formation of a light or nutrient-deficit triggered dormant state did not occur. While this may still imply the formation of resting cells normal in appearance, which may result in an apparent increase in CFU mL^{-1}, this would also appear as a constant cells mL^{-1}, which was not observed. Conversely, an apparent rise in cells mL^{-1} could be attributable to simply the counting of dead cells (cell staining with propidium iodide was unable to differentiate between healthy cells and ethanol killed cells). However, this would give a constant CFU mL^{-1}, which was also not observed.

It is possible that the observed cell doubling is simply due to the facile division of cells poised at the end of their division cycle. However, in order to observe the doubling seen here, that would require that nearly every cell had already doubled in cell length (but not yet divided) before illumination. We observed no such features, with a vast majority of cells existing as single cells over all time points. This suggests that cell wall biosynthesis had to predominantly occur under illumination, where light was required for acetic acid metabolism (Fig. 2-7A, B).

While the growth is not robust (as would be suggested by several doubling cycles), our observations suggest a direct correlation between *M. thermoacetica*-CdS illumination and their apparent increase in both cell number and cell viability. In experiments inoculated with 50% the normal *M. thermoacetica*-CdS loading (2× diluted), cell numbers tripled over the first 24 hours (292±69%). It is possible that the initially high concentration of bacteria quickly exhausts a limiting nutrient in the defined photosynthesis medium, allowing only one cell doubling. As noted previously, photosynthesis was not sufficient to produce fully ripened (yellow) CdS nanoparticles. It is possible the upper limit on doubling cycles is set by the CdS loading amount, in which each doubling cycle halves the average nanoparticle $cell^{-1}$ loading. These initial insights demonstrate that a fully self-replicating hybrid organism may be possible, but will require significant optimization to fully understand and rigorously demonstrate the process.

Headspace Gas Analysis During Photosynthesis:

One of the possible electron transfer mechanisms presented in Fig. 2-2 denotes that the formation of molecular hydrogen, H_2, may be generated at the CdS surface. Gas chromatographic analysis of headspace gas during photosynthesis does detect trace amounts of H_2 roughly in the range of 1-10 ppm. While it is difficult to conclude the prevalence of this reaction pathway (as H_2 may be generated at CdS, but immediately consumed by *M. thermoacetica* before it escapes to the headspace), it demonstrates that this pathway is present to some extent.

Chapter 3

Cysteine-Cystine Photoregeneration for Oxygenic Photosynthesis of Acetic Acid from CO_2 by a Tandem Inorganic-Biological Hybrid System

Abstract:

Tandem "Z-scheme" approaches to solar-to-chemical production afford the ability to independently develop and optimize reductive photocatalysts for CO_2 reduction to multi-carbon compounds, and oxidative photocatalysts for O_2 evolution. To connect the two redox processes, molecular redox shuttles, reminiscent of biological electron transfer, offer an additional level of facile chemical tunability that eliminates the need for solid-state semiconductor junction engineering. In this work, we report a tandem inorganic-biological hybrid system capable of oxygenic photosynthesis of acetic acid from CO_2. The photoreductive catalyst consists of the bacterium *Moorella thermoacetica* self-photosensitized with CdS nanoparticles at the expense of the thiol amino acid cysteine (Cys) oxidation to the disulfide form cystine (CySS). To regenerate the CySS/Cys redox shuttle, the photooxidative catalyst, TiO_2 loaded with co-catalyst Mn(II) phthalocyanine (MnPc), couples water oxidation to CySS reduction. The combined system *M. thermoacetica*-CdS+TiO_2-MnPc, demonstrates a potential biomimetic approach to complete oxygenic solar-to-chemical production.

3.1 Introduction:

Though they may project to outcompete natural photosynthesis, the conversion of solar energy into chemical bonds remains a daunting task for current artificial systems.[67] Many semiconductor light harvesters have been developed as both monolithic photoelectrodes and suspended nanoparticle photocatalysts.[68] However, the development of cheap, efficient and selective co-catalysts remains challenging for water oxidation and particularly for CO_2 reduction to multi-carbon compounds.[69] Biomimetic co-catalysts that emulate the active sites of the proteins employed within natural photosynthesis have yet to fully capture the performance of their biological inspiration due to the inherent complexity of enzyme catalysis.[70]

To skirt these difficulties, several studies have recently demonstrated the use of whole cells and whole protein complexes in solar-to-chemical production schemes.[3,41,71,72] We have recently shown the ability of the acetogenic bacterium *Moorella thermoacetica* to self-photosensitize by bio-precipitation of CdS nanoparticles, facilitating photosynthesis of acetic acid from CO_2.[73] While this system demonstrates high efficiency photoreductive capabilities, the inorganic-biological hybrid organism operates at the expense of a sacrificial reductant, the thiol amino acid cysteine (Cys), which oxidizes to the disulfide form, cystine (CySS).

Direct photooxidation of water to O_2 by *M. thermoacetica*-CdS is infeasible due to the poor oxidative stability of many metal chalcogenides.[74] We have thus taken a biomimetic approach based on the tandem "Z-scheme" design, in which photoreduction and photooxidation are carried out by two separate light harvesters and co-catalysts.[75] To balance the CO_2 photoreduction of *M. thermoacetica*-CdS, TiO_2 nanoparticles were selected due to their well characterized performance as water oxidation photocatalysts as well as their high stability.[76]

Within tandem systems, two choices for linking photoreduction and photooxidation exist: 1) a direct solid-state junction and 2) a redox mediator. Though direct contact between the two semiconductor light absorbers could afford fast electrical conduction, optimization and engineering of the junction remains non-trivial due to the formation of detrimental charge transfer barriers.[77] The junctions that form are highly dependent of the material, band structure, and doping of the semiconductor, rendering this approach non-general, thus requiring reoptimization with the discovery of new and better semiconductors light absorbers. Additionally, close proximity between oxidative and reductive processes may lead to significant back reactions at the opposing semiconductor resulting in net loss in photosynthetic products.[78] In contrast, molecular redox mediators, which are widely employed within natural photosynthesis, afford a more facile connection to biological catalysts and offer a wide range of tunability via molecular synthetic chemistry as opposed to solid-state chemistry.

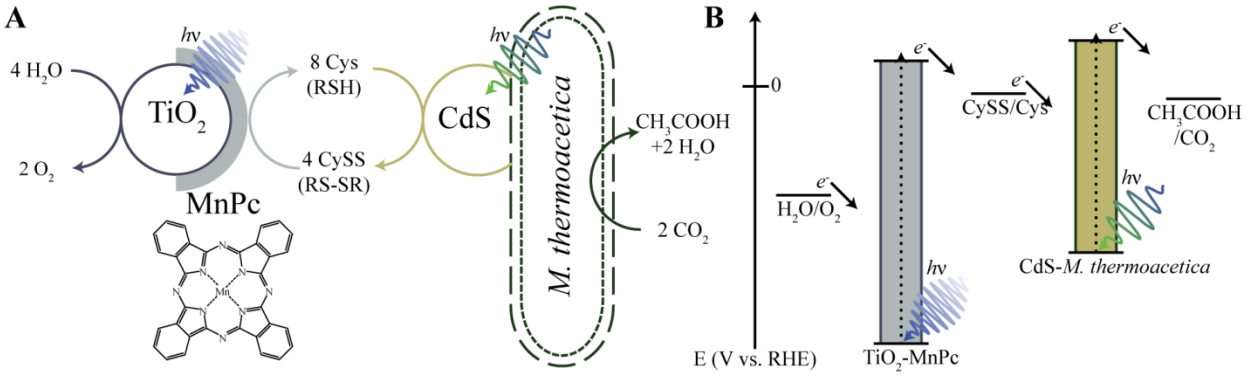


Figure 3-1. Schematic of the *M. thermoacetica*-CdS + TiO_2-MnPc Tandem System. (A) Illumination of *M. thermoacetica*-CdS drives the reduction of CO_2 into acetic acid, coupled to the oxidation of Cys to CySS. Co-illumination of TiO_2-MnPc drives the reduction of CySS back into Cys, coupled to oxidation of water to H_2O. (B) Energy level diagram depicting the relative alignment of the TiO_2 and CdS with the relevant redox reactions.

Taking inspiration from biological redox processes, a biocompatible CySS/Cys redox couple (RSH/RSSR) was selected.[79] As depicted in Fig. 3-1, the tandem system investigated here consists of a TiO_2 nanoparticle loaded with a manganese(II) phthalocyanine (MnPc) co-catalyst to reduce CySS back into Cys, rendering the formerly sacrificial reductant into a regenerative redox couple.

3.2 Characterization of Phthalocyanine-based Cystine Reduction Photocatalysts:

The choice of a selective CySS reduction co-catalyst was crucial to prevent degradation of the CySS/Cys redox couple. Bare TiO_2 alone has been shown to be a poor photocatalyst for CySS reduction due to irreversible oxidative degradation.[80,81] Additionally, the inability of TiO_2 to absorb visible light severely limits its performance under solar illumination. Previous studies have reported on the electrochemical selectivity of various transition metal phthalocyanines (TMPc) to CySS reduction and Cys oxidation, and have suggested that MnPc displays the highest activity towards CySS reduction of the first row transition metals due to its stronger binding of Mn to CySS.[82] Several first row TMPcs and unmetalated H_2Pc were tested under *in vitro* conditions suitable for *M. thermoacetica*-CdS photosynthesis by loading on to TiO_2 nanoparticles and measuring Cys production rate under illumination (5% sun, AM1.5G).

Reflectance spectra of the TiO_2-TMPc photocatalysts were taken to confirm loading of MnPc (Fig. 3-2) and display strong retention of the absorption peaks of the molecular co-catalyst.

As presented in Tbl. 3-1, MnPc exhibited the highest activity for CySS reduction. The time series presented in Fig. 3-3 under an inert N_2 atmosphere as well 21% O_2 demonstrate that even in the presence of an oxidant, photocatalyst illumination results in net Cys production and a steady state Cys concentration. However, the rate of CySS reduction eventually plateaus as the rate of oxidation back into CySS matches that of the forward reaction. However, this insight demonstrates that the TiO_2-MnPc photocatalyst system is compatible with aerobic conditions and net O_2 production.

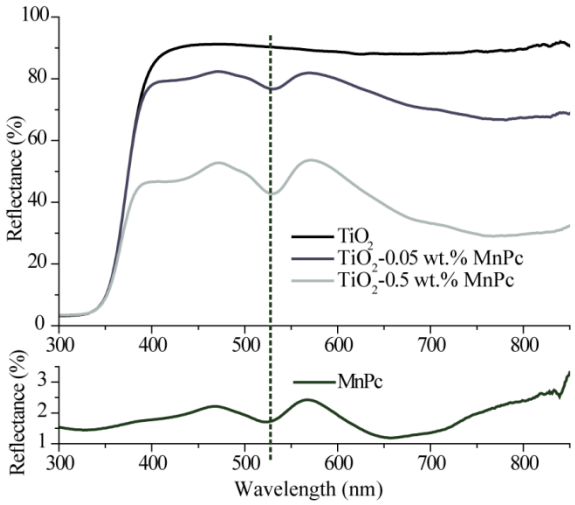


Figure 3-2. Reflectance Spectra of TiO_2-MnPc. Successful loading of increasing amounts of MnPc loaded onto TiO_2 as evidenced by sub 400 nm absorption. While the position of the peak at 530 nm remains consistent between the discrete and loaded MnPc, the lower energy peaks at ~650 nm broaden and redshift once loaded onto TiO_2.

Table 3-1. CySS Reduction Rate of Phthalocyanine Loaded TiO_2 Photocatalysts

Catalyst	Rate (μM Cys hr^{-1})
No catalyst	53.0±9.3
MnPc (0.1 wt.%)[1]	65.9±4.6
MnPc (0.05 wt.%)[1]	130.1±8.4
MnPc (0.01 wt.%)[1]	75.9±3.3
FePc[2]	61.9±4.5
CoPc[2]	56.4±2.2
NiPc[2]	87.7±18.7
CuPc[2]	68.7±5.8
ZnPc[2]	45.2±5.7
H_2Pc[2]	75.5±12.8

[1]Catalyst loading relative to mass of TiO_2. [2]Equimolar to 0.05 wt.% MnPc. Standard deviation represents error associated with linear regression of kinetic data.

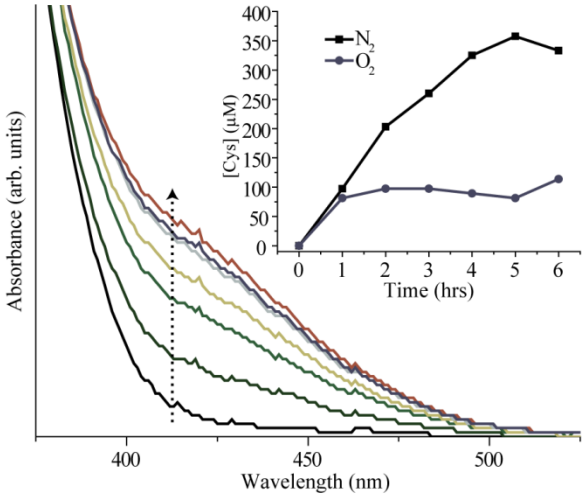


Figure 3-3. CySS Photoreduction Kinetics of TiO_2-MnPc. A colorimetric assay employing Ellman's reagent monitored the progress of Cys photogeneration. (*inset*) TiO_2-MnPc demonstrated net CySS photoreduction under both anaerobic and aerobic conditions.

The non-linear trend of CySS reduction activity with increasing an number of *d*-electrons deviates from the monotonic decreasing trend observed in previous reports.[82] Specifically, we observe a local peak in activity for NiPc and CuPc which have exhibited the poorest dark electrochemical activity. In addition, MnPc displays a significantly higher activity than all other tested Pc. While previous electrochemical studies employed relatively inert and non-interacting graphitic electrodes, reflectance spectra (Fig 3-2, 3-4) demonstrate a redshift in the low energy peaks around 650 nm, suggesting coupling between TiO_2 and MnPc. The solubility of TMPc in EtOH (the solvent used for loading) may play a role, as MnPc has the highest EtOH solubility, perhaps leading to more even loading on TiO_2 and a greater number of exposed active sites.[83] However, both NiPc and CuPc have demonstrated lower solubility than FePc and CoPc, indicating that differences in coscatalyst loading fails to sufficiently explain the activity trend.
The spectrum of TiO_2-MnPc retains the distinct peak at 530 nm found in the neat MnPc spectrum (Fig. 3-2), whereas such spectral signatures are often lost in the other TiO_2-Pc photocatalysts suggesting either poor loading, or perhaps interactions between the TMPc and TiO_2 (Fig. 3-4). However, activity does not directly correlate with reflectance spectra, as NiPc and ZnPc which show the second highest and lowest activity, respectively, have similar reflectance spectra with deemphasized features.

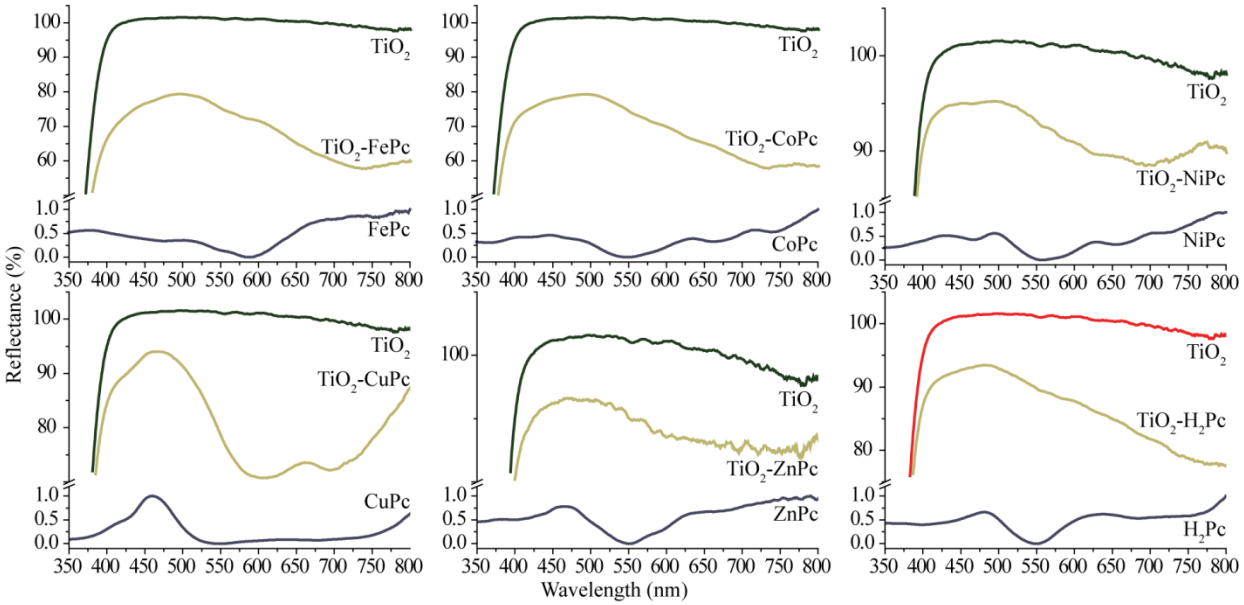


Figure 3-4. Reflectance Spectra of TMPc and TiO_2-TMPc. Spectra of TiO_2-TMPc show distinct differences from the neat TMPc. Features in the range of 400-500 nm are diminished on TiO_2, while absorption in the range of >600 nm is enhanced.

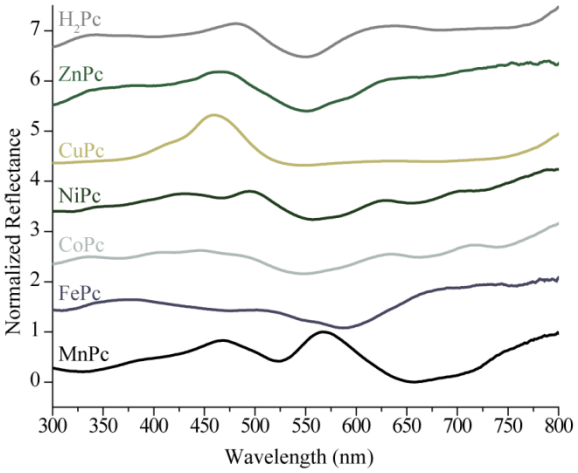


Figure 3-5. Direct Comparison of TMPc and H_2Pc Reflectance Spectra.

Since previous studies were conducted as electrocatalysts in dark, the differences in activity observed here suggest TMPc visible light absorption has an effect on catalytic performance. TMPcs have been widely employed as visible and IR sensitizers of dye-sensitized solar cells (DSSCs) due to the favorable energy alignment of their HOMO and LUMO with the conduction band of TiO_2.[84] We do note that ZnPc, a common visible light sensitizer in DSSCs, demonstrates the lowest activity, perhaps due to the favorable charge injection from ZnPc to TiO_2 that would impede CySS reduction.

The activity of NiPc deviates most drastically from previous reports. While Zagal, et al. report NiPc as one of the least catalytically active for CySS reduction, photocatalytically, NiPc was the second most active behind MnPc. Analysis of the MO diagram of NiPc shows that the HOMO-LUMO charge transfer is a ligand-to-metal charge transfer (LMCT) from the Pc a_{1u} to

the Ni $3d_{x^2-y^2}$ centered b_{1g}.[85] This shift of electron density towards the metal active site under illumination may improve CySS binding and increase reduction activity. In contrast, FePc and CoPc, the least photocatalytically active, exhibit largely metal-to-ligand charge transfer (MLCT) which may disfavor CySS binding. A similar LMCT argument may explain the higher activity of CuPc. H_2Pc also demonstrates reasonable activity towards CySS reduction despite not having a metal site to facilitate disulfide binding. However, the close proximity of two hydrogens may favor a proton-coupled electron transfer.

3.3 Photosynthetic Performance of *M. thermoacetica*-CdS+TiO_2-MnPc Tandem System:

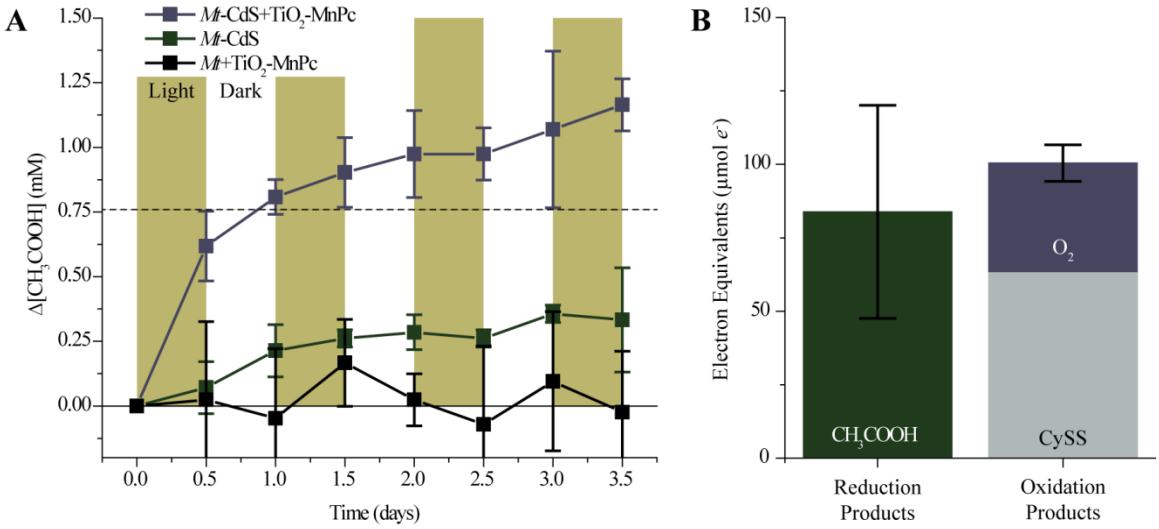


Figure 3-6. Photosynthetic Performance of *M.thermoacetica*-CdS and TiO_2-MnPc Tandem System. (A) Comparison of *M.thermoacetica*-CdS and TiO_2-MnPc with controls show greater acetic acid production from the combination of the tandem system. Both *M. thermoacetica*-CdS only and *M.thermoacetica*+TiO_2-MnPc controls showed lower acetic acid production below the stoichiometric limit imposed by Cys (dashed line). (B) Comparison of acetic acid ($8e^-$) and O_2 ($4e^-$) yields after 3.5 days. Electrons potentially derived from the next oxidation of Cys to CySS ($2e^-$) indicated to balance electron equivalents between acetic acid and O_2. All values represent the average and standard deviation of triplicate experiments.

Illumination of various combinations of *M. thermoacetica*-CdS and TiO_2-MnPc demonstrated that the CySS photoregenerative catalyst effectively pairs with the CO_2 photoreductive catalyst (Fig 3-6). When only *M. thermoacetica*-CdS was illuminated, the rate of acetic acid production leveled off after roughly 1 day, below the stoichiometric limit set by Cys as limiting reagent (i.e. no photoregeneration). Similarly, combination of TiO_2-MnPc with CdS-free *M. thermoacetica* cells yielded negligible acetate production (Fig. 3-6A). While the band gap of TiO_2 is thermodynamically sufficient to drive microbially catalyzed CO_2 reduction, the process remains kinetically unfavorable due to the poor interface between TiO_2-MnPc and *M. thermoacetica*. TiO_2 may also photosterilize *M. thermoacetica* in the absence of CdS nanoparticles via the formation of reactive oxygen species (ROS).[86] Finally, the combination of *M. thermoacetica*-CdS for CO_2 reduction to acetic acid and Cys oxidation, coupled with TiO_2-MnPc for CySS reduction and water oxidation produced a net amount of acetic acid at a higher rate than *M. thermoacetica*-CdS alone, and above the stoichiometric limit of Cys, clear evidence

of CySS/Cys as a regenerative redox couple. The photoprotective role of TiO_2 (in addition to the protection afforded by CdS alone) may also help to explain the higher photosynthetic rate of *M. thermoacetica*+TiO_2-MnPc compared to *M. thermoacetica*-CdS alone.[54] Comparison of electron yields for the reduced product (acetic acid) and oxidative products (O_2 and CySS) show comparable stoichiometries (Fig. 3-4B). A slight excess of oxidative products are indicated due to potential loss of acetic acid towards *M. thermoacetica* biomass.[55] Additionally, as CySS participates within the redox cycle, CySS derived electron equivalents indicated in Fig. 3-6B are slightly overestimated.

3.4 Conclusion:

While the current system demonstrates reasonable net kinetic performance, several improvements could be made to further increase the photosynthetic rate. As seen in both Fig. 3-3 (inset) and Fig. 4-4A, the rate of CySS reduction or acetic acid production begins to decrease from the initial rate, likely due to the effects of O_2 accumulation. As the partial pressure of O_2 rises, the back reaction of Cys oxidation begins to compete, giving a steady state concentration of Cys below the ~6 mM desired for high CO_2 reduction rates by *M. thermoacetica*-CdS. Additionally, the O_2 sensitivity of CdS and the anaerobic *M. thermoacetica* likely limit their performance at higher O_2 concentrations.[87] While engineering approaches such as gas purging could limit the detrimental effects of O_2, a more elegant solution would call for physically separating the two incompatible processes through either physical space, or *via* a selective membrane.[88] While physically separating the oxidative and reductive photocatalysts would create significant difficulties for solid-junction nanoparticle tandem systems, the use of a molecular redox shuttle enabled by diffusional or convective transport renders this design readily accessible.

The limited light absorption of TiO_2 and CdS likely bottlenecks the solar-to-chemical efficiency of the current system. Exploration of the semiconductor parameters space may yield lower bandgap semiconductors to raise the theoretical limit on solar-conversion efficiency. Due to the relative ease of engineering molecular rather than solid-state interfaces, the various components of this modular tandem inorganic-biological hybrid system may be switched out as newer, better performing materials become available. With these advances, this paradigm holds promise for the future of advanced solar-to-chemical production.

3.5 Materials and Methods:

All reagents were used as received without further purification and were purchased from Sigma-Aldrich with the exception of zinc phthalocyanine (Acros Organics), cobalt(II) phthalocyanine (Alfa Aesar), and nickel(II) phthalocyanine (Eastman Kodak). Reagents related to the growth of *M. thermoacetica* (ATCC 39073) and photosynthesis characterization were described previously.[73]

Preparation of TiO_2-TMPc Photocatalyst

Phthalocyanines were loaded onto TiO_2 nanoparticles (Sigma-Aldrich 637254, anatase, <25 nm) by suspending both at the desired ratio in 50 mL of ethanol and 50 μL of 1 M HCl in a 100 mL beaker. The suspension was sonicated with a Microtip Probe Sonicator for 15 min intervals at 21% amplitude and allowed to settle. The solvent was removed by rotary evaporator and stored until further use.

Cystine Photoreduction Assay

Oxygen free 1,4-piperazinediethanesulfonic acid (PIPES, 30 mM) buffered media was made by boiling DI water under a N_2 stream for 5 min. The pH was adjusted to 7 by addition of 10 M NaOH. To the cooled PIPES buffer was added 10mM cystine. Each TiO_2-Pc composite was suspended in the cystine buffer at 0.1 g L^{-1} and sealed in a Balch type anaerobic tube under an N_2 atmosphere. The suspensions were irradiated by a filtered 75 W Xenon lamp (Newport Corp., AM1.5G, 5% sun) for 2 hours with time points taken at 0, 0.25, 0.5, 1 and 2 hrs. Cysteine production was determined photometrically by addition of an equal volume of 5 mM Ellman's reagent in degassed ethanol (freeze-pump-thaw). The mixture was allowed to react and then centrifuged to remove the photocatalyst and quantified by UV-Vis spectrophotometry (Shimadzu UV3101PC UV-Vis-NIR Spectrophotometer with an integrating sphere). Reflectance spectra were obtained by suspending the photocatalysts or TMPc in ethanol and drop casting onto glass cover slips until an opaque film formed.

Preparation and Photosynthesis Assay of *M. thermoacetica*-CdS+TiO_2-MnPc

M. thermoacetica-CdS was prepared and assayed as previously described with modifications noted below.[73] All techniques were conducted anaerobically under an oxygen-free atmosphere or using standard Hungate technique. Briefly, cryopreserved stocks of *M. thermoacetica* (ATCC 39073) was inoculated at 5 vol.% into undefined precipitation media (UDM) with 25 mM glucose, 0.1 wt.% cysteine·HCl, 250 kPa N_2:CO_2 (80:20) and incubated at 52°C for 3 days until OD_{600}=0.16. The suspension was reinoculated at 5 vol.% into fresh UDM with 50 mM glucose and 0.1 wt.% cysteine·HCl. After 24 hrs of incubation as before, 1mM $Cd(NO_3)_2$ was added. The culture was incubated an additional 2 days with frequent agitation. After 2 days, the yellow suspension was centrifuged under an inert atmosphere and resuspended in half the original volume (5 mL) of defined photosynthesis media (DPM) supplemented with 0.1 wt.% cysteine·HCl and 250 kPa H_2:CO_2 (80:20). The suspension was incubated for 24-36 hrs before the headspace was exchanged for N_2:CO_2 (80:20). Deletional controls (*M.thermoacetica*-CdS, *M.thermoacetica*+TiO_2-MnPc) were prepared in a similar fashion.

The 0.05 wt.% TiO_2-MnPc was suspended in DPM at 1 g L^{-1} and sonicated for 1 hr. To the above *M. thermoacetica*-CdS suspension was added 5mL of the TiO_2-MnPc suspension. The complete 10 mL of *M. thermoacetica*-CdS+TiO_2-MnPc was illuminated by a filtered 75 W Xenon lamp (AM1.5G, 5% sun) with a 12 hrs light/12 hrs dark cycle with heating and stirring

(55 °C, 150 rpm). The suspensions were sampled every 12 hrs. Liquid sample time points were centrifuged to remove cells and nanoparticles and assayed for acetic acid concentration by quantitative ^{1}H-NMR with trimethylsilylpropionate as an internal standard. Oxygen production as monitored by a Neofox in-situ optical oxygen monitoring probe (Ocean Optics, Inc.).

Chapter 4

Spectroscopic Elucidation of Picosecond Energy Transfer Pathways in Hybrid Inorganic-Biological Organisms for Solar-to-Chemical Production

Abstract:

The rise of inorganic-biological hybrid organisms for solar-to-chemical production has spurred forth mechanistic investigations to uncover the dynamics of the biotic-abiotic interface and drive the development of next-generation systems. The model system, *Moorella thermoacetica*-Cadmium Sulfide (CdS), combines an inorganic semiconductor nanoparticle light harvester with an acetogenic bacterium to drive the photosynthetic reduction of CO_2 to acetic acid with high efficiency. In this work, we report insights into this unique electrotrophic behavior and propose a charge transfer mechanism from CdS to *M. thermoacetica*. Transient absorption spectroscopy (TAS) revealed that photoexcited electron transfer rates increase with increasing hydrogenase (H_2ase) enzyme activity. On the same time scale, time-resolved infrared (TRIR) spectroscopy demonstrated new vibrational states arose in the 1700-1900 cm^{-1} spectral region. The quantum efficiency of this system for photosynthetic acetic acid production also increased with increasing H_2ase activity and shorter carrier lifetimes when averaged over the first 24 hours of photosynthesis. However, within the initial 3 hours of photosynthesis, the rate followed an opposite trend: the bacteria with the lowest H_2ase activity photosynthesized acetic acid the fastest. These results suggest a two-pathway mechanism: a high quantum efficiency charge transfer pathway to H_2ase generating H_2 as a molecular intermediate that dominates at long time scales, and a direct energy transducing enzymatic pathway responsible for acetic acid production at short time scales. The methodology and insights gained here serve as a template for future investigations into the complex biotic-abiotic interface and will catalyze crucial advances in inorganic-biological solar-to-chemical production.

4.1 Introduction:

The sluggish transduction of solar energy into chemical bonds through natural photosynthesis has strangled our efforts to harvest the full bounty of the sun's energy.[33] We have temporarily sidestepped this limitation by tapping into large reserves of carbonaceous energy to drive an exponential growth in manufacturing, agriculture, urbanization and population. However, the growing scarcity of petrochemicals has called for a return to photosynthesis - rather a new form of photosynthesis capable of keeping pace with modern society.[89,90] As a sign of progress, inorganic semiconductor light harvesters now routinely surpass the efficiency of plants.[35] In contrast, synthetic catalysts still struggle to replicate the complex C-C bond forming chemistry of biology.[37,67] Significant strides towards comprehensive solar-to-chemical production have been demonstrated through several inorganic-biological hybrid systems, combining inorganic semiconductor light harvesters with microbial CO_2 reduction.[3,41,71] Recently, we have reported the self-photosensitized hybrid bacterium, *M. thermoacetica*-CdS, that photosynthesizes acetic acid from CO_2 *via* bio-precipitated CdS nanoparticles.[91]

Though e^- transfer from electrodes to electrotrophic bacteria has been demonstrated across several genera, the mechanism remains in contention.[65] Spectroscopic investigations of bacterium-to-electrode anodic e^- transfer in electrogenic microbial fuel cells have implicated cytochrome mediated mechanisms.[92] However, analogous studies of semiconductor-to-bacterium cathodic e^- transfer in electrotrophic organisms have remained sparse. Electron transfer first to membrane bound or extracellular H_2ase to generate molecular H_2 as an intermediate followed by uptake into the native acetogenic Wood-Ljungdahl pathway (WLP) has been speculated or inferred.[66,93,94] Still, detailed spectroscopic characterization has remained elusive due to the difficulty of adapting previous techniques to solid electrode platforms. In contrast, our model system, *M. thermoacetica*-CdS, as a translucent colloidal suspension in which photoelectrons are generated by an optically addressable CdS nanoparticle, eliminates the need for opaque electrodes, thereby enabling existing transmittance based spectroscopic techniques in uncovering the molecular basis of this charge transfer mechanism (Fig. 4-1A). In this work, we present transient absorption spectroscopy (TAS) and time-resolved infrared spectroscopy (TRIR) correlated with biochemical activity to propose a model of the dynamics of inorganic-biological charge and energy transfer.

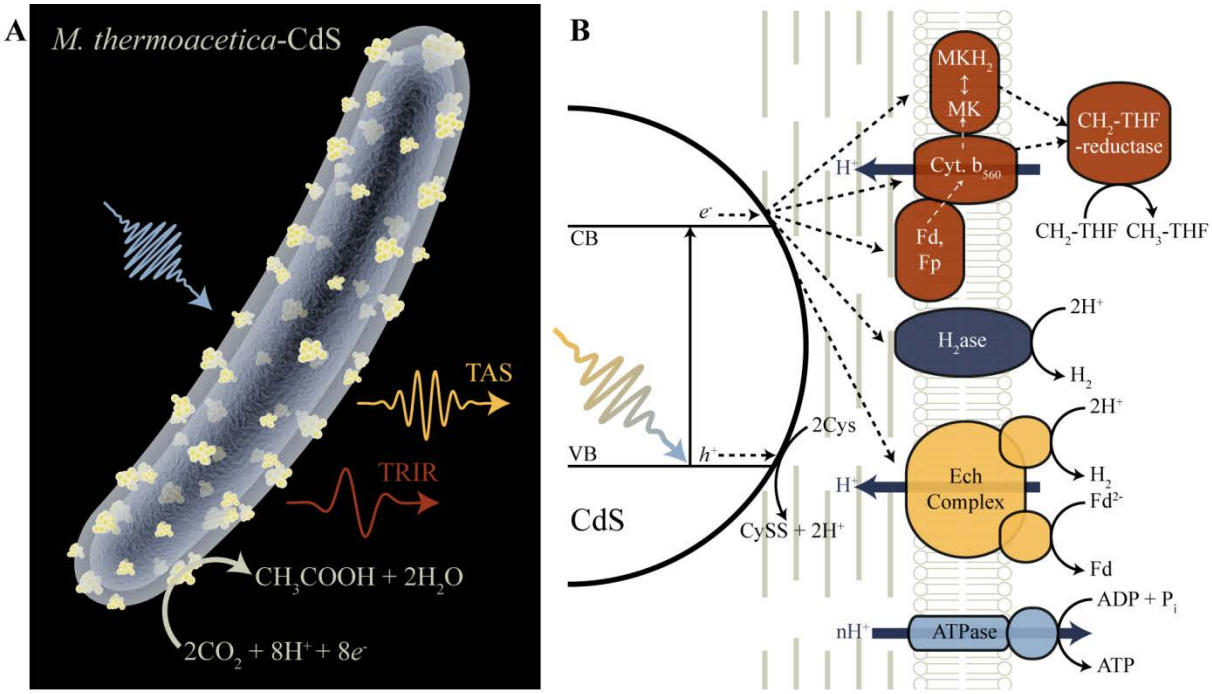


Figure 4-1. Schematic of *M. thermoacetica*-CdS Photosynthetic Charge Transfer. (A) Visible light excitation of optically addressable CdS photosensitizing nanoparticles enables photosynthetic acetic acid production from CO_2, as well as characterization by TAS and TRIR spectroscopy. (B) Potential electron transfer pathways in *M. thermoacetica*-CdS.

Upon photoexcitation of CdS, cysteine (Cys) oxidation to cystine (CySS) and H^+ quenches the valence band h^+, while the conduction band e^- may transfer to membrane bound proteins or soluble e^- acceptors. Genomic mining, enzymology, and thermodynamic comparison of protein redox potentials have proposed several viable e^- transfer pathways (Fig. 4-1B).[58,93–95] Electron transfer to membrane bound Ni-Fe H_2ases may play a significant role as H_2 directly feeds into the WLP. Demonstrations of direct e^- transfer between metal chalcogenide

nanoparticles and purified H_2ases *in vitro* lend credibility to this pathway's existence in complex whole cells.[39,96–98] Alternative pathways have implicated e^- transfer first to membrane bound cytochromes, ferredoxin (Fd), flavoproteins (Fp) and menaquinones (MK).[93,94] While these pathways may generate reducing equivalents, implicitly, they must also couple to the generation of a H^+ gradient to facilitate ATP generation by ATPase. The generation of this proton motive force, either through the transmembrane Ech complex or simply through surface proximal Cys oxidation, may be crucial to electrotrophic behavior, as a related acetogen, *Acetobacterium woodii*, which instead utilizes a Na^+ motive force, notably cannot engage in electrotrophy.[43,58]

4.2 Photo-biochemical Characterization of *M. thermoacetica*-CdS

To investigate the possibility of H_2ase mediated e^- transfer, *M. thermoacetica*-CdS was incubated from 0 to 48 hrs on H_2 (H_2:CO_2, 80:20, henceforth referred to as H_2 incubated) or glucose (25 mM) to vary the expression and activity of H_2ase. Activity was assayed photometrically by standard benzyl viologen reduction in the presence of H_2 (Fig 4-2A, 4-3).[55,99]

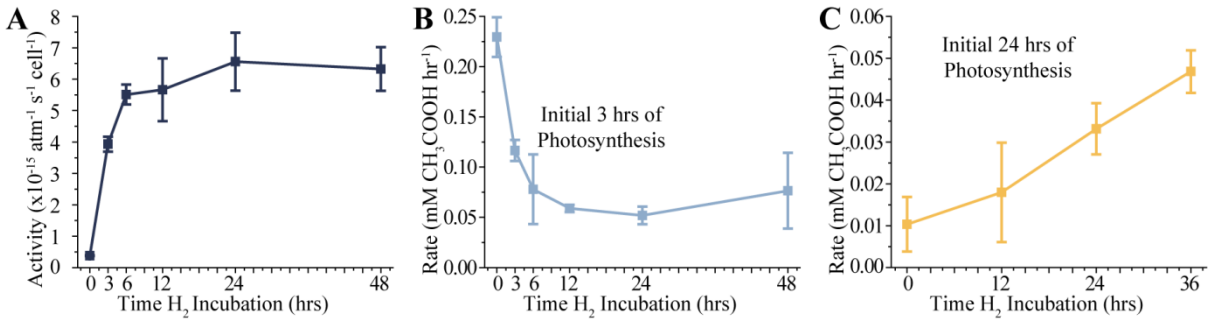


Figure 4-2. Biochemical Assays of *M. thermoacetica*-CdS. (A) H_2ase activity with varying incubation time under H_2. See Methods for details of quantification. (B) CO_2-to-acetic acid conversion rates averaged over the first 3 hrs of photosynthesis show a decreasing trend with increasing H_2 incubation time. (C) CO_2-to-acetic acid conversion rates averaged over the first 24 hrs of photosynthesis show an increasing trend with increasing H_2 incubation time. Error bars represent the standard deviation obtained from triplicate experiments.

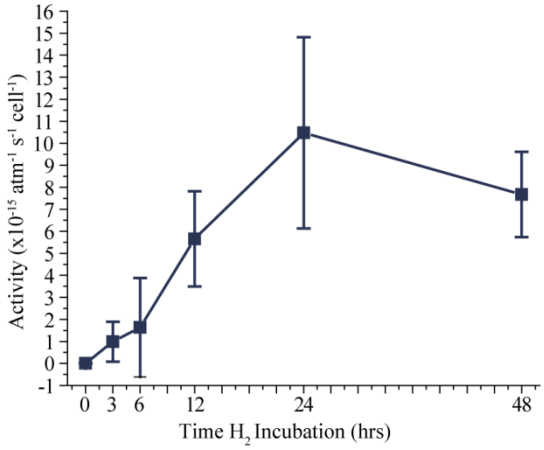


Figure 4-3. H_2ase Activity of *M. thermoacetica*-CdS with Varying H_2 Concentration. H_2ase activity was determined by variation of H_2 partial pressure with a fixed benzyl viologen concentration (supplemental to Fig. 4-2A).

Consistent with previous characterizations of *M. thermoacetica*, H_2 oxidation-benzyl viologen reduction activity increased under increasing H_2 incubation time, presumably through increased H_2ase expression. Comparison of *M. thermoacetica*-CdS incubated for 24 hrs under glucose and H_2 showed H_2ase activity of $6.56\pm0.92\times10^{-15}$ (atm s cell)$^{-1}$ and $1.85\pm8.39\times10^{-17}$ (atm s cell)$^{-1}$, respectively.

To correlate enzyme activity with photosynthetic performance, the same samples were subjected to simulated solar illumination (0.5% sun, AM1.5G) and analyzed for acetic acid production. Interestingly, during the initial 3 hrs of photosynthesis, the rate of CO_2 reduction anti-correlated with H_2ase activity, with the 0 hrs sample demonstrating the highest activity (0.23 ± 0.02 mM hr^{-1}). The 24 hrs glucose sample produced acetic acid at 0.47 ± 0.15 mM hr^{-1}, one order of magnitude faster than the 24 hrs H_2 sample. However, at longer illumination times, H_2 incubated samples demonstrated the opposite trend. When averaged over 24 hrs of illumination, photosynthesis rates increased with increasing incubation time in H_2 (Fig. 4-2C). These contrasting results suggest two competing charge transfer mechanisms: a non-H_2ase mediated pathway dominant at short time scales (<3 hrs) and a H_2ase mediated pathway dominant at long time scales (~24 hrs).

4.3 Transient Absorption Spectroscopy of *M. thermoacetica*-CdS

To delve deeper into the molecular basis of these two mechanisms, we turned to time-resolved spectroscopic techniques for a dynamic understanding of the activity trends. TAS decay kinetics followed the rate of photogenerated e^- leaving CdS for various preparations of *M. thermoacetica*-CdS (Fig. 4-4, 4-5A). A transient bleach from 440-490 nm matched typical spectra observed with CdS- e^- acceptor systems and was not observed in CdS-free *M. thermoacetica*. The spectrum of chemically precipitated CdS alone decayed much slower than *M. thermoacetica*–CdS indicating that rapid quenching may result from a proximal e^- acceptor. The H_2 incubated *M. thermoacetica*-CdS displayed even faster decay kinetics than the glucose analogue, correlating well with the higher H_2ase activity. These observations point to faster e^- transfer to an acceptor site or more e^- acceptors available in H_2 incubated bacteria.[98,100] Fitting of the TAS data to a tri-exponential decay revealed three lifetimes: a fast component in the range of 2-10 ps (τ_1), a longer component in the range of 20-80 ps (τ_2) and an even longer component in the range of several 100 ps (τ_3). A multi-exponential decay unsurprisingly indicates several processes at play in the complex *M. thermoacetica*-CdS hybrids. Rapid picosecond decays were previously measured with colloidal CdS that featured molecular acceptors with fast e^- transfer behavior.[101–103] As hot e^- relaxation in Cd-chalcogenide quantum dots occurs in the sub-picosecond regime, this process does not likely contribute to the TAS kinetics in the measured timescale.[104] However, previous studies of Fe-Fe H_2ase-CdS nanorod constructs reported TAS lifetimes in the range of 100 ns, significantly longer than the data presented here.[97,98] The discrepancy may be attributed to the presence of surface ligands (not present in *M. thermoacetica*-CdS) which present a charge transfer barrier, differences in CdS-H_2ase spatial proximity, solvent effects and reorganization energies, H-bonding networks, and the relatively impaired functionality of purified enzymes under *in vitro* vs. *in vivo* conditions.[44,105,106]

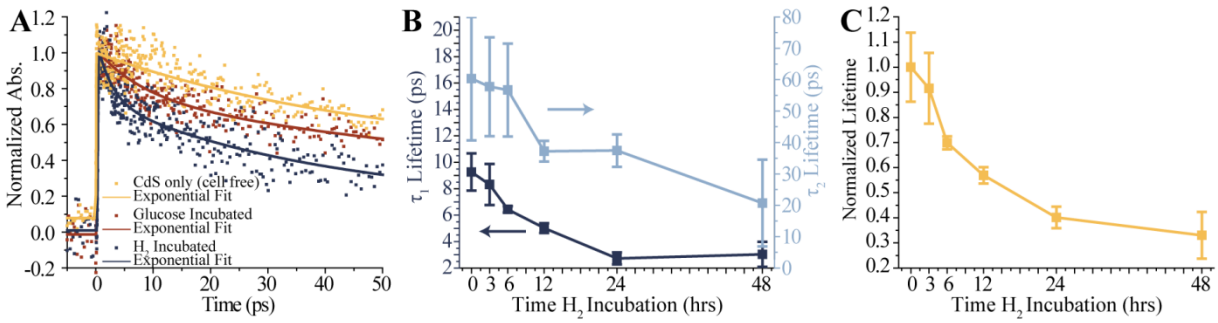


Figure 4-4. TAS of *M. thermoacetica*-CdS. (A) TAS plots of CdS only (cell-free), 24 hrs glucose incubated, and 24 hrs H_2 incubated. (B) Trends of exponential τ_1 and τ_2 lifetimes with increasing incubation time under H_2. (C) Weighted averages of the normalized τ_1 and τ_2 lifetimes with increasing incubation time under H_2. Error bars represent the standard error associated with the exponential fitting.

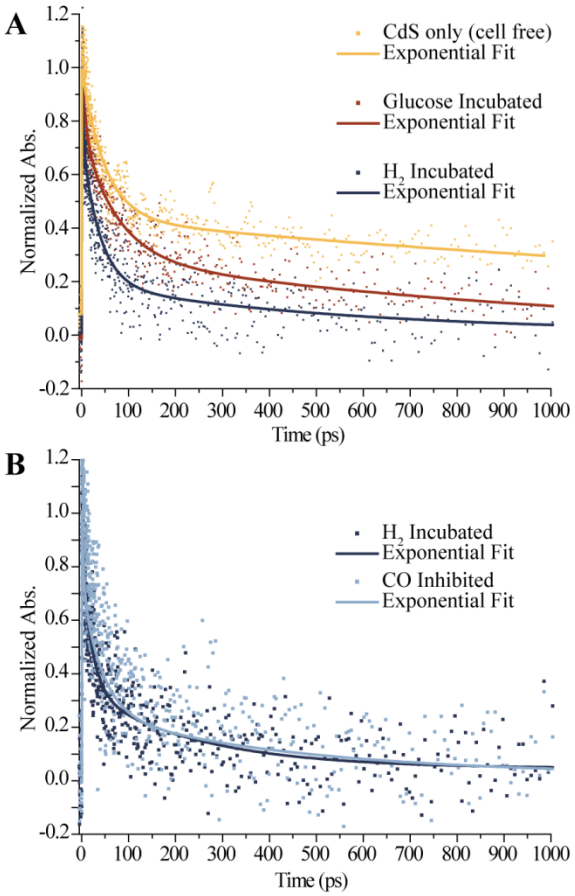


Figure 4-5. Supplementary TAS Spectra of *M. thermoacetica*-CdS. (A) Expanded time scale of spectrum presented in Fig. 5-4A. (B) Comparison of H_2 incubated and CO inhibited spectra.

The differences in lifetimes between cell-free CdS, H_2 incubated, and glucose incubated cells suggests the importance of H_2ase expression in e^- transfer kinetics. To correlate with the above H_2ase activity (Fig. 4-2A), the TAS lifetimes of the H_2 incubated time series were measured (Fig. 4-4B, C). Both the fast τ_1, τ_2 and their weighted average showed decreasing

lifetimes with increasing H_2ase activity, suggesting that the fast e^- transfer kinetics were due to an increase in H_2ase e^- acceptor sites. Inhibition of the H_2ase active site (H-cluster) with CO did not significantly change the TAS kinetics, similar to previous works, in which e^- transfer initially proceeds through the Fe-S cluster chain rather than directly to the Ni-Fe active site (Fig. 4-5B).[98,107,108]

4.4 Time Resolved Infrared Spectroscopy of *M. thermoacetica*-CdS:

While kinetically efficient e^- transfer a to membrane bound H_2ase may explain the increasing photosynthesis rates at long time scales (Fig. 4-2C), TRIR helped determine the basis of the decreasing rates seen at short time scales (Fig 4-2B).

We observed changes in the 1760-1880 cm^{-1} spectral window, roughly corresponding to the vibrational range of C, O, and N double and triple bonds, among other IR active modes characteristic of amino acid residues (Fig. 4-6).[109–111] The peaks decayed on the same timescale as the TAS signal, giving further evidence that the picosecond e^- transfer resulted from a molecular, rather than purely physical, process. No significant changes in the 1900-2100 cm^{-1} spectral window associated with the catalytic cycle of the [Ni-Fe] H_2ase H-cluster were observed, indicating that a significant quantity of photogenerated e^- were not transferred to the active site within this timeframe.[96,112,113] While the complexity of the whole cell *M. thermoacetica*-CdS system renders unambiguous peak assignment beyond the scope of these initial results, careful construction of controls yielded valuable insight into the nature of these vibrational changes.

H_2 and glucose incubated samples yielded different TRIR spectral responses. While several bleach features in the range of 1760-1820 cm^{-1} on the picosecond time regime appeared for the H_2 incubated sample (Fig. 4-6A, 4-7), in the same spectral window, glucose incubated samples showed long lived peak growth (Fig. 4-6B). These features may indicate H_2ase mediated charge transfer, with the differential response seen in glucose potentially representing an alternate pathway. In the region of 1810-1880 cm^{-1}, signal bleaches of similar time scales appeared in both H_2 and glucose incubated samples, implicating a similar e^- transfer pathway in both systems (Fig 4-6C, D). However, differences in their kinetic evolution point towards different utilization of this shared mechanism. While the pair of bands at 1823 and 1827 cm^{-1} retained a roughly 1:1 ratio for the H_2 incubated sample, in the glucose incubated sample, the 1823 cm^{-1} feature did not grow in until 1-2 ps after the pump excitation, and decayed back to zero faster than the 1827 cm^{-1} feature. Additionally, the single feature at 1842 cm^{-1} in the H_2 incubated sample blue shifted to 1845 cm^{-1} in the glucose incubated sample, temporarily forming a pair of peaks. We conclude that these spectral responses point towards different predominant e^- transfer pathways in H_2 vs. glucose incubated samples.

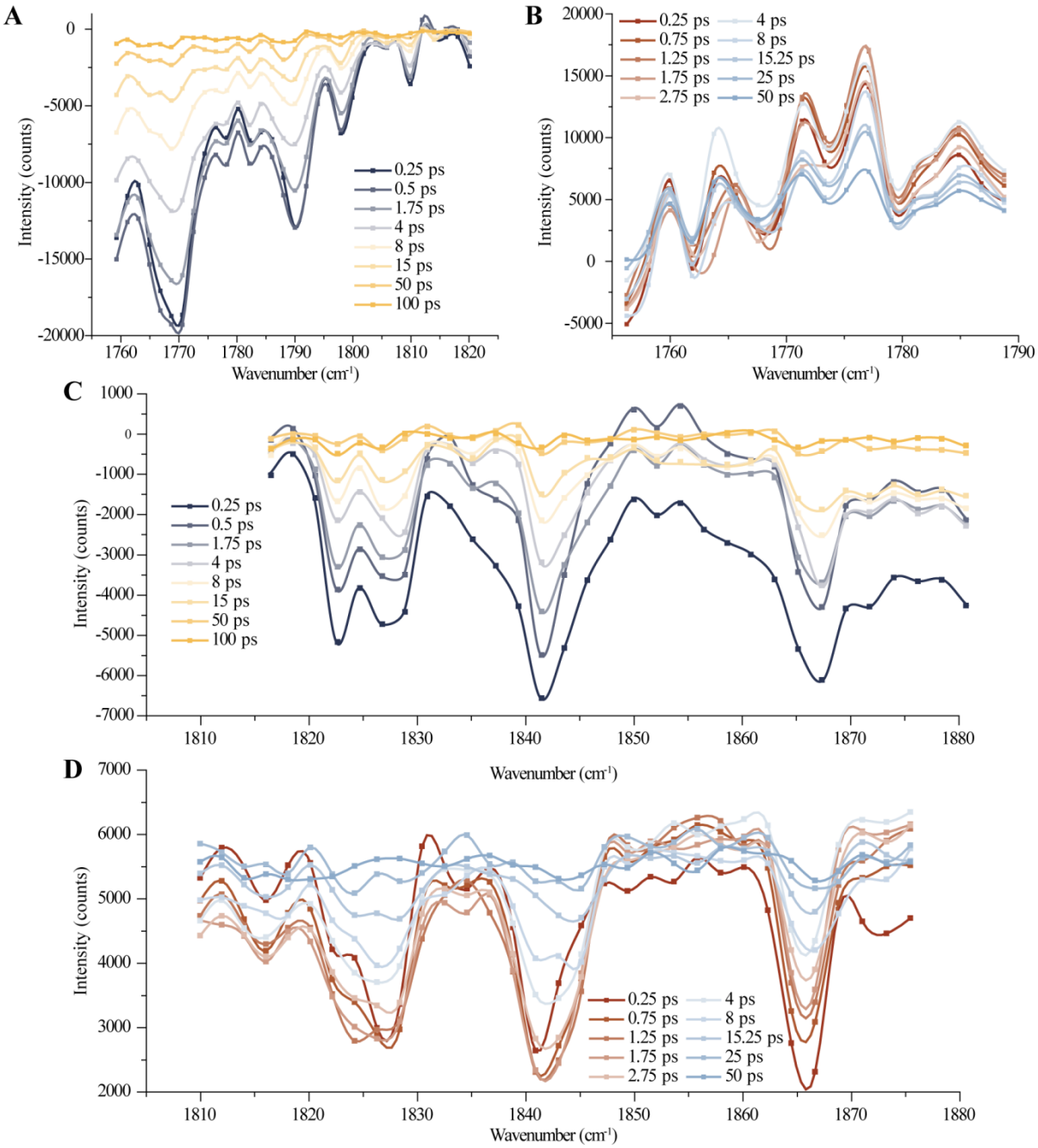


Figure 4-6. TRIR Spectra of *M. thermoacetica*-CdS. (A, C) TRIR of 24 hrs H_2 incubated *M. thermoacetica*-CdS showing bleaching of several peaks in the region of C, N, O double and triple bonds. (B, D) TRIR of 24 hrs glucose incubated *M. thermoacetica*-CdS.

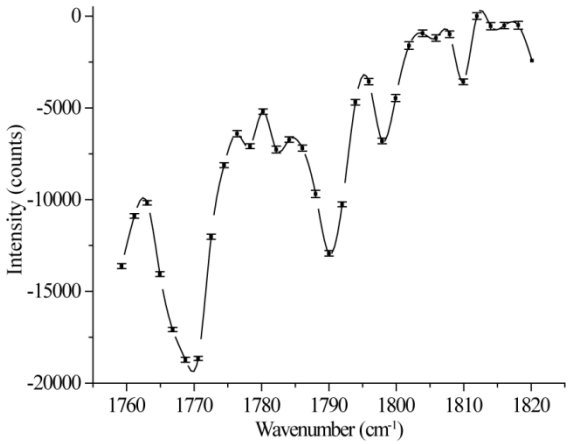


Figure 4-7. Standard Error of TRIR Spectra. Standard error associated with H_2 incubated sample.

4.5 Proposed Mechanism of *M. thermoacetica*-CdS Charge and Energy Transfer:

Taken together, the biochemical, TAS and TRIR data suggest two competing pathways for e^- transfer within *M. thermoacetica*-CdS (Fig. 4-8). Initially, low H_2ase expression favors e^- injection to a membrane bound e^- acceptor (Fd, Fp, cytochrome, MK) that generates a proton motive force for ATP generation, as well as directly reduces CH_2-THF for the final stages of the WLP. However, slower charge transfer leads to poorer quantum efficiency, likely due to e^--h^+ recombination losses. Additionally, this pathway cannot generate high energy reducing equivalents (H_2, NAD(P)H, Fd) needed for the first reductive steps of the WLP. As H_2ase expression increases, charge transfer kinetics favors e^- transfer to a membrane bound H_2ase to generate molecular H_2. While this H_2ase mediated pathway may display higher quantum efficiency, the higher photosynthetic rates only kick in once a significant concentration of extra(intra)cellular H_2 accumulates. This results in lower photosynthetic rates in the first 3 hrs with increasing H_2ase activity (e^- diverted from the non-H_2ase pathway), but eventually higher rates after 24 hrs. This H_2 then enters the normal WLP via oxidation by the HydABC complex generating both ATP and reducing equivalents.[58]

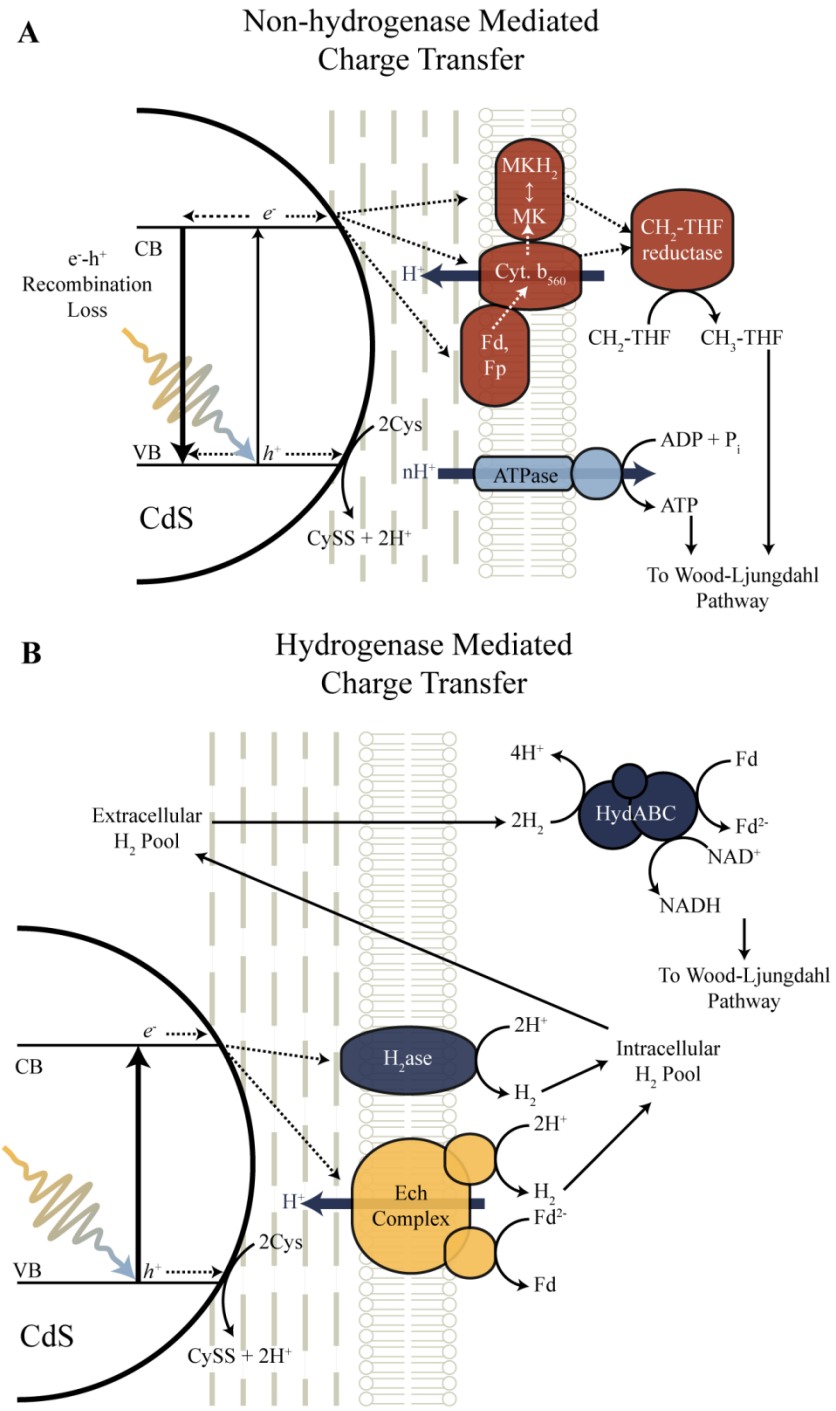


Figure 4-8. Proposed Dual Pathway of Charge and Energy Transfer in *M. thermoacetica*-CdS.(A) The proposed non-H_2ase mediated pathway predominant in glucose incubated cells, transiently faster during the initial 3 hrs of photosynthesis. (B) Membrane bound H_2ase mediated pathway dominant in H_2 incubated cells and photosynthetically faster at long time intervals.

4.6 Conclusions:

In conclusion, the work here represents an initial experimental probe into the photosynthetic, electrotrophic behavior of *M. thermoacetica*-CdS. With the careful construction of controls and mild, bio-compatible probing conditions, complex biological behaviors may be studied through conventional spectroscopic techniques. Increasing H_2ase activity correlated with more efficient long term photosynthetic rates of acetic acid generation. Evidence provided by TAS and TRIR likewise supported the existence of a picosecond charge transfer pathway that correlated well with results from biochemical characterization. Our proposed two-pathway mechanism bears further investigation to probe more acutely the molecular and enzymatic basis of this biotic-abiotic charge transfer. Such insights will ultimately lead to a deeper understanding of the burgeoning complex nexus of inorganic materials and biological systems, and provide a rational framework for the optimization and design of next generation solar-to-chemical systems.

4.7 Materials and Methods:

Preparation and Biochemical Characterization of *M. thermoacetica*-CdS

M. thermoacetica-CdS was prepared and assayed as previously described with modifications noted below.[91] After full growth, *M. thermoacetica*-CdS was centrifuged under N_2 and resuspended in 20% of the original volume of defined photosynthesis media (DPM) with 0.1 wt.% Cys·HCl and 2.5 atm H_2:CO_2 (80:20) or 25 mM glucose.

At various time points, aliquots of *M. thermoacetica*-CdS were sampled and stored at 4°C under N_2:CO_2 (80:20) until further use.

Benzyl viologen reduction assays were conducted in a modified procedure as previously described.[99] In short, 0.1 mL of *M. thermoacetica*-CdS was added to 5 mL of 50 mM PIPES buffer (pH 7) containing benzyl viologen dichloride with concentrations ranging from 0.5 mM to 8 mM under a 2.5 atm H_2:CO_2 head space in a Hungate tube (Chemglass, Inc.). For varying concentrations of H_2:CO_2, volumes of H_2:CO_2 were syringe injected into an N_2:CO_2 headspace with a fixed concentration of 4 mM benzyl viologen. Kinetics of benzyl viologen reduction were monitored by at 578 nm (Shimadzu UV3101PC UV-Vis-NIR Spectrophotometer with an integrating sphere) for the initial 30 s. Rates were cell normalized by OD_{600} correlated with manual cell counting.

H_2ase activity was calculated assuming pseudo-first order kinetics (constant benzyl viologen or H_2 concentration). The activity is thus defined as mM benzyl viologen formed (mM benzyl viologen)$^{-1}$ (atm H_2)$^{-1}$ s^{-1} cell^{-1}.

For photosynthesis measurements, 1 mL of *M. thermoacetica*-CdS was diluted into 4 mL of DPM with 0.1 wt.% Cys·HCl. The suspension was illuminated by a filtered 75 W Xenon lamp (Newport Corp., AM1.5G, 0.5% sun) with heating and stirring (55 °C, 150 rpm). Liquid sample time points were centrifuged to remove cells and nanoparticles and assayed for by quantitative ^{1}H-NMR.

Transient Absorption Spectroscopy

TAS measurements were acquired with a Helios high temporal resolution transient absorption system with 20 femtosecond resolution and Surface Xplorer software. Samples were held in sealed Starna optical glass 2 mm cells with a ~0.5 optical density. Samples were photoexcited with 350 nm laser pulses with 600 nanojoule power.

Time-Resolved IR Spectroscopy

TRIR spectroscopy was performed with a home-built setup described elsewhere.[114] A 400 nm pump pulse was utilized and the spectral region of 1700-2800 cm^{-1} was probed. The sample was mechanically rastered and circulated in a nitrogen purged and sealed flow cell through 2 IR-transparent windows spaced 30 or 75 µm apart.

_

References

1. Yan, R. *et al.* Nanowire-based single-cell endoscopy. *Nat. Nanotechnol.* **7,** 191–6 (2012).
2. Gómez-Hens, A., Fernández-Romero, J. M. & Aguilar-Caballos, M. P. Nanostructures as analytical tools in bioassays. *Trends Anal. Chem.* **27,** 394–406 (2008).
3. Liu, C. *et al.* Nanowire–Bacteria Hybrids for Unassisted Solar Carbon Dioxide Fixation to Value-Added Chemicals. *Nano Lett.* **15,** 3634–3639 (2015).
4. Hanson, L., Lin, Z. C., Xie, C., Cui, Y. & Cui, B. Characterization of the cell-nanopillar interface by transmission electron microscopy. *Nano Lett.* **12,** 5815–20 (2012).
5. Friedlander, R. S. *et al.* Bacterial flagella explore microscale hummocks and hollows to increase adhesion. *Proc. Natl. Acad. Sci. U. S. A.* **110,** 5624–9 (2013).
6. Wang, H. & Ren, Z. J. A comprehensive review of microbial electrochemical systems as a platform technology. *Biotechnol. Adv.* **31,** 1796–807 (2013).
7. Zhang, T. *et al.* Improved cathode materials for microbial electrosynthesis. *Energy Environ. Sci.* **6,** 217–224 (2013).
8. *Bioelectrochemical Systems: From Extracellular Electron Transfer to Biotechnological Applications*. (IWA Publishing, 2010).
9. Logan, B. E. Exoelectrogenic bacteria that power microbial fuel cells. *Nat. Rev. Microbiol.* **7,** 375–81 (2009).
10. Nevin, K. P., Woodard, T. L., Franks, A. E., Summers, Z. M. & Lovley, D. R. Microbial Electrosynthesis: Feeding Microbes Electricity To Convert Carbon Dioxide and Water to Multicarbon Extracellular Organic Compounds. *MBio* **1,** e00103–10 (2010).
11. Jeong, H. E., Kim, I., Karam, P., Choi, H.-J. & Yang, P. Bacterial Recognition of Silicon Nanowire Arrays. *Nano Lett.* **13,** 2864–2869 (2013).
12. Qi, S., Yi, C., Ji, S., Fong, C.-C. & Yang, M. Cell Adhesion and Spreading Behavior on Verticaly Aligned Silicon Nanowire Arrays. *ACS Appl. Mater. Interfaces* **1,** 30–4 (2009).
13. Epstein, A. K., Hochbaum, A. I., Kim, P. & Aizenberg, J. Control of bacterial biofilm growth on surfaces by nanostructural mechanics and geometry. *Nanotechnology* **22,** 494007 (2011).
14. Männik, J., Driessen, R., Galajda, P., Keymer, J. E. & Dekker, C. Bacterial growth and motility in sub-micron constrictions. *Proc. Natl. Acad. Sci. U. S. A.* **106,** 14861–6 (2009).
15. Anselme, K. *et al.* The interaction of cells and bacteria with surfaces structured at the nanometre scale. *Acta Biomater.* **6,** 3824–46 (2010).
16. Hochbaum, A. I. & Aizenberg, J. Bacteria Pattern Spontaneously on Periodic Nanostructure Arrays. *Nano Lett.* **10,** 3717–21 (2010).
17. van den Burg, B. Extremophiles as a source for novel enzymes. *Curr. Opin. Microbiol.* **6,** 213–218 (2003).
18. Norde, W. *Colloids and Interfaces in Life Sciences and Bionanotechnology*. (CRC Press, Taylor & Francis Group, 2011).
19. Li, B. & Logan, B. E. Bacterial adhesion to glass and metal-oxide surfaces. *Colloids Surfaces B Biointerfaces* **36,** 81–90 (2004).
20. Bayoudh, S., Othmane, A., Mora, L. & Ben Ouada, H. Assessing bacterial adhesion using DLVO and XDLVO theories and the jet impingement technique. *Colloids Surf. B. Biointerfaces* **73,** 1–9 (2009).
21. Rijnaarts, H. H. M., Norde, W., Lyklema, J. & Zehnder, A. J. B. DLVO and steric contributions to bacterial deposition in media of different ionic strengths. *Colloids Surfaces B Biointerfaces* **14,** 179–195 (1999).

22. Eastman, J. in *Colloid Sci. Princ. methods Appl.* (Cosgrove, T.) 36–49 (Blackwell Publishing Ltd, 2005).
23. Elimelech, M. Predicting Collision Efficiencies of Colloidal Particles in Porous Media. *Water Res.* **26,** 1–8 (1992).
24. Ramasamy, R. P., Ren, Z., Mench, M. M. & Regan, J. M. Impact of initial biofilm growth on the anode impedance of microbial fuel cells. *Biotechnol. Bioeng.* **101,** 101–8 (2008).
25. Csonka, L. N. Physiological and Genetic Responses of Bacteria to Osmotic Stress. *Microbiol. Rev.* **53,** 121–47 (1989).
26. Ishii, A., Sato, T., Wachi, M., Nagai, K. & Kato, C. Effects of high hydrostatic pressure on bacterial cytoskeleton FtsZ polymers in vivo and in vitro. *Microbiology* **150,** 1965–72 (2004).
27. Kawarai, T. *et al.* Biofilm formation by *Escherichia coli* in hypertonic sucrose media. *J. Biosci. Bioeng.* **107,** 630–5 (2009).
28. Meury, J. Glycine betaine reverses the effects of osmotic stress on DNA replication and cellular division in Escherichia coli. *Arch. Microbiol.* **149,** 232–239 (1988).
29. Stephens, M. A. Use of the Kolmogorov-Smirnov, Cramer-Von Mises and Related Statistics Without Extensive Tables. *J. R. Stat. Soc. Ser. B* **32,** 115–122 (1970).
30. Poortinga, A. T., Bos, R. & Busscher, H. J. Reversibility of Bacterial Adhesion at an Electrode Surface. *Langmuir* **17,** 2851–2856 (2001).
31. Walker, S. L., Hill, J. E. & Redman, J. A. Influence of Growth Phase on Adhesion Kinetics of *Escherichia coli* D21g. *Appl. Environ. Microbiol.* **71,** 3093–3099 (2005).
32. Bray, D. F., Bagu, J. & Koegler, P. Comparison of Hexamethyldisilazane (HMDS), and Peldri II, and Critical-Point Drying Methods for Scanning Electron Microscopy of Biological Specimens. *Microsc. Res. Tech.* **26,** 489–95 (1993).
33. Larkum, A. W. D. Limitations and prospects of natural photosynthesis for bioenergy production. *Curr. Opin. Biotechnol.* **21,** 271–276 (2010).
34. Gust, D., Moore, T. A. & Moore, A. L. Solar Fuels via Artificial Photosynthesis. *Acc. Chem. Res.* **42,** 1890–1898 (2009).
35. Blankenship, R. E. *et al.* Comparing Photosynthetic and Photovoltaic Efficiencies and Recognizing the Potential for Improvement. *Science (80-.).* **332,** 805–809 (2011).
36. Meyer, T. J. Chemical Approaches to Artificial Photosynthesis. *Acc. Chem. Res.* **22,** 163–170 (1989).
37. Appel, A. M. *et al.* Frontiers, Opportunities, and Challenges in Biochemical and Chemical Catalysis of CO_2 Fixation. *Chem. Rev.* **113,** 6621–6658 (2013).
38. Hawkins, A. S., McTernan, P. M., Lian, H., Kelly, R. M. & Adams, M. W. W. Biological conversion of carbon dioxide and hydrogen into liquid fuels and industrial chemicals. *Curr. Opin. Biotechnol.* **24,** 376–84 (2013).
39. Brown, K. A., Wilker, M. B., Boehm, M., Dukovic, G. & King, P. W. Characterization of Photochemical Processes for H2 Production by CdS Nanorod-[FeFe] Hydrogenase Complexes. *J. Am. Chem. Soc.* **134,** 5627–5636 (2012).
40. Giraldo, J. P. *et al.* Plant nanobionics approach to augment photosynthesis and biochemical sensing. *Nat. Mater.* **13,** 400–408 (2014).
41. Torella, J. P. *et al.* Efficient solar-to-fuels production from a hybrid microbial–water-splitting catalyst system. *Proc. Natl. Acad. Sci.* **112,** 2337–2342 (2015).
42. Lapinsonnière, L., Picot, M. & Barrière, F. Enzymatic versus Microbial Bio-Catalyzed Electrodes in Bio-Electrochemical Systems. *ChemSusChem* **5,** 995–1005 (2012).

43. Nevin, K. P. *et al.* Electrosynthesis of Organic Compounds from Carbon Dioxide Is Catalyzed by a Diversity of Acetogenic Microorganisms. *Appl. Environ. Microbiol.* **77,** 2882–2886 (2011).
44. King, P. W. Designing interfaces of hydrogenase-nanomaterial hybrids for efficient solar conversion. *Biochim. Biophys. Acta* **1827,** 949–957 (2013).
45. Crookes-Goodson, W. J., Slocik, J. M. & Naik, R. R. Bio-directed synthesis and assembly of nanomaterials. *Chem. Soc. Rev.* **37,** 2403–2412 (2008).
46. Ducat, D. C. & Silver, P. A. Improving carbon fixation pathways. *Curr. Opin. Chem. Biol.* **16,** 337–44 (2012).
47. Gronenberg, L. S., Marcheschi, R. J. & Liao, J. C. Next generation biofuel engineering in prokaryotes. *Curr. Opin. Chem. Biol.* **17,** 462–471 (2013).
48. Fast, A. G. & Papoutsakis, E. T. Stoichiometric and energetic analyses of non-photosynthetic CO_2-fixation pathways to support synthetic biology strategies for production of fuels and chemicals. *Curr. Opin. Chem. Eng.* **1,** 380–395 (2012).
49. Van Eerten-Jansen, M. C. A. A. *et al.* Bioelectrochemical Production of Caproate and Caprylate from Acetate by Mixed Cultures. *ACS Sustain. Chem. Eng.* **1,** 513–518 (2013).
50. Sakimoto, K. K., Liu, C., Lim, J. & Yang, P. Salt-Induced Self-Assembly of Bacteria on Nanowire Arrays. *Nano Lett.* **14,** 5471–5476 (2014).
51. Vogel, R., Hoyer, P. . & Weller, H. Quantum-sized PbS, CdS, Ag_2S, Sb_2S_3, and Bi_2S_3 Particles as Sensitizers for Various Nanoporous Wide-Bandgap Semiconductors. *J. Phys. Chem.* **98,** 3183–3188 (1994).
52. Drake, H. L. & Daniel, S. L. Physiology of the thermophilic acetogen *Moorella thermoacetica*. *Res. Microbiol.* **155,** 869–883 (2004).
53. Cunningham, D. P. & Lundie, L. L. Precipitation of cadmium by *Clostridium thermoaceticum*. *Appl. Environ. Microbiol.* **59,** 7–14 (1993).
54. Holmes, J. D. *et al.* Bacterial Photoprotection Through Extracellular Cadmium Sulfide Crystallites. *Photochem. Photobiol.* **62,** 1022–1026 (1995).
55. Daniel, S. L., Hsu, T., Dean, S. I., Drake, H. L. & Ljungdahl, L. Characterization of the H_2- and CO-dependent Chemolithotrophic Potentials of the Acetogens *Clostridium thermoaceticum* and *Acetogenium kivui*. *J. Bacteriol.* **172,** 4464–4471 (1990).
56. Dumas, E. *et al.* Interfacial Charge Transfer between CdTe Quantum Dots and Gram Negative Vs Gram Positive Bacteria. *Environ. Sci. Technol.* **44,** 1464–1470 (2010).
57. Liu, B., Zhao, X., Terashima, C., Fujishima, A. & Nakata, K. Thermodynamic and kinetic analysis of heterogeneous photocatalysis for semiconductor systems. *Phys. Chem. Chem. Phys* **16,** 8751–8760 (2014).
58. Schuchmann, K. & Müller, V. Autotrophy at the thermodynamic limit of life: a model for energy conservation in acetogenic bacteria. *Nat. Rev. Microbiol.* **12,** 809–821 (2014).
59. Hankamer, B. *et al.* Photosynthetic biomass and H_2 production by green algae: From bioengineering to bioreactor scale-up. *Physiol. Plant.* **131,** 10–21 (2007).
60. Cha, H. G. & Choi, K.-S. Combined biomass valorization and hydrogen production in a photoelectrochemical cell. *Nat. Chem.* **7,** 328–333 (2015).
61. Logan, B. E. & Rabaey, K. Conversion of Wastes into Bioelectricity and Chemicals by using Microbial Electrochemical Technologies. *Science (80-.).* **337,** 686–690 (2012).
62. Kita, A. *et al.* Development of genetic transformation and heterologous expression system in carboxydotrophic thermophilic acetogen *Moorella thermoacetica*. *J. Biosci. Bioeng.* **115,** 347–352 (2013).

63. Jensen, H. M. *et al.* Engineering of a synthetic electron conduit in living cells. *Proc. Natl. Acad. Sci. U. S. A.* **107,** 19213–19218 (2010).
64. Wang, C. L., Lum, A. M., Ozuna, S. C., Clark, D. S. & Keasling, J. D. Aerobic sulfide production and cadmium precipitation by *Escherichia coli* expressing the Treponema denticola cysteine desulfhydrase gene. *Appl. Microbiol. Biotechnol.* **56,** 425–430 (2001).
65. Rosenbaum, M., Aulenta, F., Villano, M. & Angenent, L. T. Cathodes as electron donors for microbial metabolism: Which extracellular electron transfer mechanisms are involved? *Bioresour. Technol.* **102,** 324–33 (2011).
66. Deutzmann, J. S., Sahin, M. & Spormann, A. M. Extracellular Enzymes Facilitate Electron Uptake in Biocorrosion and Bioelectrosynthesis. *MBio* **6,** 1–8 (2015).
67. Kim, D., Sakimoto, K. K., Hong, D. & Yang, P. Artificial Photosynthesis for Sustainable Fuel and Chemical Production. *Angew. Chemie Int. Ed.* **54,** 3259–3266 (2015).
68. Osterloh, F. E. Inorganic nanostructures for photoelectrochemical and photocatalytic water splitting. *Chem. Soc. Rev.* **42,** 2294–320 (2013).
69. Kumar, B. *et al.* Photochemical and photoelectrochemical reduction of CO_2. *Annu. Rev. Phys. Chem.* **63,** 541–69 (2012).
70. Magnuson, A. *et al.* Biomimetic and Microbial Approaches to Solar Fuel Generation. *Acc. Chem. Res.* **42,** 1899–1909 (2009).
71. Nichols, E. M. *et al.* Hybrid bioinorganic approach to solar-to-chemical conversion. *Proc. Natl. Acad. Sci.* **112,** 11461–11466 (2015).
72. Wang, W., Chen, J., Li, C. & Tian, W. Achieving solar overall water splitting with hybrid photosystems of photosystem II and artificial photocatalysts. *Nat Commun* **5,** 4647 (2014).
73. Sakimoto, K. K., Wong, A. B. & Yang, P. Self-photosensitization of nonphotosynthetic bacteria for solar-to-chemical production supporting information. *Science (80-.).* **351,** 1–17 (2016).
74. Meissner, D. & Memming, R. Photoelectrochemistry of cadmium sulfide. 1. Reanalysis of photocorrosion and flat-band potential. *J. Phys.* … 3476–3483 (1988). at <http://pubs.acs.org/doi/pdf/10.1021/j100323a032>
75. Kudo, A. & Miseki, Y. Heterogeneous photocatalyst materials for water splitting. *Chem. Soc. Rev.* **38,** 253–78 (2009).
76. Chen, X. & Mao, S. S. Titanium dioxide nanomaterials: Synthesis, properties, modifications and applications. *Chem. Rev.* **107,** 2891–2959 (2007).
77. Resasco, J. *et al.* TiO_2/$BiVO_4$ Nanowire Heterostructure Photoanodes Based on Type II Band Alignment. *ACS Cent. Sci.* acscentsci.5b00402 (2016). doi:10.1021/acscentsci.5b00402
78. Liu, C., Tang, J., Chen, H. M., Liu, B. & Yang, P. A fully integrated nanosystem of semiconductor nanowires for direct solar water splitting. *Nano Lett.* **13,** 2989–92 (2013).
79. Paulsen, C. E. & Carroll, K. S. Cysteine-mediated redox signaling: Chemistry, biology, and tools for discovery. *Chem. Rev.* **113,** 4633–4679 (2013).
80. Nosaka, A. Y., Tanaka, G. & Nosaka, Y. The Behaviors of Glutathione and Related Amino Acids in the TiO_2 Photocatalytic System. *J. Phys. Chem. B* **116,** 11098–11102 (2012).
81. Machado, A. E. H. *et al.* Characterization and Evaluation of the Efficiency of TiO_2 /Zinc Phthalocyanine Nanocomposites as Photocatalysts for Wastewater Treatment Using Solar Irradiation. *Int. J. Photoenergy* **2008,** (2008).
82. Zagal, J. H. & Herrera, P. Electrochemistry of cysteine and cystine on metal-

phthalocyanines adsorbed on a graphite electrode. *Electrochim. Acta* **30,** 449–454 (1985).
83. Ghani, F., Kristen, J. & Riegler, H. Solubility Properties of Unsubstituted Metal Phthalocyanines in Different Types of Solvents. *J. Chem. Eng. Data* **57,** 439–449 (2012).
84. Giribabu, L. *et al.* Unsymmetrical alkoxy zinc phthalocyanine for sensitization of nanocrystalline TiO_2 films. *Sol. Energy Mater. Sol. Cells* **91,** 1611–1617 (2007).
85. Liao, M. S. & Scheiner, S. Electronic structure and bonding in metal phthalocyanines, metal=Fe, Co, Ni, Cu, Zn, Mg. *J. Chem. Phys.* **114,** 9780–9791 (2001).
86. Ireland JC, Klostermann P, Rice EW, C. R. Inactivation of Escherichia coli by titanium dioxide photocatalytic oxidation. *Appl. Environ. Microbiol.* **59,** 1668–1670 (1993).
87. Karnholz, A., Küsel, K., Gößner, A., Drake, H. L. & Schramm, A. Tolerance and Metabolic Response of Acetogenic Bacteria toward Oxygen Tolerance and Metabolic Response of Acetogenic Bacteria toward Oxygen. *Appl. Environ. Microbiol.* **68,** 1005 (2002).
88. Giddings, C. G. S., Nevin, K. P., Woodward, T., Lovley, D. R. & Butler, C. S. Simplifying microbial electrosynthesis reactor design. *Front. Microbiol.* **6,** 1–6 (2015).
89. Ort, D. R. *et al.* Redesigning photosynthesis to sustainably meet global food and bioenergy demand. *Proc. Natl. Acad. Sci.* **112,** 8529–8536 (2015).
90. Faunce, T. A. *et al.* Energy and environment policy case for a global project on artificial photosynthesis. *Energy Environ. Sci.* **6,** 695–698 (2013).
91. Sakimoto, K. K., Wong, A. B. & Yang, P. Self-photosensitization of nonphotosynthetic bacteria for solar-to-chemical production. *Science (80-.).* **351,** 74–77 (2016).
92. Kuzume, A. *et al.* An in situ surface electrochemistry approach towards whole-cell studies: the structure and reactivity of a *Geobacter sulfurreducens* submonolayer on electrified metal/electrolyte interfaces. *Phys. Chem. Chem. Phys.* **16,** 22229–36 (2014).
93. Kracke, F., Vassilev, I. & Krömer, J. O. Microbial electron transport and energy conservation - The foundation for optimizing bioelectrochemical systems. *Front. Microbiol.* **6,** 1–18 (2015).
94. Das, A. & Ljungdahl, L. in *Biochem. Physiol. Anaerob. Bact.* 191–204 (2003). doi:10.1007/0-387-22731-8_14
95. Pierce, E. *et al.* The complete genome sequence of *Moorella thermoacetica* (f. *Clostridium thermoaceticum*). *Environ. Microbiol.* **10,** 2550–73 (2008).
96. Greene, B. L., Joseph, C. A., Maroney, M. J. & Dyer, R. B. Direct Evidence of Active-Site Reduction and Photodriven Catalysis in Sensitized Hydrogenase Assemblies. *J. Am. Chem. Soc.* **134,** 11108–11111 (2012).
97. Utterback, J. K. *et al.* Competition between electron transfer, trapping, and recombination in CdS nanorod–hydrogenase complexes. *Phys. Chem. Chem. Phys.* **17,** 5538–5542 (2015).
98. Wilker, M. B. *et al.* Electron Transfer Kinetics in CdS Nanorod-[FeFe]-Hydrogenase Complexes and Implications for Photochemical H_2 Generation. *J. Am. Chem. Soc.* **136,** 4316–24 (2014).
99. Drake, H. L. Demonstration of Hydrogenase in Extracts of the Homoacetate-Fermenting Bacterium *Clostridium thermoaceticum*. *J. Bacteriol.* **150,** 702–709 (1982).
100. Brown, K. a, Dayal, S., Ai, X., Rumbles, G. & King, P. W. Controlled Assembly of Hydrogenase-CdTe Nanocrystal Hybrids for Solar Hydrogen Production. *J. Am. Chem. Soc.* **132,** 9672–80 (2010).
101. Tseng, H. W., Wilker, M. B., Damrauer, N. H. & Dukovic, G. Charge Transfer Dynamics between Photoexcited CdS Nanorods and Mononuclear Ru Water-Oxidation Catalysts. *J.*

Am. Chem. Soc. **135,** 3383–3386 (2013).
102. Nosaka, Y., Miyama, H., Terauchi, M. & Kobayashi, T. Photoinduced Electron Transfer from Colloidal Cadmium Sulfide to Methylviologen: A Picosecond Transient Absorption Study. *J Phys Chem* **255,** 6521–6522 (1988).
103. Ben-Shahar, Y. *et al.* Optimal metal domain size for photocatalysis with hybrid semiconductor-metal nanorods. *Nat. Commun.* **7,** 10413 (2016).
104. Kambhampati, P. Unraveling the Ttructure and Dynamics of Excitons in Semiconductor Quantum Dots. *Acc. Chem. Res.* **44,** 1–13 (2011).
105. Gray, H. B. & Winkler, J. R. Electron Transfer in Proteins. *Annu. Rev. Biochem.* **65,** 537–561 (1996).
106. Gray, H. B. & Winkler, J. R. Long-range electron transfer. *Proc. Natl. Acad. Sci. U. S. A.* **102,** 3534–9 (2005).
107. Morra, S. *et al.* Direct electrochemistry of an [FeFe]-hydrogenase on a TiO_2 electrode. *Chem. Commun. (Camb).* **47,** 10566–8 (2011).
108. Flanagan, L. A. & Parkin, A. Electrochemical insights into the mechanism of NiFe membrane-bound hydrogenases. *Biochem. Soc. Trans.* **44,** 315–328 (2016).
109. De Lacey, A. L., Fernández, V. M., Rousset, M. & Cammack, R. Activation and Inactivation of Hydrogenase Function and the Catalytic Cycle: Spectroelectrochemical Studies. *Chem. Rev.* **107,** 4304–4330 (2007).
110. Kong, J. & Yu, S. Fourier Transform Infrared Spectroscopic Analysis of Protein Secondary Structures. *Acta Biochim. Biophys. Sin. (Shanghai).* **39,** 549–559 (2007).
111. Venyaminov, S. Y. & Kalnin, N. N. Quantitative IR Spectrophometry of Peptide Compounds in Water (H_2O) Solutions. I Spectral Parameters of Amino Acid Residue Absorption Bands. *Biopolymers* **30,** 1243–1257 (1990).
112. Pandelia, M. E., Ogata, H., Currell, L. J., Flores, M. & Lubitz, W. Probing intermediates in the activation cycle of [NiFe] hydrogenase by infrared spectroscopy: The Ni-SIr state and its light sensitivity. *J. Biol. Inorg. Chem.* **14,** 1227–1241 (2009).
113. Pierik, A. J., Roseboom, W., Happe, R. P., Bagley, K. A. & Albracht, S. P. J. Carbon Monoxide and Cyanide as Intrinsic Ligands to Iron in the Active Site of [NiFe]-Hydrogenases. *J. Biol. Chem.* **274,** 3331–3337 (1999).
114. Nguyen, S. C. *et al.* Chemistry of the Triplet 14-Electron Complex $Fe(CO)_3$ in Solution Studied by Ultrafast Time-Resolved IR Spectroscopy. *Organometallics* **31,** 3980–3984 (2012).